*DISTRIBUTION STATEMENT A. Approved for public release; distribution is unlimited.*

# FINAL REPORT

# Analysis of Spatiotemporal Clutter Statistics and Support for the Five Octave Research Array

Chad M. Smith
The Pennsylvania State University
Applied Research Laboratory
P.O. Box 30
State College, PA 16804-0030
phone: (814) 863-4159 fax: (814) 865-8069 email: cms561@arl.psu.edu

Award Number: N00014-16-1-2561
Period of Performance: June 1st, 2016 to November 30th, 2021

## SUMMARY

The following represents the final project report for ONR Code 322-OA. This report outlines chief goals and accomplishments carried out during this project. Publications (3), a report for the major experimental endeavor (SCEX17), and documentation for the final acceptance of the new ONR-OA towed line array are attached.

## PRIMARY GOALS AND ACHIEVEMENTS

- Significant advances were made in characterizing and understanding spatial coherence statistics for active littoral sonar during the reporting period. Several statistics related to spatial reverberation coherence were developed for steered line array systems, and physical-statistical analytic and computational models were developed. These models were used to quantitatively assess whether spatial coherence statistics can provide useful information about the azimuthal distribution of scattering within broad, low-resolution sonar beams for certain types of clutter. It was found they can provide complementary information to more commonly used active sonar statistics (e.g., signal envelope or intensity) from the standpoint of environmental assessment, clutter characterization, and statistical processing. In particular, they may provide a valuable method of separating compact (small compared with beamwidth) and non-compact (large compared with beamwidth) clutter. The TREX13 FORA dataset was the primary dataset used in this work. This work is summarized in publication/attachment 1 (abstract only due to file size).

- Data collection and analysis using the FORA and additional acoustic acquisition systems during the SCEX17 New England mud patch experiment. This data collection provided a wealth of data for analysis in the interest of geoacoustic inversion, scattering, and reverberation from muddy seabeds. One of the most significant findings during this work was the existence of an angle of intromission in single-bounce acoustic returns from the seabed. This is direct evidence of the muddy properties of the seabed within the experimental region. This work was in conjunction with

# REPORT DOCUMENTATION PAGE

*Form Approved*
**OMB No. 0704-0188**



**1. REPORT DATE** *(DD-MM-YYYY)*

**2. REPORT TYPE**
Final

**3. DATES COVERED** *(From - To)*
June 01, 2016 - November 30, 2021

**4. TITLE AND SUBTITLE**
Analysis of Spatiotemporal Clutter Statistics and Support for the Five Octave Research Array

**5a. CONTRACT NUMBER**

**5b. GRANT NUMBER**
N00014-16-1-2561

**5c. PROGRAM ELEMENT NUMBER**

**6. AUTHOR(S)**
Chad Smith

**5d. PROJECT NUMBER**

**5e. TASK NUMBER**

**5f. WORK UNIT NUMBER**

**7. PERFORMING ORGANIZATION NAME(S) AND ADDRESS(ES)**
The Pennsylvania State University Applied Research Labotatory
Office of Sponsored Programs
110 Technology Center Building
University Park, PA 16802-7000

**8. PERFORMING ORGANIZATION REPORT NUMBER**

**9. SPONSORING/MONITORING AGENCY NAME(S) AND ADDRESS(ES)**
Office of Naval Research
875 North Randolph Street
Arlington, VA 22203-1995

**10. SPONSOR/MONITOR'S ACRONYM(S)**
ONR

**11. SPONSORING/MONITORING AGENCY REPORT NUMBER**

**12. DISTRIBUTION AVAILABILITY STATEMENT**
Approved for Public Release; distibution is Unlimited.

**13. SUPPLEMENTARY NOTES**

**14. ABSTRACT**
Chief goals and accomplishments of this project are summarized in the attached final report. Publications (3), a report for the major experimental endeavor (the seabed characterization experiment of 2017, deemed SCEX17), and documentation for the final acceptance of the new Ocean Acoustics towed line array are also attached with the report. Significant scientific work included advancements in characterizing and modeling spatial coherence statistics for active littoral sonar reverberation, and an SCEX17 geoacoustic inversion analysis finding significant evidence of a low sound speed seabed within the SCEX17 experimental region. During the SCEX17 experiment, PSU-ARL collected close to a terabyte of acoustic data, primarily in the interest of geoacoutics inversion and seabed scattering research. Finally, a significant amount of effort went towards a trade study of the best way to move forward with the aging FORA array, and management of design and development of a FORA replacement ONR-OA towed line array acquisition system.

**15. SUBJECT TERMS**

| **16. SECURITY CLASSIFICATION OF:** | | | **17. LIMITATION OF ABSTRACT** | **18. NUMBER OF PAGES** | **19a. NAME OF RESPONSIBLE PERSON** |
|---|---|---|---|---|---|
| **a. REPORT** | **b. ABSTRACT** | **c. THIS PAGE** | SAR | | Chad Smith |
| U | U | U | | | **19b. TELEPONE NUMBER (*Include area code*)** 814-863-4159 |

the work of Charles Holland (now at Portland State University). Connected with preparations for this work, was final analysis and reporting on single bounce geoacoustic inversion measurements taken during the TREX13 experiment. Findings and experimental work are summarized in attachments, 2, 3, and 4.

- PSU-ARL conducted a trade study concerning the most cost effective and scientifically advantageous way forward to maintain ONR-OA's experimental towed array capabilities in light of the aging FORA. The best route forward was determined to be development of a new research array, but reusing several high cost components of the FORA system. Quotes were obtained from several sources and it was found the engineering group at the Centre for Maritime Research and Experimentation (CMRE) was by far the most cost efficient and flexible in array design options. PSU submitted a DURIP to ONR-OA that was funded in 2019 to acquire this FORA replacement acquisition system.

- The management of array design and development of the new ONR towed array system also fell under this project. The new array is a large diameter design that incorporates much of the geometry and the non-summed hydrophone design of the FORA. It was developed with a modular design and significant headspace in data throughput, so additional apertures could be added in future work if scientific need and funding warrant. The new array passed factory acceptance testing and was delivered to ARL-PSU in late 2021. It will replace the highly accomplished but poorly aging FORA array, which had become unreliable and costly to maintain. This research acquisition system is expected to provide significant advancements to PSU-ARL and ONR-OA's experimental capabilities. Array design specifications are discussed later in this report, and final acceptance documentation is provided in attachment 5.

- This work also covered design and planning of a FORA replacement engineering trial. Unfortunately, DURIP funds were not able to cover the costs of wet testing the new array— only laboratory verification and acceptance testing. PSU-ARL developed a test plan for an engineering trial of the new towed array system. This plan was provided to the array development group (CMRE's engineering group) for comment and revision. This trial could take place as a standalone engineering trial or in conjunction with a science trial. The engineering trial requirements are outlined in the last section of this report.

## RELATED PUBLICATIONS


1) Smith, C. M. (2021). *Modeling and analysis of transverse horizontal spatial coherence statistics for reverberation-limited active littoral sonar* [Doctoral dissertation, The Pennsylvania State University, State College, PA, USA]. (Only the abstract is attached due to file size, but full the file is at https://etda.libraries.psu.edu/files/final_submissions/23803.)

2) Holland, C. W., Smith, C. M., Lowe, Z., and Dorminy, J. (2021). Seabed observations at the New England Mud Patch: Reflection and scattering measurements and direct geoacoustic information. *IEEE Journal of Oceanic Engineering*. (Attachment 2.)

3) Holland, C. W., Pinson, S., Smith, C. M., Hines, P. C., Olson, D. R., Dosso, S. E., & Dettmer, J. (2017). Seabed structure inferences from TREX13 reflection measurements. *IEEE Journal of Oceanic Engineering*, 42(2), 268-288. (Attachment 3.)

## RESULTS

### Modeling and Analysis of Spatial Coherence-based Clutter Statistics

Significant advances were made in characterizing and understanding spatial coherence statistics for active sonar during the reporting period. Several statistics related to spatial reverberation coherence were developed for steered line array systems, and physical-statistical analytic models were developed for diffuse reverberation. A computational reverberation model capable of estimating complex scenarios within the long-range littoral environment was also developed. These models were used to quantitatively assess information about the azimuthal distribution of scattering within broad, low-resolution sonar beams for certain types of clutter. Clutter types included water-column biologics as well as stationary bottom clutter, each of which can cause false alarms and/or obscure targets for sonar systems. However, published work thus far has focused primarily on stationary clutter types. It was found that these statistics may provide complementary information to more commonly used active sonar statistics (e.g., signal envelope, intensity) from the standpoint of environmental assessment, clutter characterization, and statistical processing. In particular, these statistics may provide a valuable method of separating compact (small compared with beamwidth) and non-compact (large compared with beamwidth) clutter. Much of this work is summarized in the attached dissertation [1] and will be further reported in journal articles currently in draft. The remaining portion of this section will summarize results found in this study.

Active sonar systems operating in the littoral environment are often reverberation-limited. This self-noise reduces the effective signal-to-noise ratio (SNR) of the sonar system. False detections, often termed clutter, are caused when the sonar processing system mistakes signals from the environment or of anthropogenic origin for targets of interest. Clutter is found is all environments, but shallow water littoral regions can be especially challenging due to the shallow water waveguide and a large number of complex variables including bathometric and geoacoustic irregularities. Analysis during this reporting period focused development and analysis of statistics related to the transverse horizontal spatial coherence (THSC) of a directional active sonar platform within a reverberation-limited littoral environment. Primary goals were to: 1) theoretically characterize and experimentally verify physical-statistical models of THSC statistics for diffuse reverberation scenarios, 2) develop computational tools to assess the influence of complex littoral features on these statistics, and, 3) empirically assess whether there is interpretable information in these statistics pertaining to the azimuthal distribution of scattering within low-resolution sonar beams that is complementary to more common sonar statistics (e.g., signal envelope [SE], and intensity). This research may lead to novel methods for environmental assessment and clutter characterization by incorporating information about the azimuthal spatial distribution of littoral reverberation without the need of a highly focused beampattern or steering of the beam across the region of interest (beam steering can be used in this processing, but is not a requirement of coherence statistic calculation).

The THSC is dependent upon the spatial distribution of scattering relative to the beampattern width. As a simple example, when a receiver array is steered directly toward a group of random scatterers that cover the entire sonar cell, a narrow THSC is expected *regardless of signal level*. However, a much more broad THSC would be expected if the sonar was moved far enough from this same group of random scatterers so they only populate half the azimuthal width of the sonar beam— even if the signal level of the latter case is much less. This work developed and characterized two THSC statistics, and carried out an empirical investigation of their utility in separating large-scale from small-scale (compared to beampattern size) scattering events for a moored horizontal towed array (TREX13). This sonar system was a pseudo-monostatic, broadband (900 Hz bandwidth), mid-frequency (3150 Hz center frequency), active sonar platform. Each spatial coherence statistic used provides a level of control over sampling uncertainty through temporal averaging, allowing investigation of the impact of differing environmental and platform conditions such as irregular bathymetry and beampattern parameters. For reference, a comparative statistic based on SE was also developed with similar temporal averaging length and noise normalization power. This statistic takes the form of a common energy detector (ED), and allows a more direct comparison (equal time gating windows, averaging length, and noise normalization power) with spatial coherence statistics while remaining related to SE and intensity. The van Cittert-Zernike theorem and sampling theory were used to derive analytic physical-statistical models of the expected correlation function, and probability distributions of each statistic under an assumption of diffuse reverberation. A coherent, ray-based computational reverberation model was also developed to simulate more realistic littoral examples and compare general trends with experimental data. Experimental data from a moored source-receiver geometry was analyzed to ensure minimal pulse-to-pulse dynamics, allowing analysis of the influence of stationary bathymetric and anthropogenic clutter types over many pulses. Statistical analysis showed empirically that THSC statistics can be used in a complementary fashion with more common signal statistics for discerning scattering events that are significantly smaller or larger in azimuthal extent than the sonar beam.

*Statistics of Interest*

Two spatial coherence statistics were developed and used as the basis of this work. A split-beam correlation coefficient (SBCC) statistic was chosen due to its relative simplicity in processing and connection with prior work. This statistic is simply the SBCC estimated at a single displacement distance between two steered array subapertures and can be used with relatively simple sonar platforms; the simplest requiring only two spatially separated directional sonar transducers. The second coherence statistic, deemed split-beam correlation length (SBCL), was added to this work to incorporate more of the information that is available in systems that have many receiver elements and provide a more physical connection with the breadth of the spatial coherence function. Figure 1 displays how these two statistics are related to the THSC function calculated along that array. A third statistic based on the temporal moment of signal envelope (SE) is also developed for comparison with spatial coherence statistics. This statistic takes the form of a simple energy detector with similar normalization power to coherence statistics.

*Physical-statistical Model*

Physical statistical models were developed based on an assumption of an incoherent backscattered acoustic field caused by littoral multipath, the van Cittert–Zernike theorem, and sonar system parameters. Assuming the transmitter is omnidirectional in the horizontal direction and the receiver elements are completely omnidirectional, the expected THSC function is equal the apodization function used in beamforming [1,3,4]. For the common Hann (cosine-squared) apodization this results in a THSC function equal to Eq. 1 [1],

$$\rho(\Delta x_0) = \frac{1}{3}\left(1 - \frac{\Delta x_0}{L_0}\right)\left(2 + \cos\left(2\pi\frac{\Delta x_0}{L_0}\right)\right) + \frac{1}{2\pi}\sin\left(2\pi\frac{\Delta x_0}{L_0}\right) \qquad \text{Eq. 1}$$

where, $\rho$, is the correlation coefficient, $L_0$, is the length of the array subapertures used, and, $\Delta x_0$, is the displacement distance between the two subaperture in the direction of the full array aperture. Statistical sampling uncertainty can then be used as a baseline uncertainty for the SBCC when the assumption of incoherence applies adequately. This sampling uncertainty can then be transformed to SBCL uncertainty using standard statistical transformation methods. This development and models are discussed more thoroughly in Chap. 2 of [1].

Figure 2 displays a comparison of the analytic statistical models developed in this work to data from a highly reverberant, benign littoral region. Polar plots (a) through (c) display color plots of the each statistic of interest in dB re E[$\eta_i$], where E[$\eta_i$] is the expected value of the statistic ($x_{SBCC} = 1/e$, $x_{SBCC} = 0.96$ m, and $x_{ED} = 1$ Pa$^2$). This scaling is an attempt at an "apple-to-apples" comparison of each statistic. Plot (d) displays a statistical comparison of the analytic models developed in this work. Blue histograms represents data from the shaded region in polar plots (a) through (c); the left being PDFs while the right are the associated CDFs. The upper PDF/CDF pair is the SBCC statistic with a hypergeometric based uncertainty model shown in red, and a Gaussian approximation to the hypergeometric model in black. The center PDF/CDF pair is SBCL with transformed-Gaussian based uncertainty in black. The lower PDF/CDF pair is ED with ideal $\chi_{2n_i}$ uncertainty shown in red. Note for an acoustical benign region/return, the models fit quite well. It was found that the model developed in this work provide a useful baseline for statistical analysis of spatial coherence metrics. Deviation from these models represent a more complex region that may constitute a region with significant clutter.

*Statistical Analysis of Compact vs. Non-compact Clutter*

A statistical analysis of compact vs. non-compact clutter was carried out in efforts to determine if spatial coherence statistics can be used to help discriminate between clutter events that are caused by scattering regions much smaller than sonar beamwidth (compact) and those that are much larger than the width of the beam (non-compact). This was done by comparing exceedances of the developed spatial coherence and ED statistics for known compact (a shipwreck) and non-compact (the shoreline termination) scattering events. Processing parameters including averaging length and normalization power were kept equal for ED and spatial coherence statistic processing, as was the data-derived 1% threshold of exceedance. It was found that while the ED statistic often had exceedances for both compact and non-compact clutter events, the spatial coherence statistics often did not have exceedances for non-compact events.

Figure 3 provides an example of the geospatially registered exceedances used to compare the different statistics. There were 84 geospatially registered (acceptable) sonar returns analyzed in this work. The three test statistics are shown using a 1% threshold estimated from data (roughly displaying the spatial location of the highest 1% of each statistic). ED is shown using cyan circles, SBCL with green triangles, and SBCC using red x's. The lower portion of plot shows chronological order of pulses. "S" and "B" annotations are the wreck of the USS Strength and a sunken bridge span, respectively, each discussed by Lee et al. [5]. Very often, all three statistics had exceedances for compact scattering events such as the shipwreck or bridge span. However, for non-compact events such as the shoreline closest to the array (very wide compared to the beam at the range), coherence statistics often did *not* have an exceedance. These results are summarized in Figs. 4 and 5.

Figure 4 displays an exceedance analysis of the shipwreck of the USS Strength. Plot (a) shows exceedances for each statistic geospatially registered for all 84 pulses (for a small 150 m circle masked around the shipwreck), while plot (b) provides a summary exceedance bar chart with 95% confidence interval (CI). Two composite statistics represent the sum of the number of times both ED and SBCC or SBCL have an exceedance at the same location. Composite statistics of similar number (within the 95% CI denoted by the blue and yellow bars) to ED imply the ED and THSC statistics are essentially dependent for compact scattering events. This suggests the object is relatively compact compared to the sonar beam. Figure 5 then shows a shallow-water exceedance analysis (depths < 7 m) similar in format to Fig. 4. This analysis looks at geospatially-registered return only from regions < 7 m depth to capture the full shoreline return. This allow a comparison of the statistics within a region where known non-compact returns are located. In particular, the bright return from the shoreline termination. Note the composite statistic sums are significantly less than the ED, implying ED and THSC statistics are reasonably independent of one another. The red dashed circle shows known compact scattering events that may have affected this assessment and caused higher composite statistic sums.

*This statistical comparison of compact and non-compact returns shows that spatial coherence statistics and more commonly used statistics (those directly related to the acoustic intensity) are highly dependent upon one another for compact clutter events (those small compared to a sonar beamwidth). However, they are much less so for non-compact clutter events (those large compared to a sonar beamwidth). This has implications in aiding in clutter type discretion and clutter mitigation. Additionally, this opens the possibility of estimating the physical size of the scattering region for physical assessment of environmental clutter.*

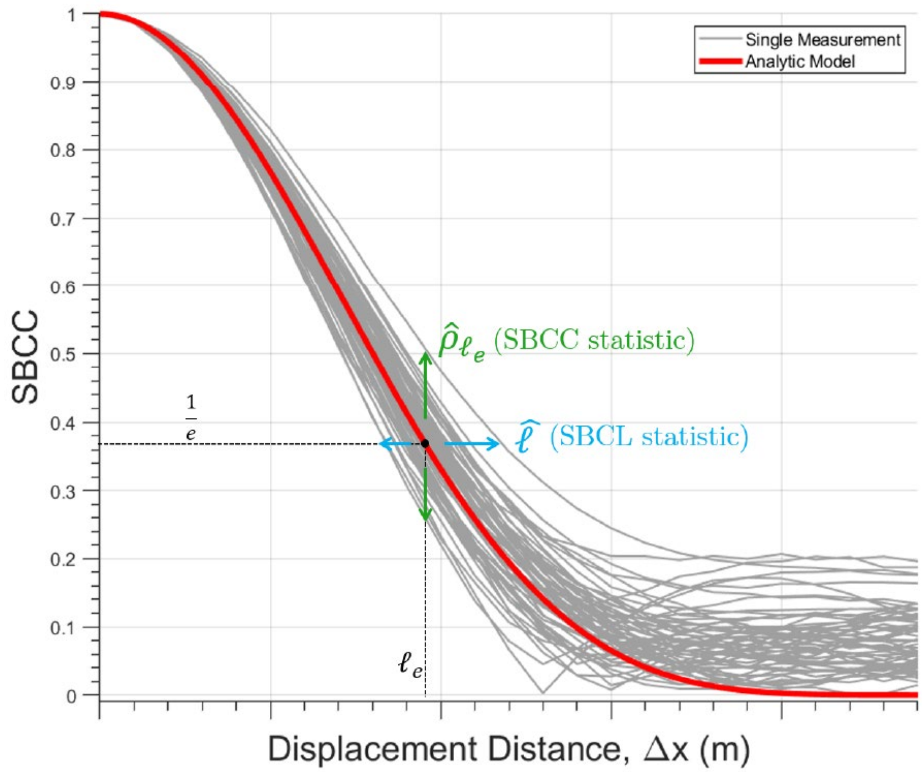


*Figure 1: This figure shows the relationship of the two developed coherence statistics, SBCC ($\hat{\rho}_{\ell_e}$), and SBCL ($\hat{\ell}$), to the expected THSC function (thick red line). Grey lines show single estimate of the THSC function. The SBCC statistic is equivalent to estimating the THSC function at a single displacement distance, $\Delta x = \ell$. This displacement distance is where the expected THSC function falls to 1/e. SBCL is a measure of the breadth of the THSC function where it falls to a level of 1/e.*

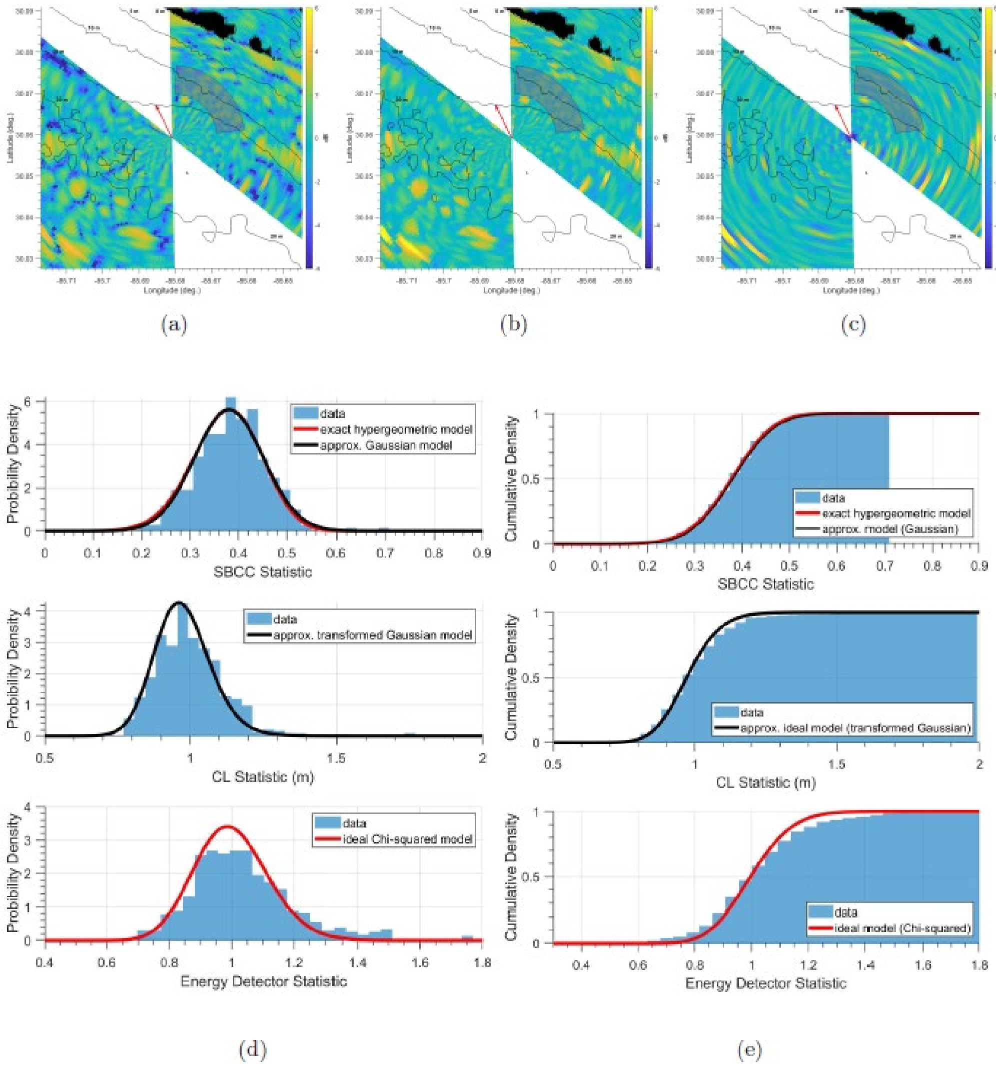


*Figure 2: Statistical model comparison of highly reverberant data from a benign littoral region. Polar plots (a) through (c) display statistics of interest in dB re E[$\eta_i$], where E[$\eta_i$] is the expected value of the statistic ($x_{SBCC} = 1/e$, $x_{SBCC} = 0.96$ m, and $x_{ED} = 1$ Pa$^2$). Plot (d) displays a statistical comparison of the analytic models developed in this work. Blue histograms represents data from the shaded region in polar plots (a) through (c); the left being PDFs while the right are the associated CDFs. The upper PDF/CDF pair is the SBCC statistic with a hypergeometric based uncertainty model shown in red, and a Gaussian approximation to the hypergeometric model in black. The center PDF/CDF pair is SBCL with transformed-Gaussian based uncertainty in black. The lower PDF/CDF pair is ED with ideal $\chi_{2n_i}$ uncertainty shown in red. Note for an acoustical benign region/return, the models fit quite well. Deviation from these models represent a more complex region that may constitute a region with significant clutter.*

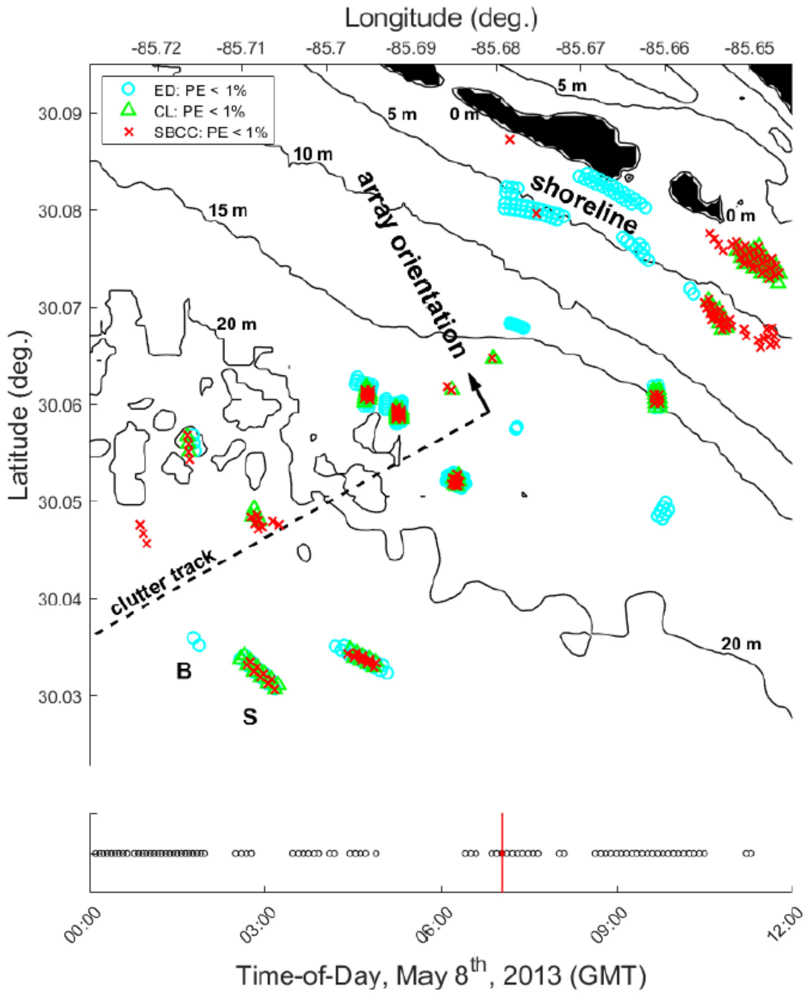


*Figure 3: Geospatially registered exceedances of pulse 50 of 84 pulses analyzed in this work. The three test statistics are shown using a 1% threshold estimated from data (roughly showing the spatial location of the highest 1% of the statistics). ED is shown using cyan circles, SBCL with green triangles, and SBCC using red x's. Lower portion of plot shows chronological order of pulses. "S" and "B" annotations are the wreck of the USS Strength and a sunken bridge span, respectively, each discussed by Lee et al. [5]. Very often, all three statistics have exceedances for compact scattering events such as these. However, for non-compact events such as the shoreline closest to the array, coherence statistics often do not have an exceedance while ED did. These results are the first experimental results to corroborate the compact vs. non-compact scattering region hypothesis developed for THSC statistics in this work.*

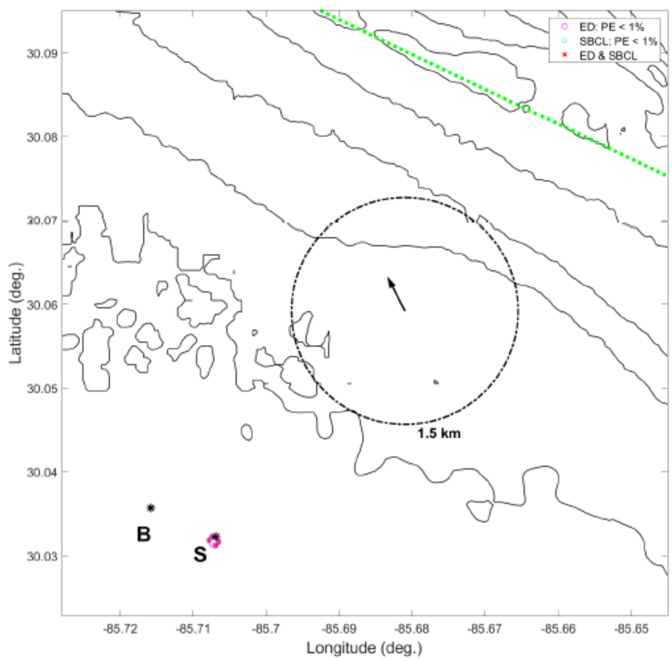


(a)

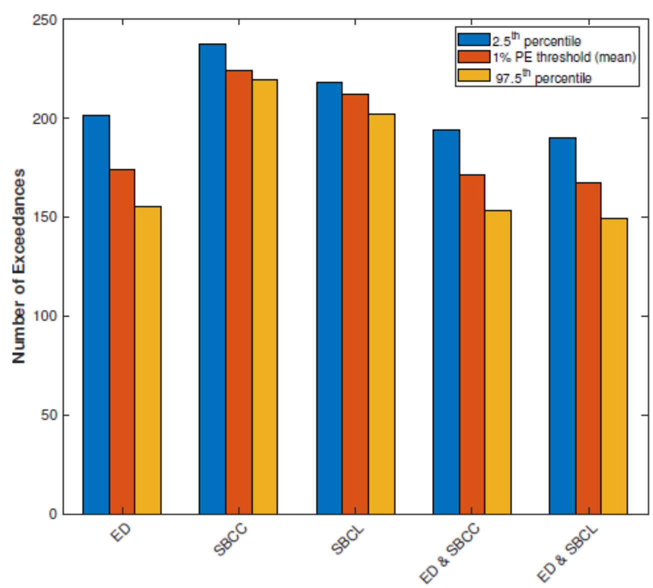


(b)

*Figure 4: Shipwreck exceedance analysis. Plot (a) shows exceedances for each statistic geospatially registered for all 84 pulses, while plot (b) provides a summary exceedance bar chart with 95\% CI. Composite statistics of similar number (within CI limits) to ED imply that ED and THSC statistics are essentially fully dependent for compact scattering events. Masking circle for ship roughly 150 m in diameter.*

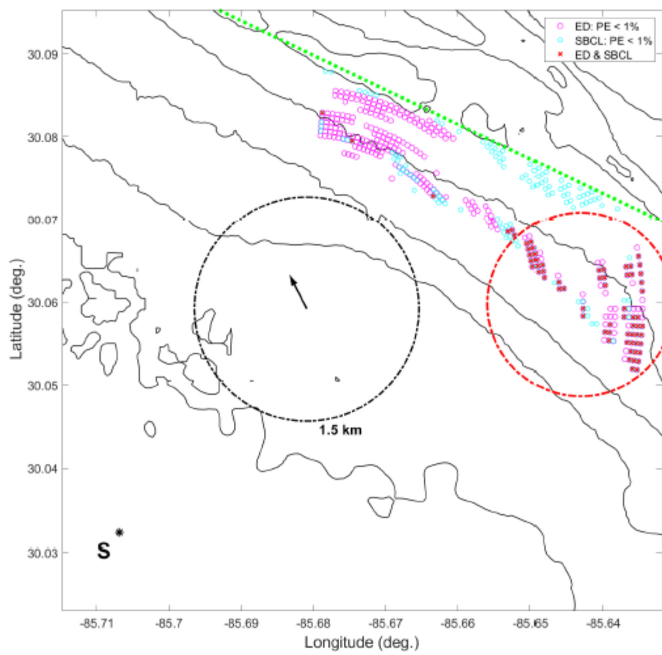


(a)

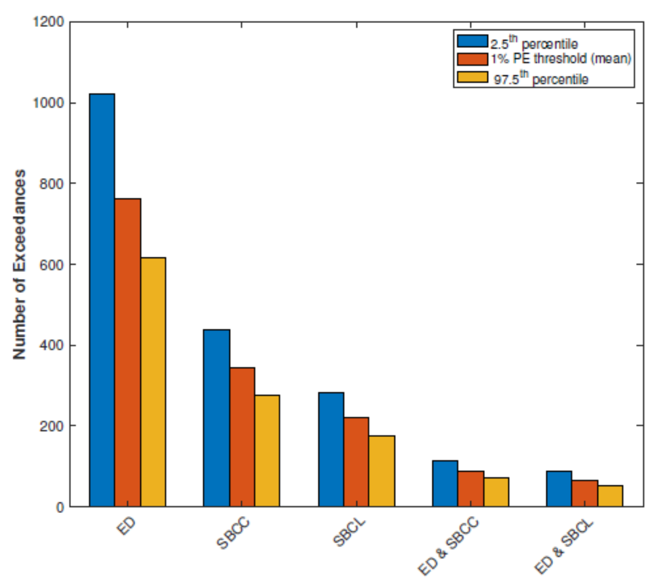


(b)

*Figure 5: Shallow-water exceedance analysis (depths < 7 m). Plot (a) shows exceedances for each statistic geospatially registered for all 84 pulses, while plot (b) provides a summary exceedance bar chart with 95\% CI. Composite statistics significantly less than ED imply that ED and THSC statistics are reasonably independent of one another. Red dashed circle shows known compact scattering events.*

## The 2017 Seabed Characterization Experiment (SCEX17)

A significant portion of this project was comprised of supporting data collection and geoacoustic analysis for the 2017 Seabed Characterization Experiment (SCEX17). In order to participate in the SCEX17, which took place during March-April of 2017, the FORA acquisition system required two significant hardware repairs to the array and a minor code update for the data recording system. First, the array's winch required an overhaul of the electrical and hydraulic systems. It was found that hydraulic system malfunctions during the 2015 Littoral Continuous Active Sonar experiment (LCAS15) caused several electrical components to overheat and the winch required a thorough overhaul to prevent future malfunction. Second, a repair of the fiber optic deck-cable to tow-cable connection was required. Teledyne Geophysical carried out this repair, but unfortunately the system still did not operate properly during the experiment and PSU had to temporarily splice and re-terminated the system during the experiment. Finally, minor acquisition software upgrade were required to allow contiguous files storage and a faster sampling rate due to the unique requirements of geoacoustic inversion measurements.

It should be noted that the thorough overhaul of the FORA winch was an investment moving forward for ONR-OA/PSU-ARL. This is because the FORA replacement array, THORA, has been mounted on this same winch. PSU-ARL contracted Electric Motor & Supply (EMS) in Altoona, PA to complete a full system overhaul of the winch control cabinet and Breon's Inc. of Pleasant Gap, PA to overhaul the 440V, 3-phase winch motor system. These companies overhauled the winch motor and completely rewired the control cabinet electrical system including electrical and hydraulic safety switches. They also verified proper operation of the hydraulic system. Speaking to the work of these companies, the FORA winch system performed flawlessly throughout the SCEX17 experiment. These companies are also local to PSU-ARL if any further work concerning the winch is required in the future.

During the SCEX17 experiment, the FORA team had a rough start due to the prior mentioned fiber optic trouble. However, PSU-ARL managed to troubleshoot the FORA and repair the system in a timely manner to complete the measurements required for this trial. Additionally, the FORA team provided considerable support of Charles Holland's experimental goals, acquiring and operating a specialized source and mooring equipment for this effort. Acoustic data was collected by the team using a combination of the cardioid aperture of the FORA and various autonomous data logging systems for a combined total of ~900 GB of raw hydrophone data in the interest of geoacoustic inversion research. This trial was a wonderful collaboration with many very capable research teams. PSU-ARL is thankful to have been involved with this work! Experimental report is the 4$^{th}$ attachment to this report.

## Trade Study for FORA Refurbishment\Replacement

The PI was tasked with providing recommendations for the best way forward for the FORA system in terms of both cost and scientific utility. This section describes the results of these efforts. Four possible ways forward were initially proposed:

1) Continue with the legacy FORA system, but applying fixes as needed prior to planned experimental efforts. (*Ruled out due to the increasingly unreliable nature of FORA during sea trials.*)
2) A major refurbishment of the current FORA system working with original design company. (*Ruled out due to the cost of refurbishment exceeding that of replacement.*)

3) Traditional line array replacement of the FORA, recycling any possible materials of the original system. This option may or may not have use the company who originally designed the FORA system.
4) FORA system replacement using autonomous time-synced acoustic recorders allowing flexible acoustic aperture. These recorders may be similar or equivalent to the distributed hydrophone modules used by Dr. Peter Worcester at Scripps Institution of Oceanography. (*Ruled out due to the required timing and localization constraints of mid-frequency beamforming.*)

Weighing scientific utility and cost efficiency of each option, PSU found the most appropriate method to move forward with was to attempt to secure funding for a traditional line array replacement (list item 3). However, it was decided to recycle the cabling and winch system of the legacy FORA system to help reduce development cost, as these are high cost components. PSU worked with several array manufacturers to find the most cost efficient method to attain a system with high scientific utility for the OA community. By a large margin, the most cost efficient source for a new towed line array was by working with the engineering group at the Centre for Maritime Research and Experimentation (CMRE) in La Spezia, Italy. PSU-ARL submitted a DURIP for the purchase price of a modular three octave towed array, and this DURIP was funded in 2019. The next section will describe the new array. Please see the attached factory acceptance test documentation (attachment 5) for further detail on this new system and acceptance testing/results.

**Development and Delivery of the FORA Replacement Array (dubbed the THORA)**

Please note this task is closely associated with an ONR-OA funded DURIP proposal: 000141912183— *Modular Towed Array for Acoustic and Oceanographic Research*. DURIP fund allowed PSU to acquire a FORA replacement towed array, while this project grant provided funding for the PI and FORA technician to aid in planning and monitor the progress of the new array's development. This research acquisition system will provide significant advancements to PSU-ARL and ONR-OA's experimental capabilities.

While delivery of the FORA replacement acquisition system was significantly delayed due to long component lead times and manpower issues related to COVID-19, fabrication and laboratory acceptance tests (FAT) were completed in late 2021. CMRE completed all acceptance testing and the array passed all required parameters. PSU has also committed final payment to CMRE. This marks the finish line for ONR-OA/PSU-ARL having a new towed research array. However, since this system has only been bench tested thus far due to available funding, there is no question wet testing is very much required to fully verify and characterize the array for future experimental use. Regardless, PSU-ARL has made highly significant advances toward maintaining PSU-ARL and ONR-OA's experimental capabilities during this funding period.

The new array was able to meet the following list of specifications and requirements:

- A large diameter (77 mm), forward nested acoustic module 50.6 m in length
- Acoustic apertures cut for 1, 2, and 4 kHz

- 192 hydrophones (sensitivity nominally -201 dB re 1V/uPa)
- A large diameter (77 m), 25.3 m length, forward vibration isolation module (VIM)
- 4 Non-acoustic sensor nodes (NAS) with roll, pitch, yaw, depth, and heading measurements (< 1 percent accuracy heading sensors)
- 16 kHz nominally flat hydrophone response band
- Single pole high-pass filter on each channel with corner frequency (-3 dB) at 70 Hz
- Selectable channel gain up to 32 dB
- Signal digitization rate up to 24 kHz
- Maximum of 10 knot tow speed
- No multi-hydrophone summed channels (common in operational arrays) to allow better TOA analysis capabilities
- Array self-noise less than SS0
- Maximum depth rating of 500 m (with a safety factor of 1.5)
- A modular design where additional acoustic apertures can be added later if scientific interest and funding allow

Figures 6 and 7 show the new array in CMRE's workshop, and the hydrophone layout of the new system, respectively.

*Figure 6: Images of the of the new, fully assembled THORA array on the test bench (right) and partially coiled onto a spool (left). The system is intended to remain at CMRE until an engineering wet test of the new acquisition system can be scheduled.*

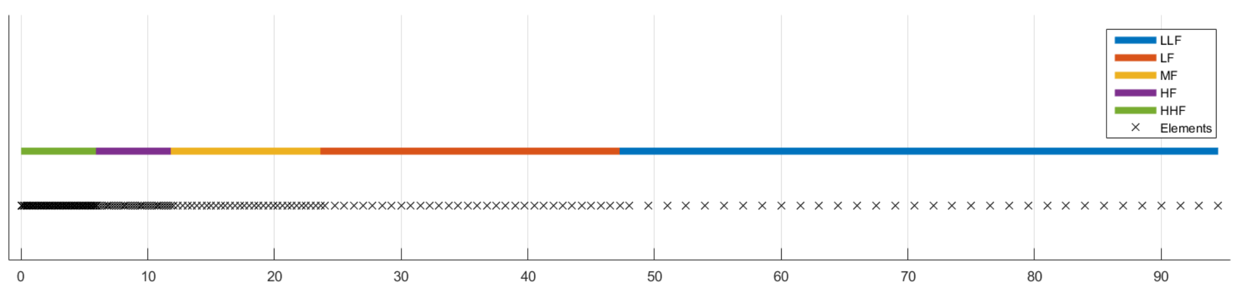


*Figure 7: Forward-nested array design— this design is viable for manufacturing and upgradability, as well as measurements. It allows closely spaced elements to remain within a single array module reducing the number of required bulkhead connections and complex wiring. It also allows more array modules to be added in later years.*

**Planning for a THORA Engineering Trial**

In 2019, ONR-OA approved funding to support ARL-PSU and the CMRE in the procurement of a replacement for the aging and increasingly unreliable FORA acquisition system. This funding supported hardware development and laboratory testing of a three aperture, mid-frequency (1000, 2000, and 4000 Hz center frequencies) modular acoustic towed array. Hardware deliverables included the array, a forward vibration isolation module (VIM), and a roughly 1 km winch system. Laboratory (dry) verification, factory acceptance testing, and delivery[1] of this system from CMRE to ARL-PSU was recently completed, and ARL-PSU believes we now have a functional and very versatile towed array system. Unfortunately, no at-sea wet testing was possible with funds available to date. This section outlines a thorough in-water engineering test for the new three-octave research array (THORA).

The engineering test outlined below was developed through discussions between ARL-PSU and CMRE. The first test component (list item 1) involves a full acoustic (magnitude and phase) response characterization and is expected to take 1 day to carry out in good weather conditions. This test would also verify the array's relative and global timing characteristics. Components 2 and 3 (list items 2 and 3) of the engineering trial would then take roughly 2 days each. The goals of these latter components are to test and characterize hydrodynamic and noise characteristics of the array, in addition to providing ARL-PSU and CMRE valuable experience with the new acquisition system. A dedicated engineering test of all array components/features is expected to take 5 trial days and could be completed relatively close to CMRE (La Spezia, Italy). This close proximity to CMRE would reduce ship-time and funding requirements, and allow quick-turn hardware corrections to the array, if required. However, due to the new array being based on previously developed and proven array technology, CMRE and ARL-PSU believe the new system is unlikely to have substantial hardware defects.

Engineering Trial Components:

1. *Acoustic characterization*

   To measure free-field hydrophone response, timing characteristics, and dynamic range, this test must be performed in relatively deep water. Water depth must be great enough that it (and weather conditions) allow the THORA to be safely deployed in a vertical configuration from the stern of the ship (>250m). Array tail-weight, weather, and oceanographic conditions should be chosen to put minimal stress on the array. Station keeping capabilities of the RV should be used to maintain a linear (vertical) array shape within practical limitations. ARL-PSU will deploy a calibrated omnidirectional (GeoSpectrum Technologies Inc. M18-6) source attached directly to the array tow cable slightly above the vibration isolation module (see Fig. 1). A series of short (<100 mS), low-level, CW tones over the operational band (~0.05-12 kHz) of the array will then be transmitted to measure array response. Higher level CW tones at 1 kHz will be used to verify the nominal acoustic clipping level of the system and aid in dynamic range characterization. A series of wide-band LFM's will be transmitted to verify the relative timing and phasing characteristics of the array as well as the global timing of the transmit/receive-array acquisition systems (THORA and transmit systems GPS synced). Additionally, a calibrated hydrophone (icListen-HF) may be attached to the tow cable to provide verification of source levels, and light bulb implosions may be used as a second source.

[1] The acquisition system has been "delivered" to ARL-PSU in the sense that it has passed all pre-determined factory acceptance tests and is ready for shipment to the U.S.A. However, it physically remains at CMRE in the hopes of completing a full engineering wet test prior to committing the financial resources required to ship the system stateside.

There are many areas with acceptable water depths for this work a short steam from CMRE (La Spezia, Italy). This test is expected to take less than ½ day *on-station* to complete, assuming good weather conditions. A single ship-day is expected to be sufficient to complete this test assuming limited weather and technical difficulties.

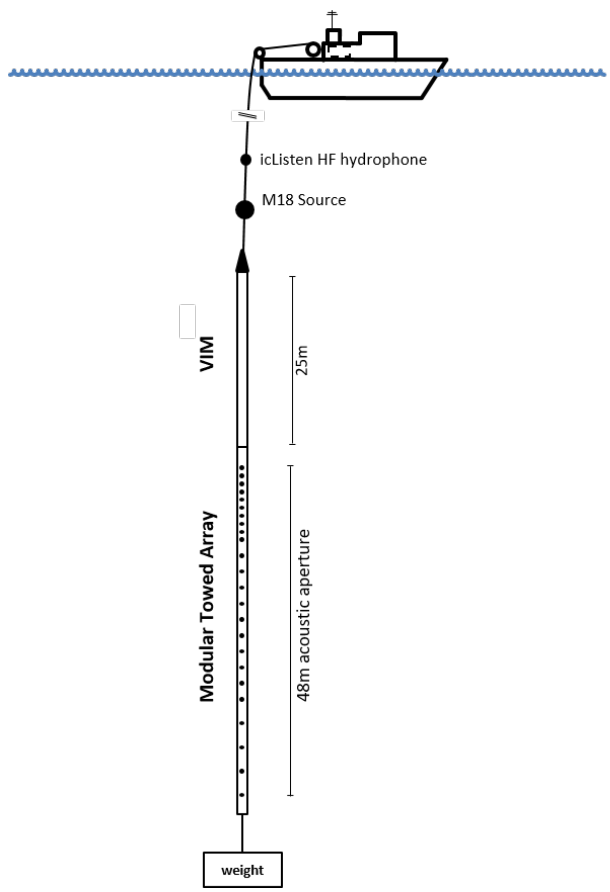


***Figure 1: Geometry for line array calibration and timing test. Weather permitting, this configuration will allow a free-field calibration and absolute timing check in deep water (> 250 m).***

2. *Tow dynamics and non-acoustic sensor testing*

This portion of the engineering trial will allow ARL-PSU/CMRE to become familiar with the tow dynamics of the new acquisition system (tow depth vs. speed-through-water, and roll, pitch, yaw, stability, etc.) and verify the complete operation of non-acoustic sensors (NAS). Initially, linear tows at constant speed/array depth will be used to determine (from NAS data) if array trimming is required (by adding or draining oil). Retesting/trimming will then be carried out until the array appears to tow stability and horizontally within the water column. A series of common tow patterns/maneuvers will then be carried out (e.g., linear/lawnmower patterns, Williamson turns, circle maneuvers) while NAS sensor data is monitored for common trends and variance in array tilt, depth, course, roll, etc. A comprehensive table of tow depth based on cable scope and speed through water for linear tows will be recorded. Ship passes by a moored echo repeater/pinger (furnished by CMRE) transmitting broadband LFM's will allow verifications of NAS sensor data such as depth and pitch, while towing at greater ranges from the source will allow verification of beamforming/bearing localization capabilities.

This component could potentially take place in conjunction with the science objectives of a towed array experiment. In a dedicated engineering trial, these tests are expected to require 2 days.

3. *Hydrodynamic noise characteristics*

At the relatively slow tow speeds (2 – 10 kts) the THORA was designed for, the large diameter array is expected to have relatively low flow noise. However, to verify this, flow noise should be part of the initial engineering assessment of this system. Flow noise can be difficult to distinguish in experimental data because of the impact of both ambient and ship noise. While highly precise measurements of flow noise characteristics are out of the scope of this work, it is desirable to record data that will provide useful engineering estimates of the flow noise associated with the new towed array. These estimates will be highly valuable in array verification and future experimental planning.

A series of short, constant speed ambient-noise tows between 2 and 10 kts (e.g., 2, 5, 8 kts) will be carried out in relatively deep water. Deep water will allow the array to be deployed at a farther range from the tow vessel (compared with shallow water) to minimize the impact of ship noise. Additionally, at the end of each constant speed run, ship and diesel engine speed may be "cut" (assuming deep enough water depth to allow for array drop) and noise will be monitored over the unpowered deceleration of the ship and array. By analyzing constant underway speed runs, deceleration ramps, and flow-noise model fitting, it will be possible to estimate empirical flow noise curves for common tow speeds over much of the band of interest. An alternative to this testing method might also be to use the NRV Alliance's gas turbine propulsion system during this test. These engines are three decks above sea level and typically found to be much quieter than diesel propulsion. Real-time wavenumber vs. frequency plots will be used to aid in identification of specific noise sources causing interference.

In conjunction with a science trial these measurements might take place during transition to science tracks. In a dedicated engineering trial, these tests are expected to require 1 to 2 days.

## IMPACT/APPLICATIONS

Sonar clutter is a significant operational difficulty for the fleet, especially within the shallow-water littoral environment. Characterizing sonar statistics is key to finding ways of quickly distinguishing between clutter types and mitigating. This will lead to lower false alarm rates for sonar systems.

The experimental work undertaken during the SCEX17 and later analysis provided a wealth of data in the interest of geoacoustic inversion research. This research will provide improved understanding of the impact of muddy seafloors on acoustic propagation and reverberation, and its impact on sonar.

The FORA replacement acquisition system will provide new towed array acquisition capabilities for the OA community moving forward. This system will be highly flexible in measurement capabilities, and is expected to be far more reliable than the FORA during its final several experiments. Its modular design also allows the addition of measurement capabilities in the future, if scientific interest and funding allow.

The cardioid array technology that the FORA system offered provided novel improvements in towed array data collection by greatly lessening the effects of ambiguous arrivals of traditional line arrays. The data collected and processing algorithms designed during this work may provide a baseline for future naval applications.

## RELATED PROJECTS

***Modular Towed Array for Acoustic and Oceanographic Research***
Contract Number: N00014-19-1-2183, PI: Chad Smith
DURIP supporting ARL-PSU in acquisition of a new ONR towed line array.

***Acoustic wave dispersion and scattering in complex marine sediment structures***
Contract Number: N00014-14-1-0224, PI: Charles Holland
Analysis of FORA and other acoustic data taken during SCEX17 in the interest of geoacoustic inversion using wave dispersion estimation.

***Analysis of Spatial Correlation for Classification and Clutter Mitigation***
Contract Number: N00024-18-D-6401, DO: N0002418F8421, PI: Chad Smith
This work seeks to utilize the physical-statistical models developed in PSU-ARL's OA analysis and apply them in real-world clutter mitigation/classification applications.

## REFERENCES

[1] Smith, Chad M. (2021). Modeling and analysis of transverse horizontal spatial coherence statistics for reverberation-limited active littoral sonar (Doctoral dissertation, The Pennsylvania State University, State College, PA, USA). Retrieved from: https://etda.libraries.psu.edu/files/final_submissions/23803.

[2] Holland, C. W., Smith, C. M., Lowe, Z., & Dorminy, J. (2021). Seabed observations at the New England Mud Patch: Reflection and scattering measurements and direct geoacoustic information. IEEE Journal of Oceanic Engineering.

[3] Jackson, D. R., & Moravan, K. Y. (1984). Horizontal spatial coherence of ocean reverberation. The Journal of the Acoustical Society of America, 75(2), 428-436.

[4] Mallart, R., & Fink, M. (1991). The van Cittert–Zernike theorem in pulse echo measurements. The Journal of the Acoustical Society of America, 90(5), 2718-2727.

[5] Lee, W. J., Tang, D., Stanton, T. K., & Thorsos, E. I. (2018). Macroscopic observations of diel fish movements around a shallow water artificial reef using a mid-frequency horizontal-looking sonar. The Journal of the Acoustical Society of America, 144(3), 1424-1434.

# ATTACHMENT 1

The Pennsylvania State University
The Graduate School

# MODELING AND ANALYSIS OF TRANSVERSE HORIZONTAL SPATIAL COHERENCE STATISTICS FOR REVERBERATION-LIMITED ACTIVE LITTORAL SONAR

A Dissertation in
Acoustics
by
Chad Mahlon Smith



Submitted in Partial Fulfillment
of the Requirements
for the Degree of

Doctor of Philosophy

May 2021

The dissertation of Chad Mahlon Smith was reviewed and approved by the following:

Thomas B. Gabrielson
Research Professor of Acoustics
Dissertation Co-advisor
Chair of Committee

Daniel C. Brown
Assistant Research Professor of Acoustics
Dissertation Co-advisor

Charles W. Holland
Research Professor of Acoustics

Russell C. Burkhardt
Assistant Research Professor of Acoustics

Timothy J. Kane
Professor of Electrical Engineering

David L. Bradley
Professor Emeritus of Acoustics
Special Signatory

Victor W. Sparrow
United Technologies Corporation Professor of Acoustics
Director of Graduate Program in Acoustics

# Abstract

Active sonar systems operating in the littoral environment are often reverberation-limited. These environments are regions where sonar operation is limited by sonar system self-noise due to reverberation arising from waveguide boundary interactions, acoustic scattering, and two-way propagation. This self-noise reduces the effective signal-to-noise ratio of the sonar platform and can lead to excessive false alarms, commonly referred to as sonar clutter. Clutter is caused when the sonar processing system mistakes signals from the environment or of anthropogenic origin for targets of interest. Clutter is found in all environments, but shallow-water littoral regions are especially challenging due to excessive reverberation, increased anthropogenic and biologic activity, as well as significant bathymetric, geoacoustic, and oceanographic variability. This dissertation will discuss the development, physical interpretation, and experimental assessment of sonar statistics related to the transverse horizontal spatial reverberation coherence of a directional active sonar platform (a subaperture beamformed line array) within the reverberation limited littoral environment. Primary goals are to theoretically characterize and experimentally verify physical-statistical models for diffusely reverberant scenarios, and quantitatively assess whether there is information about the azimuthal distribution of scattering within wide, low-resolution sonar cells for certain environmental scenarios. If so, these statistics may provide complementary information to more commonly used active sonar statistics (e.g., signal envelope, intensity) from the standpoint of environmental assessment, clutter characterization, and statistical processing.

In this work, a set of spatial coherence statistics are developed for analyzing data from a 1-dimensional, pseudo-monostatic, active sonar platform and applied to a broadband (900 Hz bandwidth), mid-frequency (3150 Hz center frequency), moored, line-array receiver system within a complex littoral environment. Each coherence statistic provides a level of control over sampling uncertainty through temporal averaging, allowing investigation of the impact of differing environmental and platform conditions such as irregular bathymetry and beampattern parameters. For reference, a comparative signal-intensity based statistic is also developed with similar temporal averaging length and incoherent noise normalization power. A simple point-scattering model is used to describe the concept of spatial coherence and provide straightforward examples that outline the complementary information content of coherence statistics in specific geometric scattering scenarios. The van Cittert-Zernike theorem and sampling theory are then invoked to derive analytic physical-statistical models of the expected correlation function, and probability distributions of each statistic under an assumption of diffuse reverberation. A ray-based computational reverberation model is then developed in order to simulate

more realistic littoral examples and compare general trends with experimental data. Finally, experimental data from a moored source-receiver geometry are analyzed to ensure minimal pulse-to-pulse dynamics, allowing analysis of the influence of stationary bathymetric and anthropogenic clutter types over many pulses. A statistical exceedance analysis is used to show empirically that spatial coherence statistics hold information that can be complementary to common signal statistics for specific types of scattering events.

# ATTACHMENT 2

# Seabed Observations at the New England Mud Patch: Reflection and Scattering Measurements and Direct Geoacoustic Information

Charles W. Holland, Chad M. Smith, *Member, IEEE*, Zackary Lowe, and Jim Dorminy

***Abstract*—Seabed reflection and scattering measurements were conducted at the New England Mud Patch to better understand the acoustic properties of fine-grained (muddy) sediments. The measurement philosophy and the measurements themselves are summarized. In addition, geoacoustic information accessed directly from the data in the time and frequency domains is presented. The main result is the existence of an angle of intromission. This observation proves that the mud sound speed is less than that of the water and yields a sediment sound speed ratio 0.9865 with outer bounds {0.985 0.989}. Another result is the observation of strong scattered arrivals from within the mud volume at/near normal incidence but not at low grazing angles. These are likely due to anisotropic sediment heterogeneities with a large horizontal to vertical scale. Evidence is also presented for a highly heterogeneous mud–sand horizon with lateral variability down to scales of order meters. Finally, the reflection measurements successfully capture Bragg interference patterns. Their importance is their substantial geoacoustic information content, which can be accessed by several inversion methods.**

***Index Terms*—Reflection, scattering, seafloor, sediment acoustics.**

## I. Introduction

MARINE and terrestrial life exploit sound to communicate and sense the ocean environment. Often, the seabed properties have a profound influence on sound propagation. The broad motivation for the multinational Seabed Characterization Experiment, SBCEX17, was to better understand acoustic propagation through fine-grained muddy sediments. Compared to granular (sandy) sediments, much less is known about the acoustics of fine-grained sediments. As one evidence of this, until very recently [1], there was no first-principle model for sound propagation through fine-grained sediments, whereas for granular sediments, a model [2] has been in existence for six decades with a large number of variants and extensions. In accord with the paucity of models, there have been significantly fewer sediment acoustic experiments conducted in muddy than sandy sediments.

The primary long-term science objective of the research described here is to measure the intrinsic frequency dependence of the sound speed and attenuation in muddy sediments from a few hundred hertz to a few kilohertz. Some discussion is warranted concerning experimentally inferred frequency dependence compared to that predicted by theoretical sediment acoustic models. Theoretical models of the frequency dependence of sound speed and attenuation treat a *homogeneous sample*—at scales much larger than the individual grains. However, in an at-sea measurement, it is often challenging to isolate a homogeneous sediment sample and obtain the intrinsic frequency dependence. One approach for isolating a homogeneous sample is through mechanical sampling, e.g., a coring device, identifying a uniform region in the cored material and then conducting measurements on that subsample. This approach has significant disadvantages: 1) mechanical sampling introduces changes to the sediment, and most especially to fine-grained sediments which have a fragile structure that is easily altered; 2) it is usually difficult/impossible to determine what the sampling effects were, and "undo" them in the analysis; and 3) the resulting subsample sizes only permit measurements of sound speed and attenuation at high frequencies (order hundreds of kilohertz), since the dimension of the subsample is generally small, of order centimeters.

An alternative approach is to use acoustic remote sensing of the sediment geoacoustic properties, and then "isolate" a homogeneous sample. To achieve this, numerous potentially confounding frequency-dependent mechanisms must be separated to obtain unbiased intrinsic sound speed and attenuation. These include nonsediment related mechanisms, such as effects of scattering from sea surface roughness/bubbles, effects of space-/time-dependent ocean dynamics, e.g., internal waves, and scattering from biologics. More subtly, sediment-related structures, if not detected and accounted for, also lead to biases. The structures include sound speed and attenuation gradients due to increasing overburden pressure or smoothly changing porosity (e.g., [3]), discrete layers greater than $\sim\lambda/8$, and seabed lateral variability. In the New England Mud Patch (NEMP) environment, these are considered to have primary effects on the frequency dependence of sound speed and attenuation. Secondary effects include effects of shear waves and associated

Manuscript received September 22, 2020; revised January 5, 2021; accepted March 23, 2021. This work was supported by the Office of Naval Research, Ocean Acoustics. *(Corresponding author: Charles W. Holland.)*

**Guest Editor: D. Knobles**.

Charles W. Holland is with the Electrical and Computer Engineering Department, Portland State University, Portland, OR 97201 USA (e-mail: charles.holland@pdx.edu).

Chad M. Smith, Zackary Lowe, and Jim Dorminy are with the Applied Research Laboratory, Penn State University, State College, PA 16801 USA (e-mail: cms561@psu.edu; zgl5003@psu.edu; jdd10@psu.edu).

Digital Object Identifier 10.1109/JOE.2021.3070028

gradients; secondary because the shear wave speed in muddy sediments is quite low, a few tens of meters per second [4], [5]. Other possible confounding mechanisms are scattering from interface roughness and sediment volume inhomogeneities.

Given the mechanisms above that need to be teased apart to recover the intrinsic frequency-dependent sound speed and attenuation, additional science questions must be addressed.

1) How do the geoacoustic properties vary vertically? This is needed to isolate and quantify properties of individual homogeneous layers.
2) How do the geoacoustic properties vary laterally at decimeter to kilometer scales? This can be divided into the following:
   a) small-scale heterogeneities (sediment volume and interface roughness), which cause scattering;
   b) large-scale lateral heterogeneities or geoacoustic range dependence.

Therefore, to compare observations with theory, it is critical that the theoretical basis (wave propagation through a homogeneous sample) is respected as strictly as possible for the observations. Thus, considerable care is required in designing the measurements.

A primary short-term goal for the present work is to address the important question of the sound speed of the mud near the water–sediment interface. This is a deceptively challenging measurement, as indicated by the wide range of sound speed ratio estimates to date at the NEMP, from 0.945 to 1.026 over the band 40–1000 Hz (see [6, Fig. 7]) from more than a dozen different measurements, corresponding to mud sound speed disparities up to ∼120 m/s. Thus, at this stage, it is not even clear whether the mud has a sound speed less than or greater than that of the water. As another data point, the commonly used Bachman–Hamilton empirical relations [7] using the porosity of the mud, 0.60 [8], yields a sound speed ratio of 1.04, which further increases the possible range of sound speed values.

In measurements reported here, the data show an unambiguous angle of intromission of 8°. The mere existence of an angle of intromission means that the sound speed of the sediment *must* be less than that of the water column. We term this "direct" geoacoustic information—no models or inversion are required. Of course, a theory of wave reflection is required, but the conclusion (sound speed ratio less than 1) is independent of whether the model of the sediment is a fluid, or a viscoelastic solid, or a poro-viscoelastic solid, or whether the wavefield is modeled as a plane wave, or spherical wave. If a model is coupled to the observation, further quantitative information can be had, namely the sound speed ratio.

Despite the considerable value of the angle of intromission for probing *in situ* fragile muddy sediments, measurements are exceedingly rare. To the authors' knowledge, there are no published angle of intromission measurements on the continental shelf of the United States, nor yet the entirety of North America. This scarcity may not be because muddy sediments exhibiting an angle of intromission are scarce, but rather because the measurements are challenging. It should also be pointed out that not all muddy sediments are expected to exhibit an angle of intromission. Measurements are required. The angles of intromission measurements at the NEMP presented here provide unique and valuable understanding of the sound speed in the upper few meters of sediment.

This article is organized as follows. In Section II, the measurement philosophy is further discussed along with the specific experiment designs to address the science questions. In Section III, direct geoacoustic information is presented and discussed, including observations of the angle of intromission and critical angle. In Section IV, time-domain measurements are presented and discussed in terms of both vertical and lateral geoacoustic properties. Section V summarizes the results.

## II. Measurements

A common and powerful geoacoustic inference technique is to exploit waveguide physics, where source and receiver are widely separated, kilometers to tens of kilometers in shallow water. One challenge faced by the waveguide methods is that oceanographic variability can cause contaminating effects in the data that are difficult to separate from seabed effects. To obviate this difficulty, the SBCEX17 experiment was specifically executed during winter months when the water column is well mixed. A remaining oceanographic feature that could cause difficulty for waveguide seabed inference methods is scattering from the sea surface and/or bubble clouds in high sea states and frequencies above a few hundred hertz. Another challenge to the waveguide measurement method is 1) that the seabed is variable over kilometer to tens of kilometer lateral scales, 2) that widely separated source and receiver observations do not have the geoacoustic information content to recover the seabed lateral variability; and 3) when the known or unknown lateral variability is ignored, the resulting estimated geoacoustic properties are biased (e.g., [9] and [10]). Another challenge is that there is generally insufficient geoacoustic information content in the data to recover the details of the depth-dependent geoacoustic properties of the seabed. This is due in part to sensitivity of the data to the ocean water column, in part to smearing of the information in range, and in part to the low frequencies generally employed. As but one example, the geoacoustic information content in long-range propagation data are insufficient to directly detect the angle of intromission and in fact are relatively insensitive to the sediment sound-speed ratio near unity. This can be seen from ten widely varying estimates of sound-speed ratio, 0.945–1.026, from 40- to 1000-Hz long-range propagation data sets (see [6, Fig. 7], which includes only sound speed ratio estimates at/near the water–mud interface).

In summary, it is difficult using long-range acoustic data to isolate a homogeneous portion of the seabed from all other mechanisms, which is needed for measuring frequency-dependent sound speed and attenuation.

To reduce these difficulties, experiments were designed/conducted with short source–receiver offsets. That is, instead of using waveguide physics, we exploit the physics of a single interaction with the seabed. Typically, the insonified lateral region was of order ten to a hundred meters. The short distance of the path through the water column and small seabed footprint greatly reduces the contaminating effects described

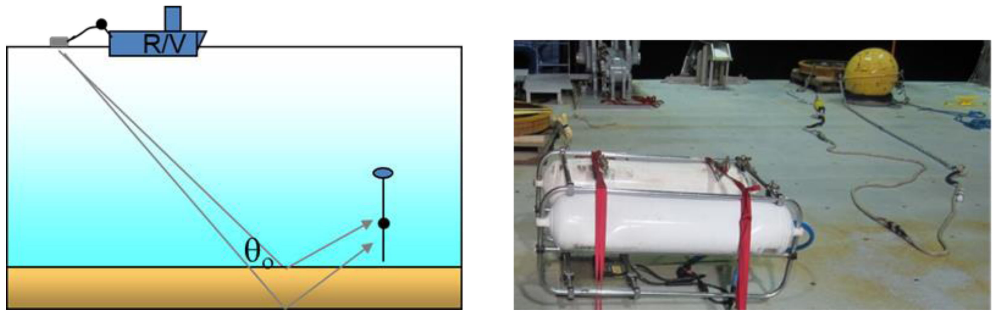


(a) (b)

Fig. 1. (a) Wide-angle seabed reflection experiment cartoon showing the broadband source towed behind the research vessel and the bottom-moored receive hydrophone string and (b) source catamaran (foreground) with source plate (behind the red strap on the left) and the receive mooring with yellow float next to the ballast (train wheel) and hydrophones attached to the mooring rope.

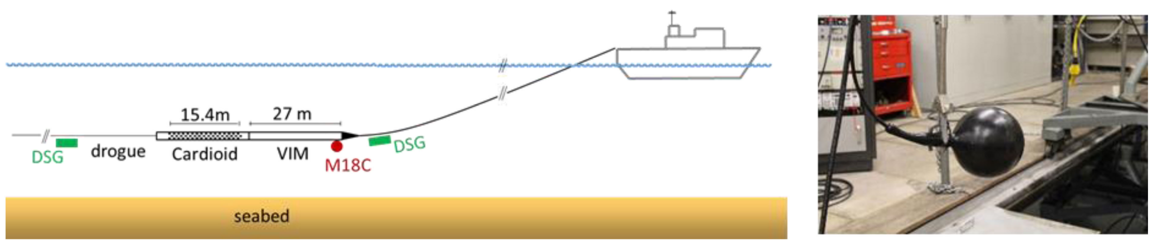


(a) (b)

Fig. 2. (a) Cartoon of seabed interaction experiment with a towed M18C source and cardioid receive array. The moving-source–moving-receiver experiment yields data from which 2-D geoacoustic properties (depth in the seabed and offset along a transect) can be obtained as well as scattering measurements. The distance from source to first cardioid triplet is 30 m. Two self-recording hydrophones (DSG) were mounted to the cable and drogue ~5 and 112 m, respectively, from the source. (b) M18C 6-in diameter source in the lab before calibration.

above; in consequence, the sensitivity of the measured signal to the geoacoustic properties is amplified. The sensitivity to geoacoustic properties is further enhanced by probing the seabed not only below the critical angle but also above it, where the reflected pressure contains greater geoacoustic information layer by layer, especially attenuation. Generally, geoacoustic information content increases with increased angular range and with increased frequency range (bandwidth). This is true for both reflection and scattering data. At very low grazing angles, neither the scattering cross-section (which approaches zero) nor the reflection coefficient (which approaches unity) has significant information content. Since theory shows that the seabed scattering cross-section is a strong function of the seabed reflection coefficient, the experiment design sought to jointly maximize geoacoustic information content for reflection and scattering measurements.

The experiments were designed to address the two science questions (listed in Section I) with two kinds of experiment geometries. To address sediment vertical variability, a broadband source is towed in radials centered at a bottom-moored receiver [see Fig. 1(a)]. Data from this experiment yield the reflection coefficient as a function of angle and frequency; analysis yields the vertical, or depth-dependent geoacoustic properties laterally averaged over about a water depth. To obtain sediment lateral variability, a source and a receive array are towed near the seabed [see Fig. 2(a)]. Analysis of these data yield: 1) the depth- and lateral-dependent geoacoustic properties of the seabed with a resolution of about 0.5 and 10 m, respectively, over a track extending tens of kilometers; and 2) roughness spectra at various interfaces and sediment volume heterogeneity spectra. For ease of reference, these two experiments will be denoted as 1-D (aimed at determining the depth-dependent geoacoustic properties) and 2-D (aimed at depth- and laterally dependent geoacoustic properties).

The locations of the experimental sites were chosen collaboratively with other scientists from the SBCEX community (e.g., see [6]), such that multiple observational methods and inference techniques could be brought to bear at the same locations. Fig. 3 shows the experiment area on the NEMP along with the 1-D experiment sites (green and cyan circles), which sample various mud thicknesses. At the VC31-2 site, the mud was only a few meters thick, whereas at the SWAMI site near the thickest region of the Mud Patch, the mud thickness was ~10 m. The former site is named for its core designator, whereas the latter site was named for proximity of the ARL-UT SWAMI array (though the ARL-UT SWAMI array was not used as a receiver for the reflection measurements). Thus, the term "SWAMI site" used in this article always refers to the reflection measurement location ~1 km WNW of the ARL-UT SWAMI array. The site in the north-east corner used a 64-hydrophone 1-km-long horizontal array (FFI, Kjeller, Norway) on the seabed as the receiver. Two traverses were performed, along (East–West) and perpendicular (North–South) to the FFI array. The mud thickness at the FFI site was ~5 m.

This article has been accepted for inclusion in a future issue of this journal. Content is final as presented, with the exception of pagination.



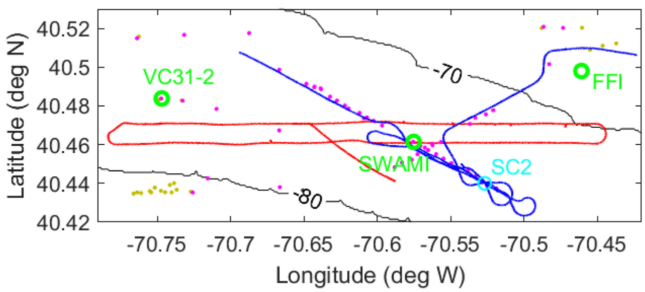


Fig. 3. Map of experiment area with bathymetry (m), cores (dots), wide-angle reflection (1-D) measurements with a fixed receiver (four circles) and source-towed array (2-D) tracks on March 30, 2017 (red) and April 3, 2017 (blue). The 1-D measurements were performed with a broadband incoherent source (green) and a M18-C coherent source (cyan). The receiver for the VC31-2, SWAMI, and SC2 sites was a short bottom-moored hydrophone string, and for the FFI site (green), it was the FFI array.

Along the 2-D experiment tracks, two equalized linear frequency modulated (LFM) 0.25-s down-sweep pulses were broadcast, from 6 to 1 kHz and 6 to 0.5 kHz. Each pulse type had a 1-Hz repetition rate and the two pulses were interleaved by 0.5 s. The tracks are shown in Fig. 3. Both the March 30 "racetrack" and the April 3 designs were motivated by the following objectives.

1) To measure 2-D geoacoustic properties and small-scale sediment heterogeneity over large (~30 km) spatial distances and over widely varying mud thicknesses (from ~3 to 12 m). The two east–west ~28 km (March 30) tracks were separated by 1 km—another sediment heterogeneity scale to probe.
2) To collect 2-D and 1-D data at the same site. This was accomplished at both the SWAMI and SC2 sites; the data sets at the same site provide an opportunity for intercomparison of 2-D geoacoustic results with those from the 1-D data. The latter are expected to contain higher geoacoustic information content and lower uncertainties due to a wider angular range.
3) To conduct 2-D measurements over sites/tracks planned by other researchers for intercomparison. For example, numerous long-range acoustic propagation experiments were conducted by other researchers along the x-shaped pattern of cores (magenta points) in the central area of the experiment box (see Fig. 3). The crossing point of the "x" is near the thickest point of the mud layer, i.e., ~12 m. The April 3 lines (blue) traverse along the same bearings as the cores and other researchers' experiments; designed to coincide with the propagation tracks and provide higher lateral/vertical resolution geoacoustic properties than possible from long-range propagation data.
4) To examine 2-D data repeatability by conducting the same experiment along the same track multiple times. This was partially accomplished on March 30 (red line); mechanical issues prevented the planned acquisition start at the western end of the northern leg. Instead, acquisition began at ~70.65° W on the northern leg, transiting east. Shortly after the first full racetrack was completed, another research vessel occupied the track, which necessitated an unplanned turn to the south-east (see Fig. 3). This left a short, ~900 m, track section starting at ~70.65° W from which raw data and inferred geoacoustic properties can be compared along the same track. The April 3 track has multiple passes near the center of the X-coring pattern.
5) To examine azimuthal variability. The multiple crossing points along the March 30 and April 3 tracks at the SWAMI site were intended to permit inter-comparison of the 2-D data along different bearings.

Marine mammal activity in the area on April 3 limited transmissions, which resulted in no data collected along the southwestern leg of the coring pattern.

In addition to the towed array receiver on April 3, a short bottom-moored hydrophone string was deployed near the former position of Scripps 2 array along the south-eastern leg (cyan circle in Fig. 3). The moored hydrophones collected valuable data from the towed source transmissions including: wide-angle 1-D reflection data, long-range propagation data, and a check on the M18C source tank calibration with the source mounted on the towed array vibration isolation module (VIM) at a depth of 50–60 m.

In the following sections, the experiment hardware and sensors are described in more detail for the two measurement geometries. New experiment geometries, i.e., not described in prior publications, are described in greater detail.

### A. One-Dimensional Reflection Measurement Design

*1) Receivers:* Two different receivers were employed. At the FFI site, the receiver was the FFI horizontal line array. At the three other sites (SWAMI, VC31-2, and SC2), the receiver was a bottom-moored sparse vertical array with two icListen hydrophones, a Loggerhead DSG hydrophone, an RBR temperature and depth recorder (TPod), and an ultra-short-baseline (USB) transponder. The buoyancy member was a 28-in steel sphere. At the SWAMI and VC31-2 sites, the two icListen hydrophones, DSG, RBR, USB, and sphere were nominally 11.5, 15.8, 20, 25, 27, and 31 m above the seabed, respectively. At the SC2 site, the sensors (no DSG) were closer to the seabed at 4, 8, 10, 11, and 15 m to reduce entanglement risk with the towed array. The bottom-moored array was stable on each deployment, with TPod peak-to-peak depth oscillations $\sim \pm 0.05$ m on March 28 and March 31 over a broad period of 9–15 s, and an additional narrow peak period ~17 s on March 28. On April 3, 2017 depth oscillations were $\sim \pm 0.1$ m with a period of 11–15 s. The icListen hydrophone dynamic range is 118 dB, which eliminates the need for gain changes at various ranges (as required in early versions of this experiment geometry [11]). The icListen sampling frequency was 32 kHz, except on March 28, 2017 (VC31-2) when the phone closest to the seabed was 16 kHz. Only data from the upper icListen hydrophone are presented here.

Following deployment, receive array locations were determined using the USB system, which involved crossing over the estimated array location multiple times. The receiver locations from the USB system on March 28, March 31, and April 3, 2017 are 70.7469° W 40.4838° N, 70.5753° W 40.4614° N, and

70.5269° W 40.4401° N, respectively. The radial crossing point over the FFI array was 70.461° W 40.498° N.

*2) Sources:* Two sources were employed. At three sites, the source was an Applied Acoustics AA201 boomer plate [see Fig. 1(b)] mounted on a 1- × 2-m catamaran at a depth of ∼0.4 m. The AA201 plate is 19 cm in diameter and emits a short, ∼0.3 ms, highly repeatable pulse every second with a useable band from a few hundred hertz to a few kilohertz. In the first deployment, the catamaran was deployed from the starboard side crane and towed via the source electrical cable. The initial test showed the catamaran pitching forward under tow. To improve balance, the plate was moved to the aft end of catamaran [see Fig. 1(b)], where the tow point is to the right. Moving the source plate improved the tow characteristics. A second issue was that the catamaran tended to set just inside the ship wake. The concern of bubbles contaminating the source signature prompted shortening the tow/source cable, so that the catamaran moved forward out of the wake. The first reflection experiment on March 28, 2017 (VC31-2 and FFI) was conducted with this setup. One of the remaining problems was that the catamaran was fairly close to the ship hull, ∼5 m, and there was concern for potential contamination by hull reflections. In the subsequent deployment, March 31, 2017 (SWAMI), the tow point was moved to the block under the A-frame and the catamaran was towed by a separate tow line, instead of the source cable. Also, the source power unit was shifted from the lab to the aft hangar, which allowed sufficient source cable for the catamaran to be towed ∼20 m behind the stern where wake bubbles did not appear to affect the result and the catamaran appeared to ride more stably than on the March 28 experiment.

The second source was a GeoSpectrum M18C-6 15.5-cm spherical (omnidirectional; see Appendix A) transducer with a resonance frequency of 12.4 kHz. This source was used at site SC2. Equalized LFM 0.25-s downsweep pulses were broadcast, from 6 to 1 kHz and 6 to 0.5 kHz. The latter pulses were significantly lower in amplitude due to the amplitude equalization.

### B. Two-Dimensional Reflection and Scattering Measurement Design

The towed receiver was the 15.4-m aperture cardioid module from the ONR Five Octave Research Array at Penn State, FORA [12]. From a science standpoint, one of the longer FORA modules (either the 23.6- or 47.2-m aperture) would have been preferable over the cardioid, to measure a wider range of seabed reflection angles (hence increased geoacoustic information content). However, the longer aperture modules do not record individual phones, but rather phone groups and thus were not suitable for individual phone processing needed for the reflection analysis. The cardioid module is oil filled and 88 mm in diameter and contains 234 hydrophones arranged in 78 hydrophone triplets with a 12.5-kHz sampling frequency. Each triplet set consists of three hydrophones on an equilateral triangle with 38.5-mm spacing between the individual phones in a plane perpendicular to the array axis. The 78 triplet sets are spaced along with the array at 0.20 m. The true dynamic range after accounting for electrical and quantization noise is ∼106 dB. In addition to the acoustic sensors, the array has a nonacoustic sensor suite 2.62 m forward of the first hydrophone, which provides heading, pitch, roll, and temperature; a depth sensor is positioned 1.25 m further forward. A depth and temperature sensor is also located 4.48 m aft of the last hydrophone. The receiver was towed at depths of 50–65 m.

The source, a GeoSpectrum M18C-6, was selected because its transmit beampattern is virtually omnidirectional over the frequency range of interest (see Appendix A). A source with a strong beampattern is problematic since the reflection coefficient and scattering cross-section are quite sensitive to the beam pattern and the concomitant required precise 3-D positioning under tow is technically challenging. The challenge with the M18C-6 is to tow a 15.5-cm diameter sphere in a stable fashion. Mounting it under a tow fish was considered; however, reflection and scattering from the towfish structure would have a deleterious effect on the seabed reflection and scattering data quality. Furthermore, the source (towfish) to receiver array separation would vary from ping to ping throughout the experiment evolution. To obviate these issues, the source was mounted directly to the VIM (which seemed a more stable arrangement than mounting on the cable). The mount was implemented with a minimum of hardware to avoid altering the source's omnidirectional characteristics. The mount consisted of a strong nylon mesh wrapped several times around the M18 source and array VIM; heavy-duty cable ties were woven through the mesh fore and aft of the source and tightened around the VIM securing the source and source cable. This necessitated tie-wrapping the source cable to the FORA power/tow cable on each deployment, which was rather labor and time intensive. Nevertheless, the array with the source attached appeared to tow quite stably.

The source was placed on the VIM at the maximum distance from the first hydrophone, i.e., at 30 m, to probe the lowest possible grazing angles (though all postcritical). Since the seabed reflection coefficient varies more rapidly at low than steep grazing angles, these angles provide higher geoacoustic information content. To obtain a wider range of reflection angles than possible from the cardioid array, two additional self-recording hydrophones (DSG) were attached to the tow cable/drogue at 4.75/112 m forward/aft of the source [see Fig. 2(a)]. At a 15-m source–receiver altitude above the seabed, bottom grazing angles from the cardioid module are 33°–45°, and from the two DSGs, 81° and 15°. A second purpose of the DSG closest to the source was to measure quasi-monostatic seabed scattering. On the April 3, 2017 deployment, the DSG attached to the drogue (112 m from the source) was dislodged and lost.

The water column properties were measured with a conductivity–temperate–depth probe immediately before and after the measurements. Consistent with extensive ocean measurements (including moorings) from other researchers [6], the sound-speed profile was nearly isothermal, and changed little during the experiments.

## III. Seabed Reflection Observations (1-D)

There is significant geoacoustic information content in the seabed reflection data both in the time domain and in the frequency domain. Many different methods have been developed to access that information. Broadly, the methods can be divided

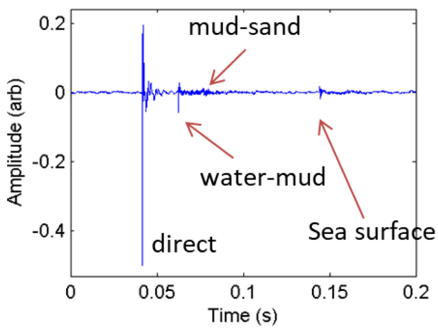


Fig. 4. Raw time series at SWAMI site for a single ping near the closest point of approach.

into "direct," i.e., methods that provide geoacoustic information without Bayesian inversion and "indirect," i.e., methods that require inversion to obtain the geoacoustic properties. In the following, we present the data in the time and frequency domains and the direct geoacoustic information content. Another analysis of the reflection measurements using indirect methods is found in [13].

### A. Time-Domain Analysis

An example of raw time-series data from a single ping is shown in Fig. 4 where the direct path and reflection from the various interfaces can be seen, including the water–mud interface, the sand–mud interface and the sea surface. It is even easier to see the arrivals over multiple pings [see Fig. 5(a)], where the arrivals in slow (UTC) time nearly follow hyperbolae. In particular, the mud–sand horizon is easier to observe than in Fig. 4. A still clearer presentation of the arrivals is shown in Fig. 5(b) where data are mapped in reduced time $t_{\text{red}}$ given by

$$t_{\text{red}}^2 = t_o^2 - \left(\frac{r}{v}\right)^2 \tag{1}$$

where $r$ is the source–receiver offset, $t_o$ is the arrival time at $r = 0$, and $v$ is the reducing velocity. This mapping removes the hyperbolic trend from the data. That is, arrivals in reduced time are approximately independent of source–receiver offset when $v$ is close to the root-mean-square (rms) sound speed. Here, $v =$ 1473 m/s, the water column sound speed. Thus, the direct path and water–mud arrival reduced time are nearly independent of offset.

The salient features to note at this point are the amplitudes of the water–mud and mud–sand arrivals versus offset. The water–mud arrivals are strongest near normal incidence (zero offset) then decay with offset. This behavior is consistent with sediment whose sound speed is less than that of the seawater, where the amplitude decreases from normal incidence to near zero at the angle of intromission [see Fig. 6(a)]. It is not easy to detect if the angle of intromission occurs in the raw data [see Fig. 5(b)], but the evolution of amplitude does show that the sediment sound speed is close to that of water. The mud–sand horizon amplitude shows more or less the opposite behavior, and the reflection amplitude is small near normal incidence and then shows an abrupt increase at about 160 m offset. This abrupt increase is due to the critical angle [see Fig. 6(b)]. Thus, by simple inspection, it is clear that the lower horizon (sand) sound speed is considerably higher than that of the mud.

In seismology, geoacoustic inversion is widely performed from the time-domain response, that is by picking peak amplitudes of individual layer horizons. However, that observable and its forward model require the implicit assumption that the reflection horizon is fully resolved by the pulse, i.e., the reflected field can be properly represented by two homogeneous halfspaces in contact. Given the wide range of seabed scales and processes, this assumption can be invalid in many situations. Moreover, it is not generally possible to determine when the underlying assumption is or is not valid. Yet another disadvantage is the need to determine the layer peak amplitude. While at first blush, it may seem straightforward to pick a peak, factors such as the sampling frequency and the signal-to-noise ratio (SNR) can make peak amplitude estimation subjective.

Instead, the observable chosen for this research is the frequency-domain seabed reflection coefficient. It neither requires any assumptions about the boundaries between layers, nor does the peak amplitude need to be estimated. Most to the point, the geoacoustic properties, sound speed, density, and, especially, attenuation, are generally better estimated in the frequency domain rather than time domain.

### B. Frequency-Domain Analysis

*1) Theory:* We begin with a discussion about the measurement quantity. The simplest quantity that describes acoustic interaction with the seabed is the plane wave pressure reflection coefficient $R_p$ defined as the ratio of the reflected to the incident pressure at a specific angle. However, experimentally, a spectrum of angles is generated, not a single plane wave. Thus, for a given source–receiver offset, the reflected field contains a spectrum of angles, i.e., not just the specular angle at the seabed. This is so because reflection occurs over a finite region at a boundary, the Fresnel zone, that includes a spectrum of incident and reflected angles. Furthermore, the seabed is generally a layered medium and each layer will have distinct specular angle and angular spectrum [see Fig. 1(a)], which shows the specular angle difference at two interfaces. The full physics solution for the reflected field at the receiver is the sum of reflected waves at all angles and is given by the Sommerfeld-Weyl integral, here cast in the angular rather than in the usual wavenumber domain

$$\begin{aligned} p_r\ (\theta_o, f, z_t) \\ = ik \int_0^{\pi/2 - i\infty} R_p\left(\theta, f\right) J_0\left(kr\cos\theta\right) e^{-ikz_t\sin\theta}\cos\theta d\theta \end{aligned} \tag{2}$$

where $\theta$ is grazing angle in the vertical plane, $\theta_o$ is the specular angle $\theta_o = \tan^{-1}(z_t/r)$, $J_0$ is the Bessel function of order 0, $k$ is the wavenumber in the water, $f$ is frequency, and $z_t$ the sum of the source and receiver heights. Note that $R_p$ is completely general and represents any arbitrary plane-layered medium. The integral thus includes reflections from all subbottom interfaces as well as refracted arrivals. It also treats inhomogeneous waves including interface and lateral waves and properly accounts for the Fresnel zone at each interface.

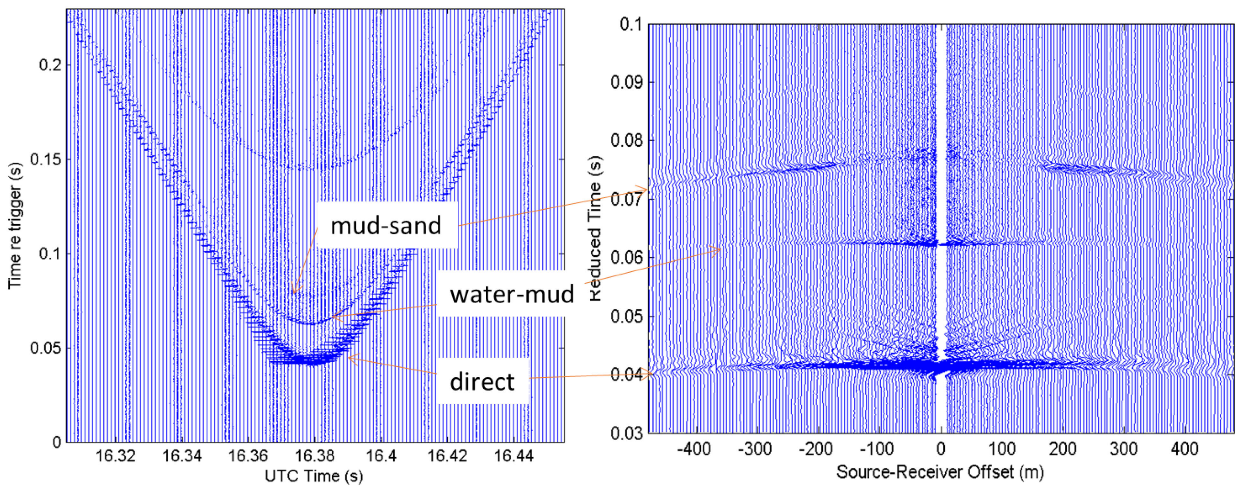


Fig. 5. Stacked raw time series at SWAMI site in (a) linear time and (b) reduced time. Note that between the direct arrival and the reflection from the water–mud interface, there is low-frequency ringing (coda) from the source.

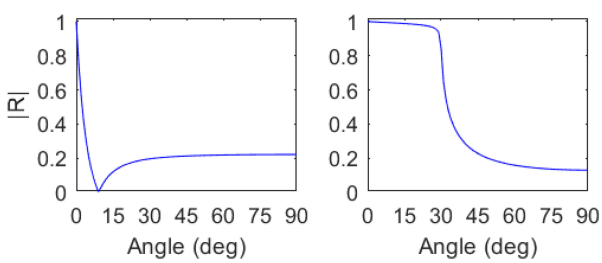


(a) (b)

Fig. 6. Hypothetical reflection coefficients at (a) water–mud and (b) mud–sand boundaries. The mud–sand normal incidence reflection coefficient is smaller than that of the water–mud reflection primarily because the density ratio is smaller.

To form a useful measurement quantity, a spherical reflection coefficient $R_s$ is defined by scaling (2) by a unit source, i.e., $p_d = 1$, times the Green's function along the specular path with $R_p = 1$

$$R_s(\theta_o, f, z_t) = \frac{p_r(\theta_o, f, z_t)}{p_i(\theta_o, f, z_t)} p_i = p_d \frac{e^{ikD}}{ikD} \tag{3}$$

$$R_s(\theta_o, f, z_t) = \frac{ikD}{e^{ikD}} \int_0^{\pi/2 - i\infty} R_p(\theta, f)\ J_0(kr\cos\theta) \times e^{-ikz_t \sin\theta} \cos\theta d\theta \tag{4}$$

where $D = \mathrm{sqrt}(r^2 + z_t^2)$. The independent variable $z_t$ is explicitly shown as a reminder that $R_s$ (unlike $R_p$) depends upon the experiment geometry. It should be noted that since $R_s$ includes a spectrum of angles and arrival paths, energy conservation is not violated for $|R_s|$ greater than unity.

*2) Data Processing:* The data processing follows directly from the theory. Dropping the subscript $o$ for the specular angle for the remainder of this article

$$\left|\hat{R}_s(\theta, f, z_t)\right| = \left|\frac{\hat{p}_r(\theta, f, \tau; z_t)}{\hat{p}_d(\theta_d, f, \tau)}\right| \frac{\gamma_d}{\gamma_r} \tag{5}$$

where $\hat{p}$ is the Fourier transform of the windowed seabed reflected time series, $\gamma$ is the Green's function from source to receiver, which includes spreading and absorption calculated via ray theory, subscripts $d$ and $r$ identify the path type: direct and seabed reflected respectively, $\theta_d$ is the grazing angle at the source for the direct path to the receiver, and $\tau$ is the integration time of the time series. In this work, the integration time starts just before the first seabed reflected return. There are some fine points related to the processing when the source is not omnidirectional that for conciseness are not discussed here but are given in [14]. For the incoherent source, it has been found that averaging the data over proportional bandwidths is a good compromise between high geoacoustic information content and noise. For example, reflection data at the SWAMI and VC31-2 sites were frequency averaged over a 1/7.5 octave bandwidth for transdimensional Bayesian inversion [13].

For one of the reflection experiments, site SC2, the source projected an LFM pulse. To properly perform match filtering, Doppler compensation was applied. The relative motion of the source and receiver imparts both a frequency shift and a pulse duration change. The appropriate Doppler compensation was estimated using a brute force search. Finally, note that the normalization in (5) means that uncertainties in source, receiver, and data acquisition system calibrations play a negligible role. The Green's functions are calculated with the measured sound-speed profiles, which were nearly isothermal and stable throughout these experiments.

When it is possible to synchronize source and receiver clocks, obtaining accurate source–receiver offsets and depth is straightforward using observed-versus-modeled direct path arrival times. When the clocks are not synchronized, as is the case in this experiment, the localization is performed using a linearized Bayesian approach [15].

Processing the direct path time series yields the source amplitude as a function of source angle and frequency. An example of measured source levels at two sites is shown in Fig. 7, where the main features of the beampattern are quite similar, as expected. Some differences are due to differences in the catamaran towing/source plate configuration. The large variation in the beampattern above ~1.5 kHz led to low-quality reflection

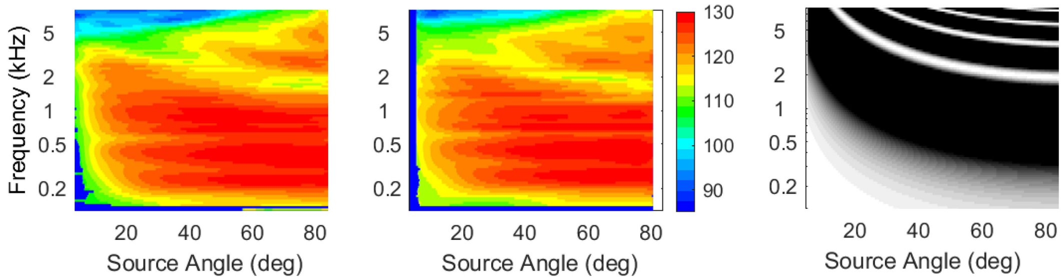


Fig. 7. Source level (dB re 1 uPa$^2$s/Hz @ 1 m) for VC31-2 (left), SWAMI (middle), and Lloyd mirror pattern (right); white is a null. Note the presence of the nulls in the measured source beampattern.

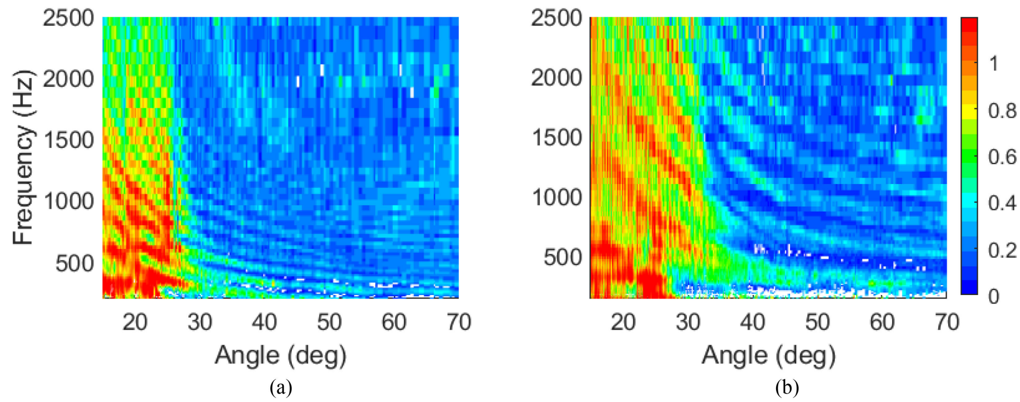


Fig. 8. Reflection coefficient data from (a) thick mud (SWAMI) site where the integration window is 16 m and (b) thin mud (VC31-2) site where the integration window is 14 m. The fringe patterns are from Bragg interference, i.e., the coherent interaction of waves reflected various layer horizons. No angular smoothing has been applied.

data since the seabed reflected path SNR was often poor. This source beampattern feature is due to the shallow source depth. The right-most plot shows the theoretical Lloyd mirror pattern for a source depth of 0.4 m, where the source plate was modeled as a point source. The first null near 2 kHz matches reasonably well with the measurements confirming the cause of the variable beampattern. The second and perhaps the third null are also visible in the measured data.

The final step in the data processing is windowing the seabed reflected path, transforming the data to the frequency domain, and then forming the reflection coefficient. The minimum SNR used in the data processing is 6 dB.

*3) Results for a Long Integration Time:* The integration time $\tau$ provides a means for further increasing the geoacoustic information content of the measured data. For example, consider the time series in Fig. 5(b) from the SWAMI site. To determine the depth dependence of the mud and sand layers, the reflection coefficient is computed from a window that begins just above the water–mud interface and ends a few meters below the upper sand interface(s) at a depth of 16-m subbottom. The resulting reflection coefficients are shown in Fig. 8(a). The most obvious feature is the clear critical angle at $\sim$27°, which can provide an initial estimate of the sandy layer(s) sound speed below the mud.

Another apparent feature is the Bragg interference pattern. Bragg's law gives the condition for constructive interference and can be written for a sediment layer *j*, as $k_j d_j \sin(\theta_j) = n\pi$, where $k$ is the wavenumber, $d$ is layer thickness, $\theta$ is grazing angle, and $n$ is an integer. The pattern of alternating constructive and destructive interference can be seen at all angles below $\sim$1500 Hz. The primary interference comes from waves reflecting off the water–mud and mud–sand interfaces. Other interference patterns from thinner layers are less easy to detect in this image. The Bragg interference contains information about the thickness, sound speed, density, and attenuation of each layer through the following:

1) the evolution of the Bragg lines across angle and frequency;
2) the interference peak-to-trough amplitudes;
3) the decay of the peak-to-trough amplitude as a function of frequency.

The first and last of these data features contain significant information about the frequency dependence of the sound speed and attenuation in each layer, respectively. Some of this geoacoustic information can be accessed through statistical inference, e.g., [13] and some via forward modeling.

The presence and stability of the Bragg interference in the data are an indication that the sediment is plane layered (an important assumption in our theoretical model) and that the processing assumptions are met. Some of the Bragg lines below the critical angle, e.g., $\sim$20°, are smeared across frequency. This has not been observed in reflection data to date, despite data being collected in a wide variety of sedimentary environments in the Mediterranean Sea. The cause of the smearing was found

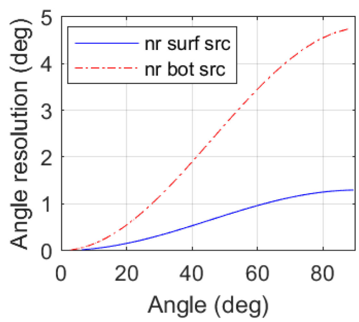


Fig. 9. Angular resolution of the reflection coefficient data from the near surface source (solid) at the SWAMI and VC31-2 sites and the near bottom source at site SC2 (dash dot).

to be due to high-speed layers, greater than roughly 2000 m/s, with relatively low attenuation. These layers are below 16-m subbottom, i.e., below the mud layer and the upper sand layers, and thus do not appear in the time window for the majority of the offsets/angles. However, because of their high sound speed, their arrivals cross over the mud–sand arrivals at far offsets (low angles) and contaminate the reflection processing results at some low angles. Their presence is subtle and not easily seen in the raw data [see Fig. 5(b)]. It may be possible with signal processing to remove or reduce the effect of these arrivals; however, this has not been attempted at this stage.

Processed spherical reflection coefficient data at site VC31-2 are shown in Fig. 8(b). Comparing this with the SWAMI data [see Fig. 8(a)], a number of similarities and differences can be observed. First, both sites exhibit clear Bragg interference patterns, and at both sites, the interference comes from the water–mud and mud–sand boundary reflected waves. Since the VC31-2 mud thickness is ∼3.5 times smaller than that at SWAMI, the peaks and nulls at VC31-2 are spaced further apart by a factor of ∼3.5. Note also the clear critical angle at both sites. The fact that the critical angle is somewhat larger at VC31-2 indicates that there are higher sound speed layers than at the SWAMI site in the upper 14–16 m of the sediment column.

The angular resolution of the reflection coefficient is a function of the ship speed, typically ∼2 m/s, the pulse repetition rate 1 s, and the geometry. The angular resolution is ∼1° at 60° and 0.1° at 15° at the SWAMI and VC31-2 sites [see Fig. 9 (solid line)]. For the M18C source towed at ∼15 m above the bottom to the bottom-moored hydrophone, the angular resolution is larger by about a factor of 4 (dash dot). The factor of 4 comes from the fact that $z_t$ was about a factor of 4 smaller for the M18C source (near the bottom). Angular averaging can be applied for several reasons—it reduces the amount of nonindependent data (i.e., very closely spaced angles do not carry any additional geoacoustic information), it reduces computational cost in statistical inference, and it reduces noise. As can be seen from the pixel size, the data in Fig. 8 have no angle smoothing.

*4) Results for a Short Integration Time (Angle of Intromission):* The angle of intromission is the angle at which the reflection coefficient goes to zero. For marine sediments, it occurs under the conditions that sound speed ratio $(c_2/c_1) < 1$ and density ratio $(\rho_2/\rho_1) > 1$. The angle of intromission $\delta$ was derived by Lord Rayleigh [16] as follows:

$$\cos\delta = \left(1 - (\rho_1 c_1/\rho_2 c_2)^2\right)^{1/2} \left(1 - (\rho_1/\rho_2)^2\right)^{-1/2} \tag{6}$$

where the subscripts 1 and 2 indicate the water and sediment, respectively. It was shown in [17] that by measuring the reflection coefficient versus angle, picking off the angle of intromission $\delta$, and the normal incidence pressure reflection coefficient $\upsilon$, the sediment density and sound speed can unambiguously be obtained from

$$\rho_2 = \rho_1 \left(1 - 4\upsilon/(\cos\delta\,(1+\upsilon))^2\right)^{-1/2} \tag{7}$$

$$c_2 = \rho_1 c_1/\rho_2\ (1+\upsilon)/(1-\upsilon) \tag{8}$$

assuming that the water column $\rho_1$ and $c_1$ are known. The equations can easily be modified if the measurements do not extend to normal incidence.

In principle, detecting the angle of intromission is a powerful way to probe fine-grained (muddy) sediments, which typically have a relative high porosity and are very fragile. Invasive techniques, such as coring and insertion of probes, tend to disrupt the tenuous bonds that form the sediment matrix. Thus, a remote sensing method is of particular value. Despite the benefits, relatively few measurements of the angle of intromission exist. This is mainly because the measurements are challenging.

In practice, measuring the absence of something (in this case, the absence of a reflected wave) is difficult because it requires a high signal to noise ratio, where "noise" not only means ambient and electronic noise, but also "noise" from other acoustic paths. For example, the reflected field from neighboring layers without an angle of intromission renders the angle of intromission "invisible." As a case in point, in this environment, reflection coefficient data from a time window that includes the mud–sand interface, e.g., Fig. 8 cannot be used to determine if an intromission angle exists, since the high reflectivity of the mud–sand interface effectively "fills in" the null in the reflected field. Thus, to observe the intromission angle, all other layers have to be windowed out. Therefore, the reflection time series are windowed around the water–sediment interface [see Fig. 10], spanning here the upper 1.7 m of sediment. Even in these windowed data, there are some low amplitude, but somewhat contaminating, contributions from the source coda, which can be seen between the direct path, at ∼0.04 s, and the water–sediment interface. In the first processing of the data (in 2017), the source coda was not removed. In this present work, the coda is removed by coherent subtraction (see Appendix B).

The processed reflection coefficient data are presented in terms of bottom loss, BL $= -10\,\log_{10}(|\hat{R}_s|^2)$ rather than $|\hat{R}_s|$ because it makes it easier to see the position of the angle of intromission, a peak in bottom loss, rather than a null in |R|. If there is no peak in the bottom loss, then the sediment sound speed in the upper 1.7 m is the same or greater than that of the bottom water. If a peak is visible, then the sediment sound speed must be less than that of the bottom water. There is, in fact, a clear peak in the BL at 8° [see Fig. 11(a)]. This is the angle of intromission. The importance of this result is that this is a direct measurement—not an inversion, which proves beyond doubt the

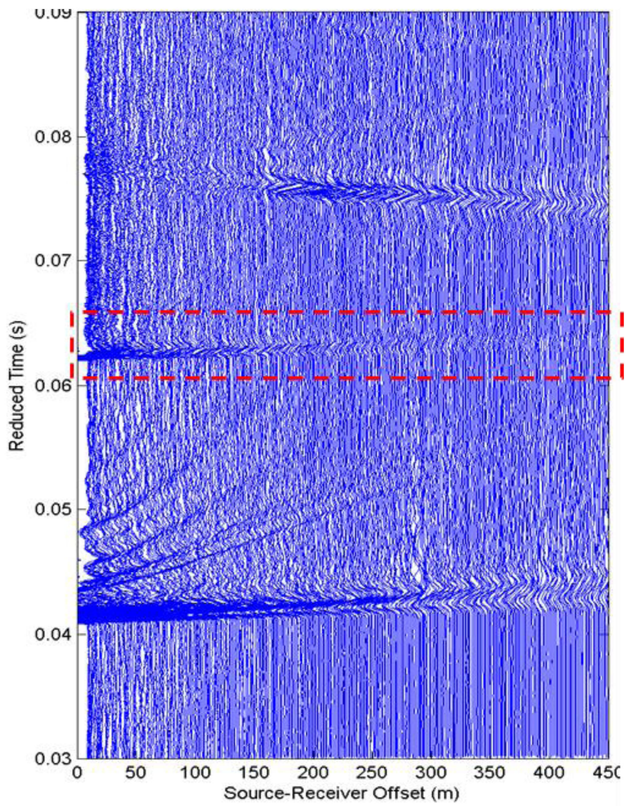


Fig. 10. Time-series data from SWAMI site with window (red dashed lines) around the water–mud interface to obtain the reflection coefficient averaged over the upper 1.7 m.

mud sound speed ratio must be less than unity. Thus, this is a valuable observation for the SBCEX17 community.

*a) Estimation of sound speed and density:* This result can be carried further. From the angle of intromission $\delta = 8°$ and $\upsilon =$ 13.5 dB results in a density ratio of 1.557 and sound speed ratio of 0.9865 unambiguously obtained using (7) and (8). Since the bottom water sound speed and density are known, this leads to a sediment density and sound speed of 1.598 g/cm$^3$ and 1454 m/s, averaged over the upper 1.7 m of sediment. As a sanity check, the directly obtained sound speed and density are used to predict bottom loss using (4), which, as expected, fits the observations quite well [see Fig. 11(b)].

It is of interest to determine the uncertainty of the sound speed and density estimates. The uncertainty depends upon both the measurement uncertainty and the estimation uncertainty. The measurement uncertainty of the angles was calculated via a Bayesian method from path travel time differences [15]. The measurement uncertainty at the angle of intromission 8° is $\pm$0.05°. Taking two standard deviations, 95% probability, the sound speed and density ratio changes from the angle uncertainties 7.9° to 8.1° are [0.9875 0.9869] and [1.5323 1.5333], i.e., very small indeed. The measurement uncertainty of $\upsilon$ related to calibration is essentially zero since the reflection coefficient is self-calibrating, i.e., the measured reflected field is normalized by the measured direct path. There is also a measurement uncertainty of $\upsilon$ related to the source fluctuations, which are a fraction of a decibel.

A more significant contributor is the estimation uncertainty of $\delta$ and $\upsilon$. Somewhat crude uncertainty estimates can be made by varying these two parameters sufficiently to produce a clear mismatch between model and observations. For purposes here, this uncertainty metric will be loosely termed outer bounds. Variations in $\delta$ lead to significant changes in sound speed, but modest changes in density; variations in $\upsilon$ lead to significant changes in density and minor changes in sound speed. Perturbing the angle of intromission from 8° to {7.3° 8.5°} leads to concomitant changes in sound speed ratio of {0.985 0.989}. These can be seen in Fig. 11(d) to poorly match the measured angle of intromission compared to $\delta = 8°$ [see Fig. 11(b)]. In other words, the sound speed ratio outer bounds {0.985 0.989} indicate a rough outer limit on sound speed ratios that can explain the data. In Fig. 11(c), a variation of about $\pm$1 dB in the reflection coefficient produces modeled BL at the extrema of the measured data with a density ratio outer bounds {1.49 1.66}. These estimates provide a measure of uncertainty in sound speed and density from the observations. More rigorous uncertainty estimates will be made in follow-on work using statistical inference methods.

Nevertheless, these sound speed ratio and density ratio results are a significant contribution to the ongoing studies of mud properties at the NEMP. They provide a useful and direct observation to compare with other estimates, which vary from 0.945 to 1.026 over the band 25–1000 Hz (see [6, Fig. 7], which includes only sound speed ratio estimates at/near the water–mud interface). This large variation in sound speed 120 m/s cannot be explained by sound speed dispersion: 1) since the frequency dependence in that figure is erratic, i.e., nonmonotonic; and 2) sound speed dispersion is modest in muds, e.g., [13]. The enormous variation in sound speed also cannot be ascribed to differences in location since: 1) many disparate estimates (including the lowest estimate) were conducted in the central thick-sediment region; and 2) the geologic evidence indicates that "the very consistent lithology of Unit 1 [the upper few meters of mud] results in a very tight range of porosity and grain density values" across the NEMP experiment area [8].

*b) Comparison with a previous angle of intromission estimate:* Previous processing and analysis of the SWAMI angle of intromission data performed without coherent subtraction were first reported in 2017 [18] and shown here in Fig. 16 (blue line). Note that the coda interference leads to bottom loss oscillations, rendering the angle of intromission position somewhat imprecise. For these bottom loss values (without coherent subtraction), the angle of intromission was estimated at 10° in a band centered on 1 kHz; which yielded a sound speed ratio of 0.981$\pm$0.01 as reported in the years 2017 [18] and 2020 [6, Fig. 7].

Coherent subtraction processing (see Appendix B) removes the coda interference, rendering the angle of intromission clear and unambiguous [see Fig. 16 (red line)]. From the coherent subtraction result, the angle of intromission at 1 kHz is 8° with sound speed ratio of 0.9865 and narrower bounds of {0.985 0.989}.

*c) Can attenuation be inferred at the angle of intromission?:* The considerable value of the measuring the angle of intromission has been discussed above. It is of interest to further inquire if there is useful information about the compressional

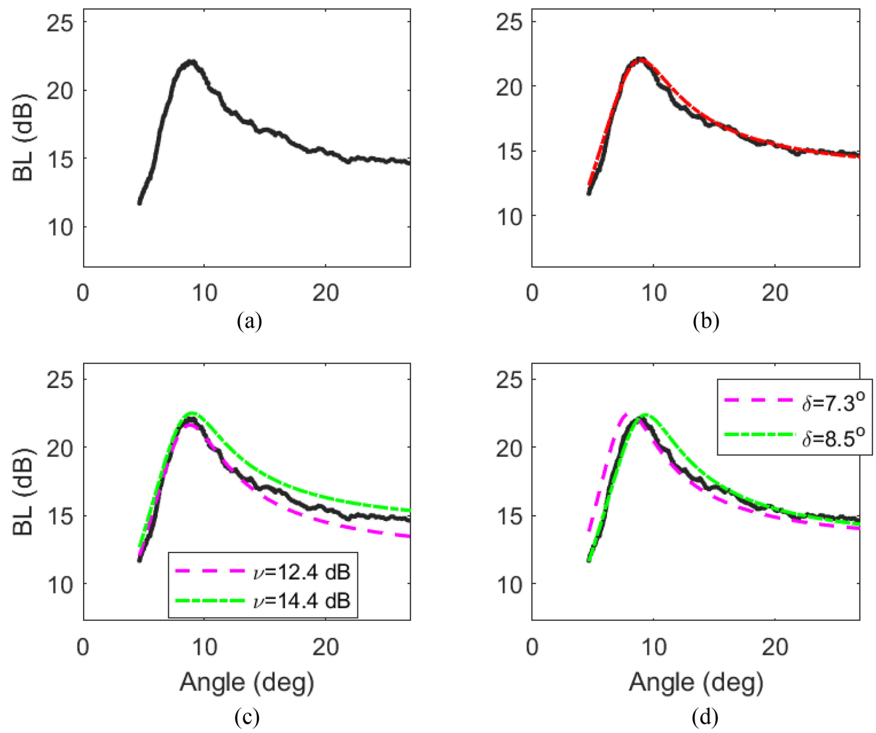


Fig. 11. (a) Measured reflection coefficient data at 1 kHz at the SWAMI site, plotted as bottom loss, i.e., BL. (b) Measured data and model result (red) from the direct geoacoustic estimates. (c)–(d) Comparison of perturbed geoacoustic models provide an indication of geoacoustic uncertainty: varying $\upsilon$ in (c) and $\delta$ in (d) leads to demonstrable misfit with the measured reflection coefficient data near the angle of intromission.

wave attenuation from the reflection coefficient at the angle of intromission $|\hat{R}_s(\delta)|$. For a lossless fluid medium, $|R_p(\delta)| = 0$ and increases monotonically with increasing attenuation. However, there are a number of reasons why the measured $|\hat{R}_s(\delta)| \neq 0$. First, the measurement is not a plane wave, but rather a curved wavefront with a spectrum of angles [see (4)]. Thus, all plane-wave reflection coefficients within the Fresnel zone contribute to the theoretical/measured $R_s$ at the specular angle $\delta$. In other words, even for a lossless fluid, all of the plane-wave reflection coefficients within the Fresnel zone are nonzero, except at $\delta$, therefore $|R_s(\delta)| \neq 0$ except at infinite frequency or infinite source–receiver height. For example, for a lossless fluid mud, the experiment geometry employed in these measurements and a frequency of 1000 Hz, BL$(\delta) \sim 48$ dB, not infinity. Second, even though the shear wave velocity is small in muds, a few tens of meters per second [4], the conversion to shear waves adds a small loss and shifts the angle of intromission to slightly higher angles, of order 0.1°. Third, small-scale microlayering sediment heterogeneities and interface roughness that normally are undetectable may be detectable when the reflection coefficient is near zero. For example, in one study [19], it appeared that the effect dominating $|R_s(\delta)|$ was microlayering, but the effects could not be precisely modeled. Finally, the fact that the attenuation is nonzero in the mud also leads to nonzero $|R_s(\delta)|$. Given the numerous factors affecting $|R_s(\delta)|$, can the compressional wave attenuation be extracted? To do so requires accurately accounting for each of the effects listed. The spherical wave effects can be modeled precisely and the losses due to the unknown shear velocity (profile) could at least be bracketed. However, properly accounting for the effects of (unknown) microlayering, (unknown) sediment heterogeneities and (unknown) interface roughness seem unlikely. Thus, estimation of attenuation from $|R_s(\delta)|$ (or BL$(\delta)$) seems impractical, at least at present. The theoretical curve (red line) in Fig. 11(b) was computed with an attenuation of 0.32 dB/m/kHz, which is an order of magnitude higher than that expected for a muddy sediment. Thus, this does not represent the effects of intrinsic attenuation but rather the small but perceptible effects of microlayering and/or sediment heterogeneities on the reflection coefficient.

## IV. Seabed Reflection and Scattering Observations (2-D)

As with the 1-D data, there is significant geoacoustic information content in the 2-D reflection data both in the time domain and in the frequency domain. An example of the match filtered time-series data in Fig. 12 shows this. The data are from the forwardmost hydrophone at a pulse repetition rate of 1 Hz over a 100-m section of the March 30 upper East–West track. The pulse is a 250-ms 0.5–6-kHz LFM, the Fresnel zone diameter at 3 kHz at the seabed is ~6 m and the distance over ground between pings is ~1.75 m. Thus, two adjacent reflected arrivals share much of the same Fresnel zone. Fast time in the plot (the *y*-axis) is arrival time and contains information about the vertical seabed characteristics. Slow time (*x*-axis) contains information about the lateral seabed characteristics. The first arrival shown in the plot at ~0.72 s is the reflection from the water–sediment (mud) interface, whereas the second arrival at ~0.733 s is from the

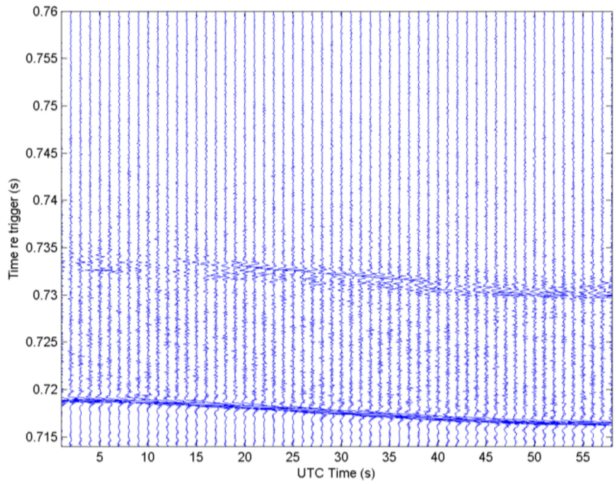


Fig. 12. Match-filtered arrivals for a single channel on the cardioid array March 30, 2017 with a ping rate of 1 Hz and speed over ground ~2 m/s. The earliest arrival, i.e., ~0.72 s, is from the water–mud interface, and the later arrival, i.e., ~0.735 s, is from the mud–sand boundary. The total distance covered on the seabed in this plot is about 100 m. The location is about 70.58° W 40.47°N (on the upper leg of the racetrack; see Fig. 3). The time re trigger is relative to an arbitrary time. The source–receiver offset is ~30 m and grazing angle at the seabed is ~45°. Note that the effects of towed array depth change have not been removed.

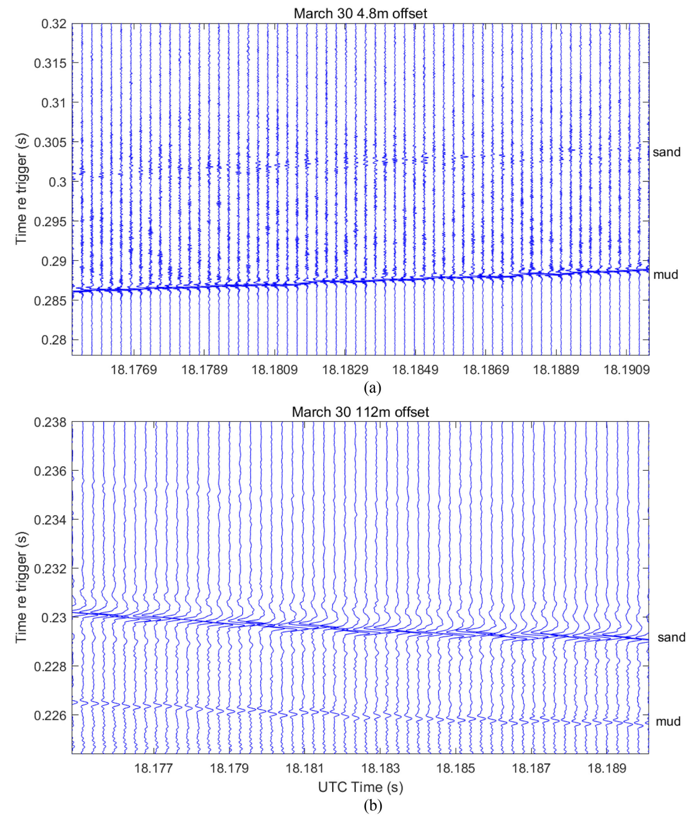


Fig. 13. March 30, 2017 DSG seabed reflection data from source–receiver offset of (a) 4.8 m where the water–mud reflection is at about 0.288 s and the mud–sand interface ~0.3 s and (b) 112 m where the water–mud reflection is at about 0.226 s and the mud–sand interface ~0.23 s. Note that VIM and drogue depth changes have not been removed. The sensors in each plot have a slightly different clock and the time re trigger is arbitrary. The salient point is the difference in the character of the interface reflections and scattering from the sediment volume. The clock on the upper plot was adjusted (40 s) to roughly synchronize the two clocks, but at this stage of the analysis, the interclock time error is still at least a few tenths of a second. The measurement location is ~70.65° W 40.47° N (on the upper leg of the racetrack; see Fig. 3).

mud–sand interface. From the two-way travel time difference, 0.013 s, the sediment thickness is ~12 m (assuming a uniform 1500 m/s and a seabed grazing angle of 45°).

There are three salient features in the data that are similar across the entire 70-km track at this source–receiver separation. First, the mud–sand interface has a high degree of lateral variability at short scales. For example between 20 and 35 s (UTC), the mud–sand interface is comprised of two or three closely spaced layers, but from 11–12 s (UTC), there is little if any evidence of an interface(s). Second, and by contrast, the water–mud interface at 0.72 s is very stable in amplitude and character from ping to ping. Third, above the mud–sand horizon, the mud is nearly devoid of "coherent" layering, but has observable returned/scattered energy. In other words, adjacent signals between 0.72 and 0.733 s have little spatial correlation one with another indicating that the "mud" is not homogeneous. The nature of the sediment heterogeneities that lead to this acoustic response are not known at present.

One question is why these data indicate stronger heterogeneities than in the chirp sonar data interpreted by Goff *et al.* [20], which show relatively clear horizons within the mud and relatively weak heterogeneities. The frequencies here are nearly the same as those in [20]. The most likely reason is that the source in [20] has a relatively narrow beampattern, which delimits the insonified volume, whereas the source is omnidirectional for these data.

The nature of the interface reflections and mud volume scattering is further explored in Fig. 13 at two different angles on the seabed. The top plot is from a small source–receiver offset, i.e., 4.8 m (a grazing angle ~81°), whereas the bottom plot is from a source–receiver offset of 112 m or a grazing angle of 15°. One of the striking differences is that near normal incidence [see Fig. 13(a)] scattering from within muddy sediment volume is high, but the scattering is much smaller at 15° [see Fig. 13(b)]. The higher scattering from the mud volume near normal incidence can also be seen clearly from the fixed-mooring data in Fig. 5(b). Note the "noisy" time series between the mud and the sand boundaries between offsets of about ±50 m; this is clearly not noise from the passing ship, for example, since the "noise" is not observed before the mud layer arrival. One candidate explanation is isotropic heterogeneities; however, these tend to be rare in nature. However, small heterogeneities where the effective radius is much, much smaller than the wavelength, e.g., some shell fragments, can be approximated as isotropic. Theory predicts, however, that the scattered field from small heterogeneities decays more slowly with decreasing angle than the observations. For example, the ratio of the predicted scattered field at 45° to that at normal incidence is only 0.8; the ratio of the scattered field at 15° to that at normal incidence is only 0.6. The scattering observed in the mud layer in Figs. 5(b) and 13 decay with angle much faster than the decay from

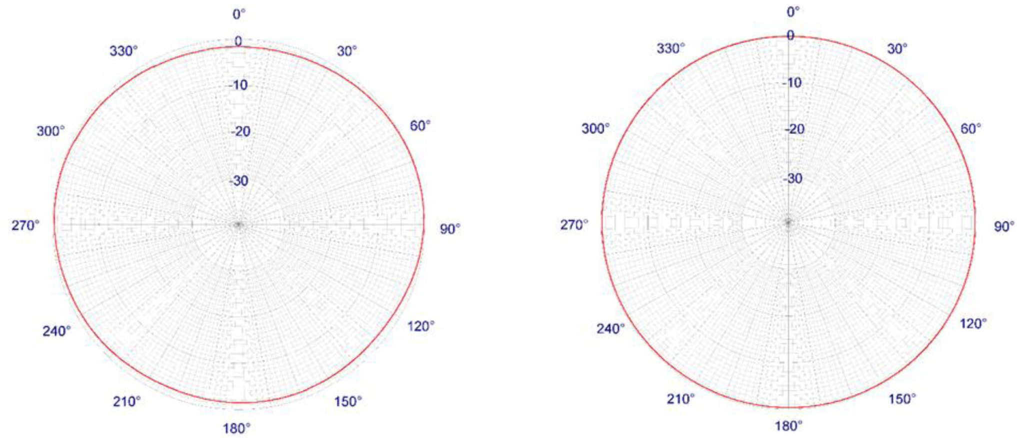


Fig. 14. Beampattern for the M18C source at 6 kHz in (a) horizontal and (b) vertical planes.

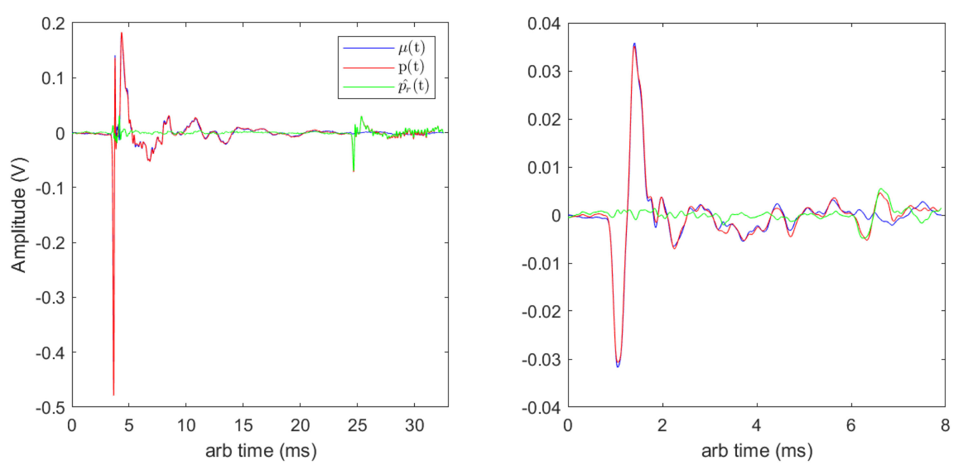


Fig. 15. Results of coherent subtraction, showing the reference (shallow) phone $\mu(t)$ (red); the deep phone $p(t)$ (blue) and the resulting coherent subtraction $\hat{p}_r(t)$ (green) at source–receiver offsets of (a) 10 m and (b) 300 m. The coda is seen in (a) where the broadband direct path arrival (3.7 ms) is followed by a long low-frequency coda, 5–30 ms. In (b), the direct path arrival is at 1 ms.

isotropic heterogeneities. Thus, heterogeneities much smaller than a wavelength do not seem to be a plausible explanation.

The scattering in the mud layer is however consistent with anisotropic heterogeneities, in which the lateral dimension is much larger than the vertical. This is a common characteristic of sediment volume homogeneities inasmuch as marine depositional processes tend to form sediments with larger lateral than vertical scales, sometimes orders of magnitude larger.

The presence of sediment volume heterogeneities within the mud unit is somewhat surprising given that time period in which the mud was deposited, the last ∼11 000 years. During that time, this area has been in an unusually quiescent condition, i.e., a region in which oceanographic conditions permitted the deposition of very fine-grained sediments, essentially the only region along the entire mid-shelf of the U.S. east coast. However, these lenses of silt or sand could have been deposited from large storms. Although the volume heterogeneities are apparent acoustically in the mud unit, the extent of their impact on measuring dispersion is not known at this time. It should be noted that the mud–sand boundary was formed when the area was subaerially exposed; its roughness and complexity is less surprising.

Another aspect to note in Fig. 13 is that the boundary reflection amplitudes are also quite different between near normal and grazing incidence. Near normal incidence, i.e., at 81°, the mud–sand reflection is weak relative to the water–mud reflection. At low grazing angle, i.e., at 15°, the situation is reversed. The primary explanation for this difference is that near normal incidence, the density ratio controls the reflection coefficient at both boundaries—the density ratio is ∼1.55 at the water–mud boundary and in the neighborhood of 1.2 at the mud–sand boundary. By contrast, at low angles, the reflection amplitude at the mud–sand boundary is controlled by the sound speed ratio, which leads to a critical angle. At the water–sediment interface, the reflection amplitude at low angles is controlled by both the density and sound speed ratio, and the proximity of the angle of intromission at ∼8° (where $|\hat{R}_s|$ is very small) means that at 15°, the amplitude will be lower than at normal incidence (see Fig. 11).

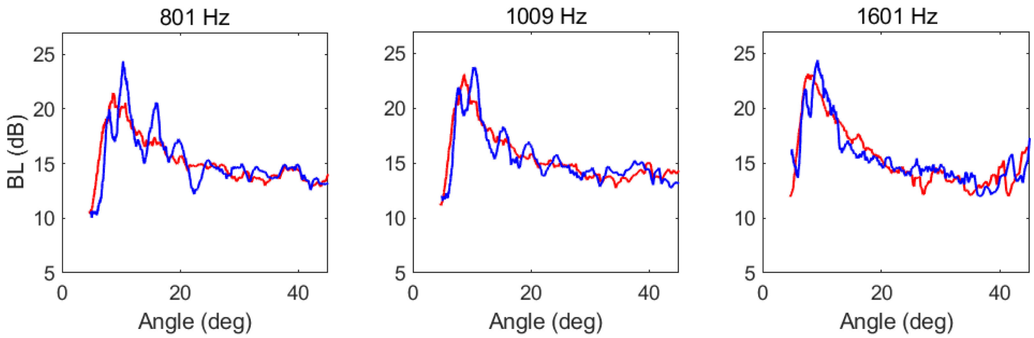


Fig. 16. Bottom loss from the SWAMI site with (red) and without (blue) coherent subtraction. Data are averaged over a 1° window.

It is also clear from the data that the mud–sand reflection is much more stable from ping to ping at low angles than at high angles (see Fig. 13). This is due to several factors, the scattering cross-section is smaller at low angles than at steep angles, the Fresnel zone size is larger at low angles, and at low angles, the critical angle limits the influence of complex sedimentary structure below it.

The above plots provide examples from a few hydrophones. Geoacoustic estimation/inference methods in future research will exploit various observables from the data set. For example, the cardioid aperture and both DSGs will be used to obtain the spherical wave reflection coefficient $|R_s(\theta,f,\tau)|$ along the entire track. From these data, a sequential transdimensional Bayesian approach will infer 2-D (depth and range) geoacoustic properties and their uncertainties. The image source method [21] is a computationally simpler approach to estimate sound speed depth and range dependence and will be applied to the same data. The data will also be used to measure the seabed scattering strength as a function of angle and frequency.

## V. Summary

Measurements were conducted on the NEMP to provide information about the vertical and horizontal geoacoustic variability, in particular that of the fine-grained, or muddy layer. The main findings from the present study are as follows.

1) There exists an angle of intromission. This is direct proof, without modeling or inversion, that the sound speed in the upper 1.7 m of sediment (mud) is less than that of the water column. To the authors' knowledge, these are the first angle of intromission measurements made anywhere on the continental shelf of North America. These data are useful, among other things, to inform reasonable values of sound speed ratio at the NEMP, which currently range 0.945–1.026 from 40 to 1000 Hz, [6, Fig. 7].
2) The angle of intromission permits a precise estimate of the sediment sound speed ratio 0.9865 with outer bounds {0.985 0.989} in the upper 1.7 m.
3) Sediment heterogeneities exist within the mud layer, which are likely anisotropic with a large horizontal to vertical scale.
4) There is clear evidence of a critical angle, both in the time and frequency domains. The time-domain data unequivocally show that the critical angle is associated with the mud–sand boundary. The critical angle at the thin sediment site is ∼5° larger than the thick sediment site.

## Appendix

### A. M18C-6 Beampattern Measurements

M18C-6 source beam pattern measurements were conducted in the anechoic test facility at Penn State. All pulses were 2 ms in length, transmitted at 100 Vrms with a 10% Tukey window.

The source was mounted mid-depth in the tank, ∼2.7 m, separated from the receiving hydrophone by 3.16 m, for a spreading loss of 10 dB. Beam pattern measurements were performed using a single frequency tone and rotating the transducer 360°. The rotational rate ∼3°/s with the transducer triggered at a rate of 10 Hz resulted in an angular resolution of ∼0.3°. Beam patterns were generated at frequencies of 2–15 kHz in 1-kHz steps in both the horizontal and vertical planes. These planes are referenced to the source orientation during the experiment, where the power connector was horizontal [see Fig. 2(b)].

Measurements were performed on two M18C-6 sources with very similar results. The beampatterns were virtually omnidirectional in both planes at below a few kilohertz and had deviations up to a few decibel at the highest frequency of the transmitted pulses during the field experiment, i.e., at 6 kHz.

Only one source was used during the experiment and its calibration is shown here. The 6-kHz beampattern in the horizontal plane is shown in Fig. 14(a) where the beampattern is 0–2 dB lower in directions along the transducer axis, where the axis is defined by the connector. Fig. 14(b) shows that the transducer is virtually omnidirectional in the vertical plane. The lower frequencies all showed less deviation from omnidirectional in the horizontal and vertical than shown here.

### B. Coherent Subtraction Processing

The uniboom source has a low-frequency coda [see Fig. 5(b)]. The coda adds nonnegligible noise within the time window for the angle of intromission measurement (where the reflection coefficient is near zero). To reduce the effects of the coda, coherent subtraction is performed using a reference (shallower) hydrophone.

Coherent subtraction for reducing a discrete scattered arrival from inside the towing platform (an autonomous undersea vehicle) from seabed reflection data was discussed in [22]. This approach was broadly followed here with some differences. The pressure time series after coherent subtraction is defined as

$$\hat{p}_r\left(t\right) = \; p\left(t\right) - aw\left(t\right)\mu\left(t - t'\right) \tag{9}$$

where $p(t)$ is the direct path and water–sediment interface reflected path from the deepest phone (~11.5 m above the seabed), $a$ is the amplitude weighting, $w$ is the window function (7.5% Tukey window), $\mu(t)$ is the reference time series, taken from the shallower phone (~15.5 m above the seabed), and $t'$ is the time shift to align the arrivals.

Several options were considered for defining the amplitude $a$ including using the direct path peak arrival and the rms amplitude of the direct path arrival including the coda. Since the amplitude of the coda (the removal of which is the objective of the processing) is not perfectly proportional to the direct path peak amplitude, the rms value of the direct path arrival including the coda was employed. The amplitude normalization on each ping used a time window delimited by the seabed arrival on the lowest phone.

To improve the accuracy of the time shift $t'$, the data were upsampled at 16 times the recorded sampling frequency 32 kHz. Since the coda is slightly different for each ping, the reference time series $\mu_i(t)$ was taken for every ping $i$ and applied to $p_i(t)$. Results at several ranges are shown in Fig. 15. In Fig. 15(a), the source–receiver separation is 10 m; note that the scaled and time-shifted hydrophones are nearly identical for the direct arrival (3.7 ms) and the coda (5–30 ms) so that the coherent subtraction nearly completely removes the coda. In the early part of the direct arrival, the coherent subtraction is not zero, but this is of no consequence inasmuch as the purpose of the coherent subtraction is to reduce the coda near/at the bottom reflected arrival, i.e., at 26 ms. At this short offset, there is a 22-ms delay between direct and bottom reflected path and the coda has decayed to nearly zero at the seabed reflected arrival time. Thus, coherent subtraction yields only a minor correction. At a further source–receiver offset of 300 m [see Fig. 15(b)], the time delay between the direct and bottom reflected is only 5 ms and the coda is not near zero (e.g., at 5.6 ms) in the neighborhood of the bottom reflected path at 6 ms. At these larger ranges (lower angles), coherent subtraction greatly reduces the coda, and hence improves the SNR of the water–mud reflection coefficient.

Bottom loss without coherent subtraction is shown in Fig. 16 (blue line). Note that since the coda has dominant low-frequency content, the coda interference increases with decreasing frequency. Also, since the coda amplitude is a decaying function, the coda interference increases with decreasing angle (where the time difference between direct and bottom reflected paths is shorter). Finally, the coda interference increases with increasing bottom loss, i.e., at very high bottom loss, the measurement will be dominated by the coda not the seabed reflection. It can be seen that coherent subtraction effectively removes the coda interference effects and thus reveals more accurately the position of the angle of intromission.

## Acknowledgment

The authors would like to thank the Office of Naval Research Ocean Acoustics Program for their support of this research. They would also like to thank Captain Kent Sheasly and his outstanding officers and crew on *R/V Armstrong*, the Seabed Characterization Experiment Chief Scientists David Knobles and Preston Wilson, and all of the colleagues in the SBCEX17 community.

## References

[1] A. D. Pierce, W. L. Siegmann, and E. M. Brown, "Characterization of mud sediments using the frequency dependence pf phase velocity and attenuation of compressional waves," in *Proc. Meetings Acoust.*, vol. 31, no. 1, 2017, Art. no. 070002. [Online] Available: https://asa.scitation.org/doi/abs/10.1121/2.0000891

[2] M. A. Biot, "Generalized theory of acoustic propagation in porous dissipative media," *J. Acoust. Soc. Amer.*, vol. 34, pp. 1254–1264, 1962.

[3] E. L. Hamilton, "Geoacoustic modeling of the seafloor," *J. Acoust. Soc. Amer.*, vol. 68, pp. 1313–1340, 1980.

[4] G. R. Potty and J. H. Miller, "Effect of shear on modal arrival times," *IEEE J. Ocean. Eng.*, vol. 45, no. 1, pp. 103–115, Jan. 2020.

[5] M. D. Richardson, "In-situ shallow Water sediment geoacoustic properties," in *Shallow Water Acoustics*, R. Zhang and J. Zhou, Eds. Beijing, China: China Ocean Press, 1997.

[6] P. Wilson, D. Knobles, and T. Nielsen, "Guest editorialan overview of the Seabed Characterization Experiment," *IEEE J. Ocean. Eng.*, vol. 45, no. 1, pp. 1–13, Jan. 2020.

[7] R. T. Bachman, "Acoustic and physical property relationships in marine sediment," *J. Acoust. Soc. Amer.*, vol. 78, pp. 616–621, 1985.

[8] J. D. Chaytor *et al.*, "Measurements of geologic characteristics and geophysical properties of sediments from the New England Mud Patch," *IEEE J. Ocean Eng.*, vol. 45, pp. 69–91, Jan. 2020.

[9] A.-L. Lapinski and D. M. F. Chapman, "The effects of ignored seabed variability in geoacoustic inversion," *J. Acoust. Soc. Amer.*, vol. 117, pp. 3524–3538, 2005.

[10] M. G. Morley, S. E. Dosso, and N. R. Chapman, "Parameter estimate biases in geoacoustic inversion from neglected range dependence," *IEEE J. Ocean. Eng.*, vol. 33, no. 3, pp. 255–265, Jul. 2008.

[11] C. W. Hollandand J. Osler, "High resolution geoacoustic inversion in shallow water: A joint time and frequency domain technique," *J. Acoust. Soc. Amer.*, vol. 107, pp. 1263–1279, 2000.

[12] K. M. Becker and J. Preston, "The ONR Five Octave Research Array (FORA) at Penn State," in *Proc. IEEE OCEANS Conf.*, 2003, pp. 2607–2610.

[13] J. Belcourt, C. W. Holland, S. E. Dosso, and J. Dettmer, "Depth-dependent geoacoustic estimates with dispersion from the New England Mud Patch via reflection coefficient inversion," *IEEE J. Ocean. Eng.*, vol. 45, no. 1, pp. 69–91, Jan. 2020.

[14] C. W. Holland, "Seabed reflection measurement uncertainty," *J. Acoust. Soc. Amer.*, vol. 114, pp. 1861–1873, 2003.

[15] J. Belcourt, S. E. Dosso, C. W. Holland, and J. Dettmer, "Linearized Bayesian inversion for experiment geometry at the New England Mud Patch," *IEEE J. Ocean. Eng.*, vol. 45, no. 1, pp. 60–68, Jan. 2020.

[16] J. W. S. B. Rayleigh, *The Theory of Sound*, 2nd ed., 1896, vol II. New York, NY, USA: Dover, 1945, p. 81.

[17] C. W. Holland, "Geoacoustic inversion for fine-grained sediments," *J. Acoust. Soc. Amer.*, vol. 111, pp. 1560–1564, 2002.

[18] C. W. Holland, C. M. Smith, J. Belcourt, and S. E. Dosso, "Geoacoustic inferences from seabed reflection measurements on the New England Mud Patch," *J. Acoust. Soc. Amer.*, vol. 142, no. 4, pp. 2590–2590, 2017.

[19] C. W. Holland, "Coupled scattering and reflection measurements in shallow water," *IEEE J. Ocean Eng.*, vol. 27, no. 3, pp. 454–470, Jul. 2002.

[20] J. Goff, J. D. Chaytor, A. H. Reed, G. Gawarkiewicz, P. S. Wilson, and D. P. Knobles, "Stratigraphic analysis of a sediment pond within the New England mud patch: New constraints from high-resolution chirp acoustic reflection data," *Mar. Geol.*, vol. 412, pp. 81–94, 2018.

[21] S. Pinson, L. Guillon, and C. Holland, "The image-source method: A tool for geoacoustic inversion," *Near Surf. Geophys.*, vol. 18, pp. 39–48, 2020.

[22] C. W. Holland, P. L. Nielsen, J. Dettmer, and S. E. Dosso, "Resolving meso-scale seabed variability using reflection measurements from an autonomous underwater vehicle," *J. Acoust. Soc. Amer.*, vol. 131, pp. 1066–1078, 2012.

**Charles W. Holland** received the B.S. degree in engineering from University of Hartford, West Hartford, CT, USA, in 1983, and the M.S. and Ph.D. degrees in acoustics from Pennsylvania State University, State College, PA, USA, in 1985 and 1991, respectively. His Ph.D. dissertation addressed acoustic propagation through and interface waves in poro-viscoelastic marine sediments.

From 1985 to 1996, he conducted research in ocean and sediment acoustics at Planning Systems, Inc., Reston, VA, USA. In 1996, he joined the NATO Undersea Research Centre, La Spezia, Italy, where he developed seabed reflection and scattering measurement and geoacoustic estimation techniques. In 2001, he joined the Applied Research Laboratory, Pennsylvania State University, and in 2020, he joined Portland State University, Williamsburg, VA, USA, where he continues his research in both theoretical and experimental aspects of ocean waveguide and seafloor acoustics.

Dr. Holland is a Fellow of the Acoustical Society of America. His contributions to this work included concept generation, experiment design, data processing, theoretical analysis, and manuscript preparation and editing.

**Chad M. Smith** (Member, IEEE) received the B.S. degree in electrical engineering technology from the Pennsylvania College of Technology, Williamsport, PA, USA and the M.S. and Ph.D. degrees in acoustics from Pennsylvania State University, State College, PA, USA.

He is currently an Assistant Research Professor at Penn State Applied Research Laboratory, where he has held a research appointment since 2010. Before his time at Penn State, he specialized in the research and development of high-power transducer control and data acquisition systems for marine applications at QorTek, Inc., Williamsport, PA, USA. His primary research interests include characterization of underwater and atmospheric propagation, sonar reverberation, signal coherence, and signal processing. His career is characterized by a combination of basic and applied research with an emphasis on marine and terrestrial experimentation and systems development. During his career, he has conducted research on a broad range of topics including rapid environmental assessment, antisubmarine warfare, sonar classification, synthetic aperture sonar imaging, geoacoustic inversion, bioacoustics monitoring, atmospheric infrasound monitoring, and infrasound transducer development.

Dr. Smith is a member of the Acoustical Society of America and the IEEE Oceanic Engineering Society. His contributions to this work included data collection, processing, and assembly and manuscript editing.

**Zackary Lowe**, photograph and biography not available at the time of publication.

His contributions to this work included data collection, processing, and assembly and manuscript preparation.

**Jim Dorminy**, photograph and biography not available at the time of publication.

His contributions to this work included data collection and assembly.

# ATTACHMENT 3

# Seabed Structure Inferences From TREX13 Reflection Measurements

Charles W. Holland, Samuel Pinson, Chad M. Smith, *Member, IEEE*, Paul C. Hines, Derek R. Olson, Stan E. Dosso, and Jan Dettmer

***Abstract*—Seabed reflection measurements can be used to infer highly detailed properties of marine sediments. The information content is largely contained in the interference pattern in frequency-angle arising from wave constructive and destructive interference in a plane layer. Wide-angle reflection measurements at a ridge crest and a swale site off the coast of Panama City, FL, USA, instead show interference patterns that are highly perturbed. Interface roughness was hypothesized to be the cause of the perturbations. This hypothesis is examined using numerical simulations. Measured data and simulations at the swale site show broadband peaks and troughs due to focusing/defocusing effects from boundary curvature which perturbs the interference pattern. While the hypothesis roughness is likely correct at the swale site, the roughness statistics are not known sufficiently to validate the hypothesis. At the crest site including roughness did not lead to strong similarities with the data. Interference pattern perturbations at both sites eliminated the possibility of estimating sediment parameters from inversion of broadband wide-angle data. Instead, sediment properties were estimated by inspection and forward modeling. The estimates reasonably agree with geoacoustic properties estimated from normal incidence measurements in the swale and indicate similar sound speeds and densities on two ridges ∼6 km apart.**

***Index Terms*—Geoacoustic properties, roughness, seabed reflection.**

## I. Introduction

MIDFREQUENCY 1–10-kHz reverberation in littoral regions is often controlled by seabed mechanisms. For example, in isospeed or downward refracting conditions, seabed properties often dominate boundary reflection and scattering, which are both important factors for reverberation. Seabed reflection is often approximated (modeled) using flat boundaries and bulk sediment properties, i.e., smoothly varying properties within a sediment layer, and ignoring heterogeneities or fluctuations, e.g., [1]. Seabed scattering, on the other hand, is a function of both of the smoothly varying sediment properties and small-scale inhomogeneities, e.g., [2].

Manuscript received February 29, 2016; revised September 6, 2016; accepted January 20, 2017. Date of publication February 22, 2017; date of current version April 12, 2017.

**Guest Editors: B. T. Hefner and D. Tang.**

C. W. Holland, C. M. Smith, and D. R. Olson are with the Applied Research Laboratory, Pennsylvania State University, State College, PA 16801 USA (e-mail: cwh10@psu.edu).

S. Pinson is with the Laboratorio de Vibracao e Acustica, Universidade Federal de Santa Caterina, Florianopolis 88040-900, Brazil.

P. C. Hines is with Dalhousie University, Halifax, NS B3H 4R2 Canada.

S. E. Dosso is with the School of Earth and Ocean Sciences, University of Victoria, Victoria, BC V8P 5C2 Canada.

J. Dettmer is with the Department of Geoscience, University of Calgary, AB, T2N 1N4, Canada

Digital Object Identifier 10.1109/JOE.2017.2658418

The bulk sediment properties of interest are the compressional wave speed and attenuation and density as a function of depth and frequency. Measurement of even these properties (under the fluid sediment approximation) is challenging. There are a number of approaches for measuring these properties including direct (e.g., coring) and remote sensing or geoacoustic inversion approaches (e.g., sediment property inference from acoustic measurements), each of which has advantages and disadvantages.

The observational approach here employs measurements of broadband wide-angle seabed reflection. The advantages of this approach are:

1) high resolution vertically, 0.1 m and laterally, $O(10^1)$m;
2) relatively small uncertainties from the space/time-varying oceanography and biologics due to short path lengths;
3) low source levels are possible;
4) the data are expected to be highly informative for seabed geoacoustic properties, especially sound speed, density, and attenuation dependencies on depth and frequency (e.g., see [3]).

Wide-angle reflection measurements can be conducted with a moving source and receiver to probe lateral variability (e.g., [4]); however in this experiment, the receiver was fixed. To probe lateral variability, broadband normal incidence reflection data were also measured. These data have significantly lower information content than the wide-angle data, and lead to numerous parameter ambiguities in estimating sediment properties. Nevertheless, these data can be useful for developing a broad understanding of the sediment spatial variability.

The high information content of the wide-angle reflection data is primarily contained in the interference pattern across frequency and angle caused by a layered medium. The interference pattern is due to the classical quarter-wavelength and half-wavelength resonances in a given layer that lead to nulls and peaks, respectively, in the reflection coefficient across frequency and angle. The interference pattern has always been observed in dozens of our previous wide-angle measurements. Its presence has opened the door to estimating: layer thicknesses [5], the number of layers[1] [6], density gradients [7], sound speed, and attenuation dispersion [3] (i.e., their frequency dependence

[1]In most geoacoustic inversion approaches, the number of layers must be chosen by the researcher before performing the inversion, but broadband wide-angle reflection data contain sufficient information through the interference pattern to permit number of layers itself to be a parameter determined by the data; see [6].

which is typically difficult to obtain), and spatial variability (e.g., [4] and [8]).

All of these previous measurements were conducted on the mid to outer shelf, in water depths 80–180 m. This experiment was sited in a water depth of 20 m off Panama City, FL, USA, as part of the 2013 Target and Reverberation Experiment (TREX13). In this inner shelf region, there is significantly more wind, wave, and current energy at the benthic boundary. This, coupled with proximity to varied sediment fabrics, e.g., estuarine and marine, leads to much higher geoacoustic spatial variability (including larger interface roughness and stronger sediment volume heterogeneities) than on mid to outer shelf regions. Thus, our past assumption of flat interfaces and no significant sediment heterogeneities turned out to be inappropriate for this environment.

The paper is organized as follows. In Section II, the design of the reflection experiment is discussed. Wide-angle data processing is described and the reflection data are presented in Section III. Modeling and inspection of the data indicate that the interference pattern has been perturbed, which prevents statistical inference using a plane-layered model. Instead, geoacoustic properties are estimated from the wide-angle data using theory and forward modeling. One cause of the perturbations is hypothesized to be layer roughness and this hypothesis is explored by numerical simulations at both the ridge crest site and the swale site. In Section IV, normal incidence seabed reflection data are presented and analyzed near the swale site and the estimated geoacoustic properties are compared with those estimated from wide-angle data. Section V presents the conclusions and summary.

## II. Measurement Design

The goal of the seabed reflection measurements was to provide bulk sediment properties in each sediment layer. This is required for 1) modeling scattering, which requires an understanding of the background medium (scattering data generally contain insufficient information content to obtain both the background and the fluctuating components); and 2) modeling propagation.

One of the experimental challenges of wide-angle measurements is multipath separation, in particular separation of the direct path, the seabed reflected path, and sea surface reflected path. At the TREX13 location, the 20-m water depth and the inability to employ a source very near the sea surface (the usual geometry) necessitated a particularly precise design of the geometry and waveforms.

The experiment design is shown in Fig. 1, where a small, $\sim 1 \times 2$ m, catamaran was deployed about 20 m aft of Canadian Forces Auxiliary Vessel *Quest*. The source was suspended below the catamaran 7–10 m, depending on the run. To limit the vertical and horizontal displacement of the source due to drag, a line was connected from the tow cable to the suspension line just above a 10-kg weight (not shown) several meters below the catamaran. The source was an ITC-1007 spherical transducer which transmitted an equalized 0.25-s linear frequency modulated (LFM) down sweep from 12 to 1.4 kHz at 

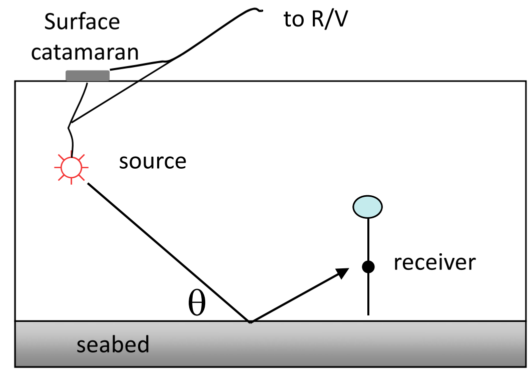


Fig. 1. Experiment design. The water depth is about 20 m; source and receiver depths were about 7 and 16 m, respectively. A reference hydrophone (not shown) 2 m above the source served to monitor source transmissions as well as measuring normal incidence reflections from the seabed.

160 dB re 1 $\mu$Pa @ 1 m and a repetition rate of 0.5 s. A depth sensor and reference hydrophone were placed about 1 and 2 m above the source, respectively. The reference hydrophone was employed both to monitor the source transmission and to measure normal incidence reflection.

The receiver consisted of three self-recording hydrophones placed along a vertical mooring line 7.5 m in length with a 0.25-m radius float providing buoyancy at the top. Signals from two hydrophones were slightly contaminated by scattering from corners and edges of the small potted rectangular electronics boxes which were within $\sim$0.1 m of the hydrophone. The third hydrophone (icListen HF) deployed at $\sim$16-m depth exhibited a clean signal and was used in this analysis. The receiver dynamic range was 120 dB and the sampling rate 64 kHz.

The ship transited as slowly as practical, given the sea conditions, while maintaining navigation along a straight line. Typically the speed was about 1.5 m/s. To achieve the widest possible angular coverage, the tracks were planned such that the catamaran transited directly over the receivers. Despite difficulties attendant to low-speed navigation and position uncertainties of the source and receiver, the minimum horizontal distance between source and receiver was typically about 10 m (estimated by geometry reconstruction discussed later). The very close proximity of the ship to the receiver required low ship radiated noise levels, which was achieved. There were also concerns in the planning stage about reflections from the ship hull, which were indeed observed in the measured data when approaching the receiver. However, hull reflections were sufficiently separated in time from the seabed arrivals that they did not affect the data processing.

Wide-angle seabed reflection measurements were conducted at two locations, see Fig. 2. The swale site is located between two small ridges near the end of the ridge-swale topography [9] and the ebb tide delta (bathymetric bulge) seen in the lower right-hand corner of Fig. 2. The sediments there are characterized by a poorly sorted conglomeration of sand and shells with a significant fine fraction [10]. In this area, it was difficult to map the mid-sand-sheet reflector beneath the poorly sorted sediment from the seismic data, but it was speculated to be about a meter or less below the seafloor [10]. The swale site is positioned slightly

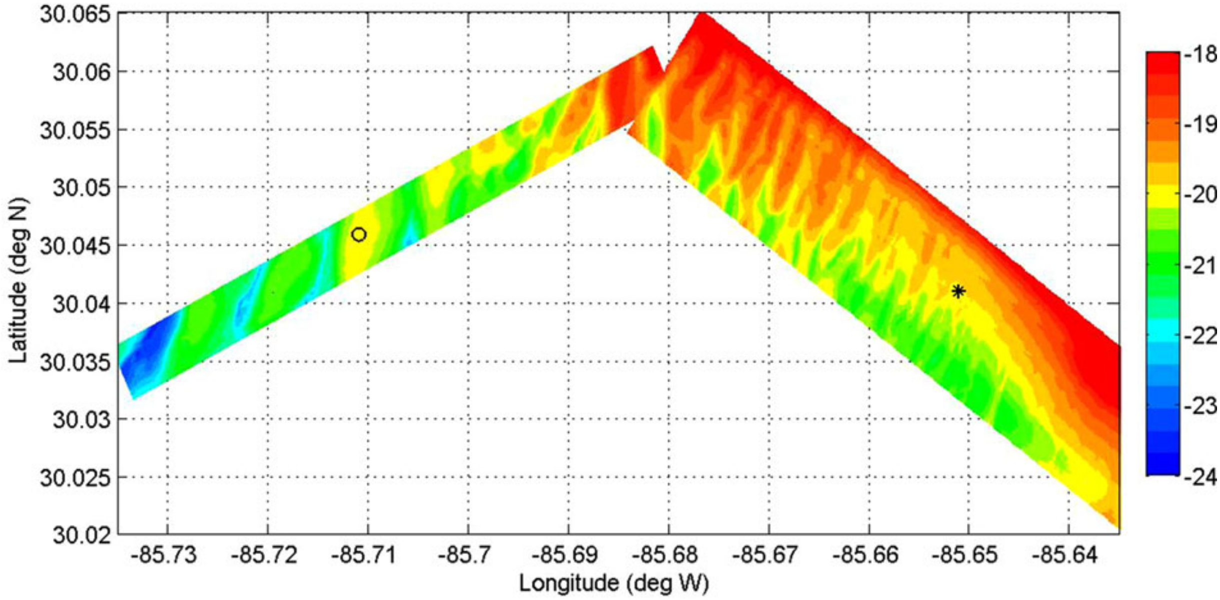


Fig. 2. Bathymetry (in meters) and location of swale (∗) and crest (○) reflection sites.

north Northeast of the main reverberation track center line. The second location, the crest site, was centered on a ridge crest along a different bearing. The measurements were conducted on May 3 (crest site) and May 5 (swale site) 2013; the sound-speed profiles at both sites were nearly isovelocity.

## III. Wide-Angle Reflection

### A. Data Processing

The quantity of interest is the seabed spherical wave reflection coefficient. It is defined as the ratio of the reflected acoustic pressure at a given source–receiver position, scaled by Green's function for the specular path as if the seabed were a perfectly reflecting half-space (for details, see [11]). Two differences from the processing in [11] and this experiment are: 1) the necessity to account for the Doppler shift (prior measurements either used an impulsive source, or the source and receivers were moving in tandem); and 2) the necessity to estimate source–receiver offsets using relative travel time between the direct, bottom, and sea surface paths. Both of these are described below.

*1) Doppler Estimation:* The use of a broadband LFM signal from a moving source and fixed receiver necessitated Doppler compensation. The Doppler corrections are important for temporally separating the direct, bottom, and surface paths so that the reflection coefficient can be formed by scaled ratio of the bottom and direct path total energies. In cases where there is a sufficiently large temporal separation of the paths, e.g., high angles, there is no difference between Doppler-corrected and no Doppler-corrected reflection coefficients. That is, Doppler effects do not change the total energy.

While there was a global positioning system (GPS) unit on the catamaran, neither the source position (beneath the catamaran), nor the receiver position were precisely known. Doppler estimation is often performed using a search algorithm resulting in an ambiguity function, from which the most likely Doppler speed is drawn. Pinson [12] developed a simpler method using the phase of the Doppler cross-power spectrum that performed as well or better than the search method on these datasets. Examples of the results are shown in Fig. 3, where the "raw" curve (blue line) represents match-filtering with the transmitted pulse. The curve labeled "Dop compen" (red line) represents match-filtering with Doppler compensation applied to the transmitted pulse. The first arrival is the direct path. Note that in the raw match-filtered data, the low frequencies arrive first/last on the incoming/outgoing legs. The Doppler processing properly compensates for the relative motion, shortening the width and increasing the peak of the direct path arrival. Near the closest point of approach (CPA), the effect of the Doppler shift is small, as expected. The estimated relative speeds from the Doppler processing agrees closely with the measured speed from a GPS unit mounted on the catamaran, which gives confidence in the method (see Appendix 1, Fig. 18).

Doppler estimation was performed on the direct path only and the Doppler compensation was applied to the entire signal. While the Doppler shift for the bottom reflected path will differ from that of the direct path, the difference is expected to be very small because the receiver is only a few meters above the seabed, i.e., the path difference between the direct and bottom paths are relatively small. The effect of ignoring the slightly different Doppler is that the match-filtered data for the bottom reflected path will have a slightly lower and broader peak than for perfect compensation. Since the wide-angle reflection processing is based on waveform energy, not peak amplitude (i.e., the time series are integrated across separate time windows containing the direct and bottom reflected paths), the slight mismatch will not lead to errors in the magnitude of the reflection coefficient. There will be a slight shift in the spectrum, but this is expected to be negligible for the 50-Hz processing bandwidth.

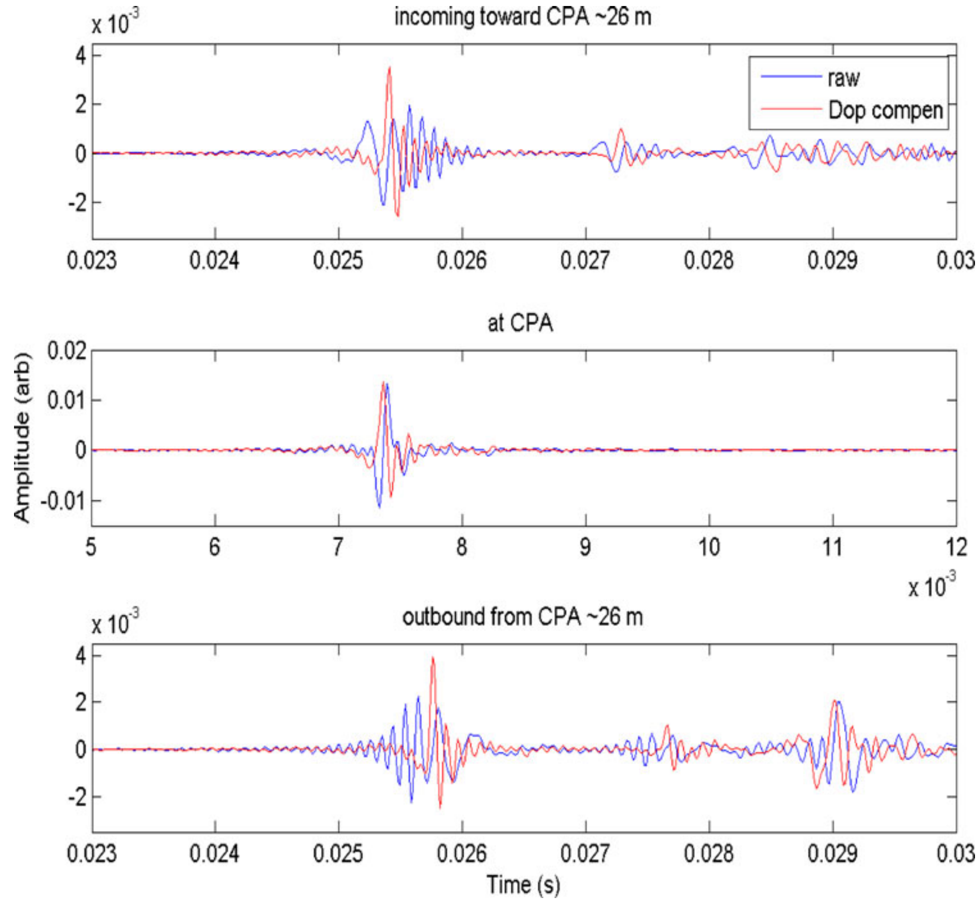


Fig. 3. Example of raw data using the transmitted waveform as the replica (blue) and the Doppler compensated pulse (red) at three source-receiver offsets: 26 m incoming, near the CPA, and 26 m outbound.

The Doppler corrected time series data, Fig. 4, show the direct path (first arrival), followed by the seabed reflected arrival, followed by the sea surface arrival (expressions of individual waves can be observed). Since the clock drift on the self-recording receiver was unknown, the transmitted source pulse arrival time is not known at this stage of the analysis. Even relative time (i.e., picking an arbitrary transmit time) was useful since in the initial analysis the slope of the incoming and outgoing direct path arrivals differed by a factor of 2. For the nearly constant ship speed, the slopes should be nearly identical. The slope differences meant that there was a 16.4-Hz error in the nominal sampling frequency of the transmitted pulse (which was later verified). In this plot, the correct sampling frequency has been used.

To determine arrival times, or equivalently the source–receiver offsets, an inversion method was employed using travel time differences between the direct, bottom, and sea surface paths (see Appendix 1).

*2) Reflection Data Processing:* Given source–receiver horizontal offsets or ranges *r*, the data can be examined in reduced time, $\tau = (t^2 - (r/c_{\rm red})^2)^{1/2}$ where $t$ is time, $c_{\rm red}$ is an arbitrary reducing velocity, here $c_{\rm red} = c_w = 1524$ m/s where $c_w$ is the seawater sound speed. This essentially removes the hyperbolae relating range offset with arrival time, flattening out the arrival times, see Fig. 5. The first arrival in Fig. 5 is the direct path; the second arrival is the seabed reflected path. Each trace represents a different seabed angle and thus each angle samples a slightly different portion of the seabed. From a ray point of view, the specularly reflected ray strikes the seabed 3.5/14 m from the receiver at the steepest/shallowest angle. The spatial dimension of the insonified region around each seabed specular point is defined by the Fresnel zone, which is an ellipse. The major axis of the ellipse is along the line connecting source and receiver projected on the seabed (termed “in-plane”), and the minor axis is perpendicular. For example at 2 kHz, the in-plane Fresnel radius is 11 m at the lowest angle and 1.5 m at the steepest angle. Given the high pulse repetition rate and low source speed, substantial overlap of the insonified area exists from angle to angle along the track. The total in-plane region of seabed that is probed in this geometry, including the Fresnel zone, is about 25 m, that is, 25 m on the incoming (negative ranges) and 25 m on the outgoing (positive ranges) tracks.

On the incoming track the multibeam data show a very slightly sloping seabed (less than 0.1°). The nearly flat nature of the seabed is borne out by inspection of the seabed reflected path (negative ranges) in Fig. 5, which is essentially constant in time. Note that on the outgoing leg, at $\sim$58 m, arrival times indicate that the bathymetry has a slight change of slope.

The third arrival in Fig. 5 is the sea surface reflected path. The strong arrival time variation associated with this path is due to individual sea surface waves. The sea state during the

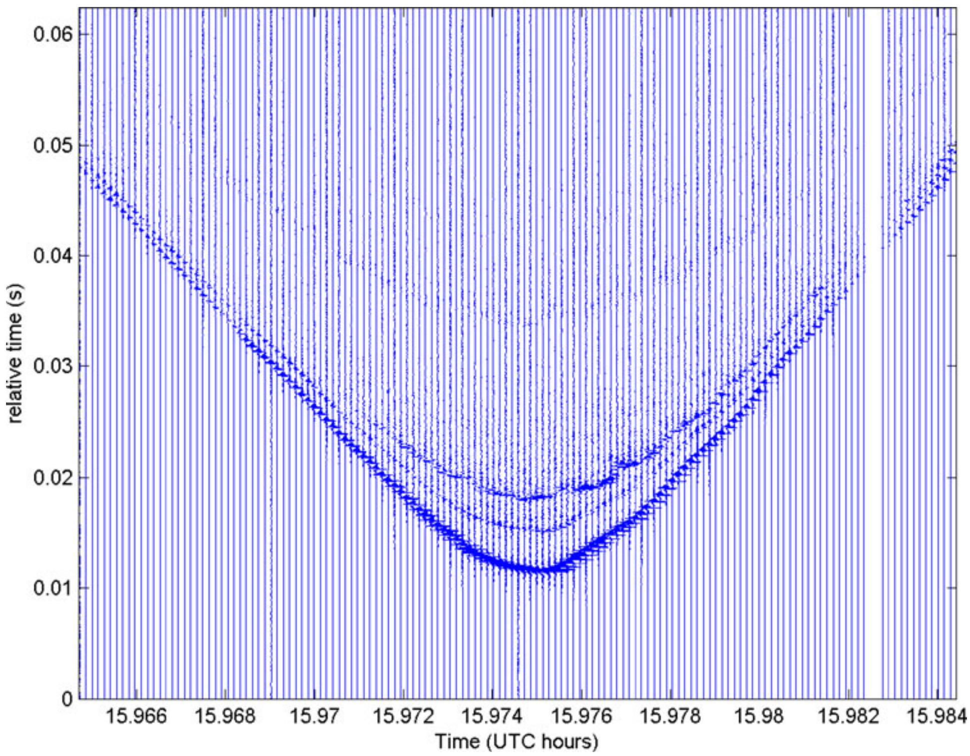


Fig. 4. Stacked pulse arrivals at the swale site. The arrival times are arbitrary, in the sense that the transmit time is not known at this stage of the processing.

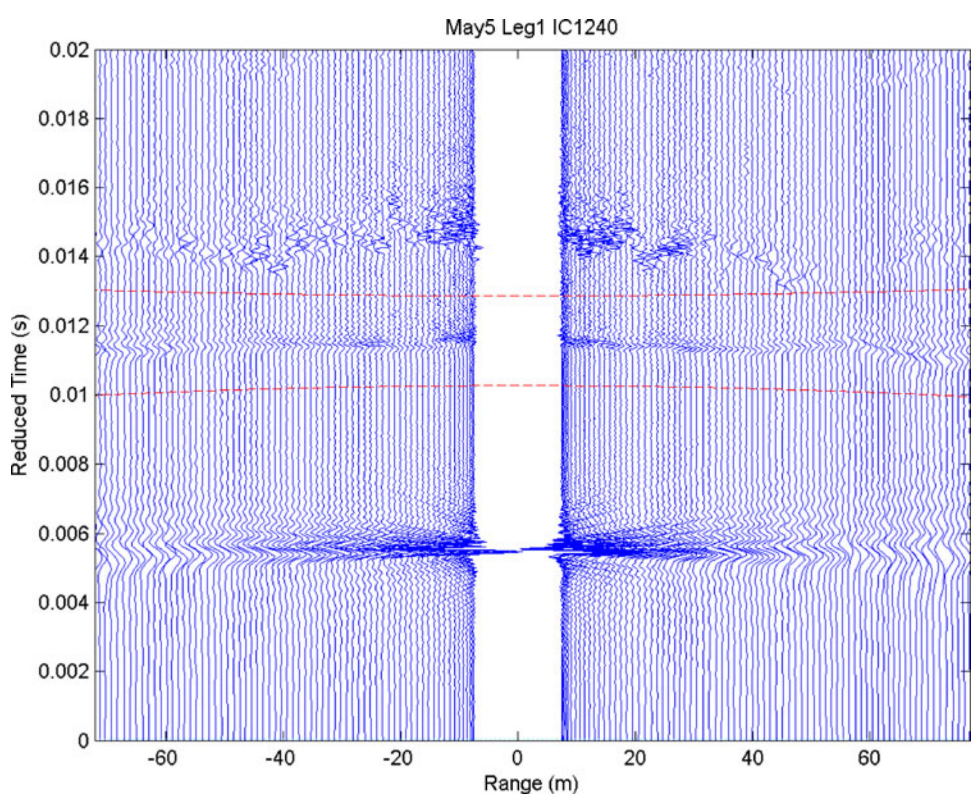


Fig. 5. Swale site measured data with Doppler corrections. The first arrival is the direct path, the second and third arrivals are the seabed and sea surface reflected arrivals, respectively. The red dashed lines show the temporal window used to estimate the seabed reflected pressure.

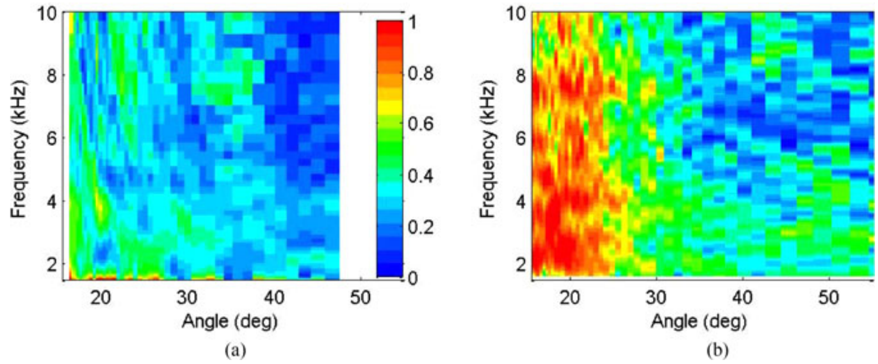


Fig. 6. Magnitude of the measured wide-angle pressure reflection coefficient at (a) swale site and (b) crest site. Note the significant difference in the reflection coefficient between the two sites indicating significant differences in seabed characteristics.

experiment increased rapidly with an incoming storm beginning with this leg. The red dashed line shows the time window used to estimate the seabed reflection coefficient. Only data from the incoming leg (negative ranges) were used for analysis, since the sea surface waves on the outgoing leg are sufficiently large to cause a leakage into the bottom reflection window at some ranges.

A window of the same size was formed around the direct path (not shown), and from data within these windows, the direct and seabed reflected pressures were estimated. The reflection coefficient is a scaled ratio of these quantities [11]. The resulting swale site reflection coefficient as a function of angle and frequency is shown in Fig. 6(a). Identical processing was performed at the crest site and the reflection coefficient is shown in Fig. 6(b). Note the significant differences between the reflection coefficients at the two sites, indicating substantial differences in seabed properties.

### *B. Geoacoustic Estimation and Hypothesis Testing*

The goal of the analysis is to estimate seabed properties from the reflection data (Fig. 6). It is instructive to first perform some simple modeling to gain insight into the information content of the data.

*1) Crest Site:* At the crest site, there is a clear critical angle at, $\theta_c \sim 25°$; from Snell's law this means that the sediment sound speed is about $c_s = c_w/\cos(\theta_c) = 1680$ m/s. This is a value associated with a sandy sediment fabric. If it is first assumed that the sediment is a homogeneous half-space, density can be estimated from the reflection coefficient $R$ at angles far above $\theta_c$ where, $\rho_s = \rho_w\, c_w/c_s(1 + \mathrm{R}(\theta \gg \theta_c))/(1 - R(\theta \gg \theta_c)) \sim 1.9$ g/cm$^3$. This value is reasonably consistent with empirical relations, e.g., [13], given a sound speed of 1680 m/s.

A second assumption is made that the incident field can be approximated by plane waves. Then the parameters and the assumptions can be tested by comparing the measured data with the modeled plane-wave reflection coefficient, Fig. 7(a). Note that the gross features of the angular dependence are modeled, however, there are substantial differences. First, the reflection data show a much greater variability above the critical angle. Second, the angular dependence of the simulation near the

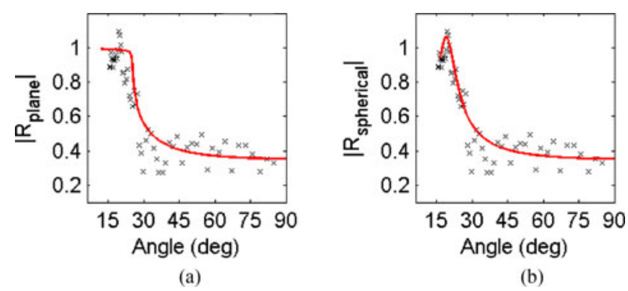


Fig. 7. Measured (x) 2 kHz pressure reflection coefficients at the crest site, and modeled results (line) assuming incident: (a) plane waves and (b) spherical waves. Note that near the critical angle, the spherical wave effects predict the data more closely. The geoacoustic parameters are given in Table I.

critical angle is not compelling. If spherical wavefronts are important, reflections at multiple angles contribute to a single reference angle, resulting in a reflection coefficient than can be greater than unity. Removing the plane wave assumption (i.e., performing the plane wave expansion for spherical waves from the source) yields the result in Fig. 7(b). Note that the behavior around the critical angle is more accurately modeled. This indicates that spherical wave effects are important for this experiment geometry and should be included. The peak in the measured and modeled data around 20° is due to the constructive interference between the classical reflected wave and the lateral wave.

It is useful at this stage to examine the forward model predictions across all frequencies. Fig. 8(d) shows the measured data in their full angular coverage. The increased dynamic range permits examination of reflection coefficients greater than unity; note especially the peak and valley structure below the critical angle that diminishes with increasing frequency. Fig. 8(a) shows the predicted angle and frequency dependence of the half-space case. The half-space assumption results differ from the measured data in the following ways.

1) Below the critical angle:
   a) the data show a "patchy" frequency dependence, whereas the model shows a smooth variation with frequency of the interference structure;
   b) the data show a general decrease in amplitude with increasing frequency, whereas the model predicts a nearly constant amplitude with frequency.

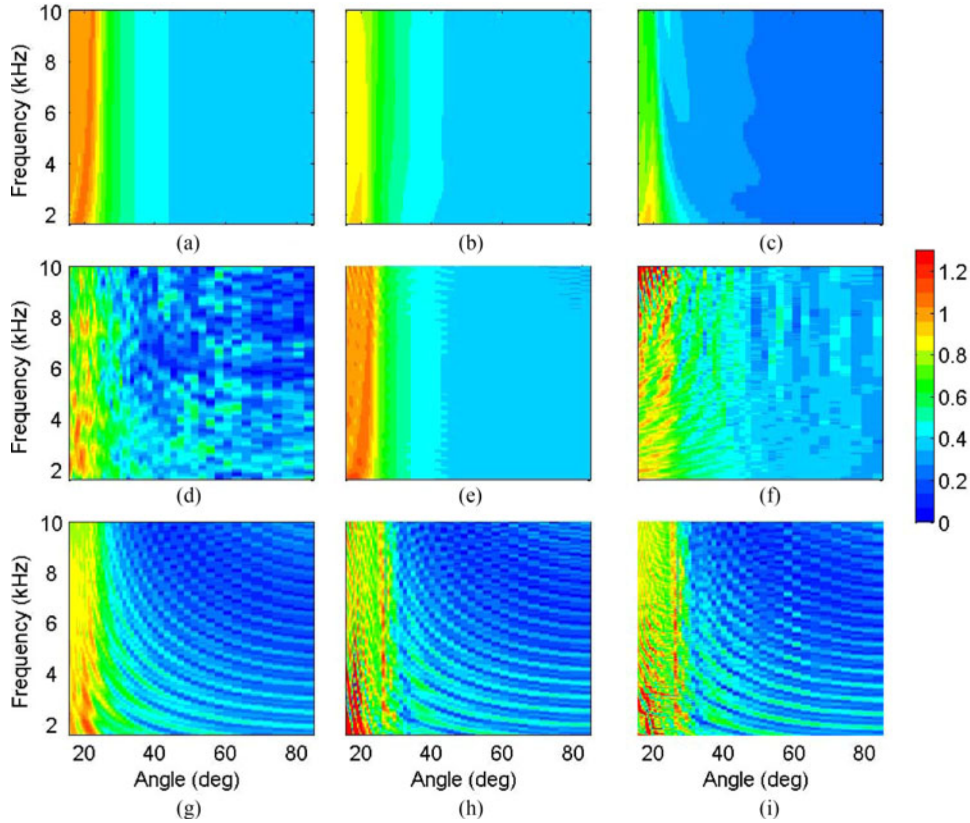


Fig. 8. Crest site spherical reflection coefficients. The measured data are shown in (d). Modeled reflection coefficients from (a) homogeneous half-space, see Table I; (b) same parameters with linear attenuation profile from the sediment interface 0.8 to 0.1 dB/m/kHz at 0.4 m subbottom; (c) same parameters as (b) with a linear sound speed and density profile from 1600 m/s and 1.6 g/cm$^3$ at the water sediment interface to 1680 m/s and 1.9 g/cm$^3$ at 0.4 m subbottom; (e) homogeneous half-space with flat interface using the L–K model, (f) same as (e) but with roughness, Table IV laser line scanner parameters and $L = 0.2$ m, (g) layered seabed, see Table II; (h) layered seabed (L–K model) flat layers, (i) layered seabed (L–K model) with rough interfaces for the two lower layers only where $w_1$ is 5 and 10 times that of Table IV (multibeam) for the 4th and 5th interface, respectively, and $L = 2$ m.

2) The measured critical angle is nearly constant with frequency, perhaps decreasing at high frequencies (above 8 kHz), whereas the modeled critical angle increases with increasing frequency.
3) Above the critical angle:
   a) the data show a broad decrease in amplitude from low angles and low frequencies to high angles and high frequencies, while the model is independent of frequency;
   b) at a finer scale, the data show some evidence of layer interference and also several reflection coefficient highlights which are generally across a band of frequencies. The model results show no structure in angle-frequency space.

It is clear that the half-space model does not capture the measured data behavior and thus further modeling was performed with the goal of explaining that behavior.

Several hypotheses were explored to explain the angular and frequency dependence at and below the critical angle. One possible explanation for the decrease in the reflection coefficient with frequency below the critical angle is gradients in the geoacoustic properties. The effect of an attenuation gradient in the upper 0.4 m is shown in Fig. 8(b), which grossly shows the overall trend in the data both in terms of the decrease in amplitude and also the nearly uniform critical angle with frequency. The hypothesized negative attenuation gradient (decreasing attenuation with subbottom depth) could be due to increased overburden pressure and concomitant increase in grain-to-grain coupling. Such coupling would be expected to lead to positive gradients in sound speed and density. The effect of including sound speed, density, and attenuation gradients [see Fig. 8(c)] yields trends slightly more similar to the data. More sophisticated gradients (e.g., exponential) were briefly explored and gave similar results.

TABLE I
CREST SITE GEOACOUSTIC PARAMETERS FOR THE HOMOGENEOUS HALF-SPACE SIMULATION

| Sound speed (m/s) | Attenuation (dB/m/kHz) | Density (g/cm$^3$) |
|---|---|---|
| 1680 | 0.05 | 1.9 |

The water sound speed is 1524 m/s. The attenuation is relatively poorly constrained.

The frequency dependent behavior of the data below the critical angle [see Fig. 8(d)] and its nonuniform angular and frequency dependence above the critical angle [see Figs. 7(b) and 8(d)] both suggest that sediment layering may be present. A hypothesized four-layer seabed (see Table II) yields the reflection

TABLE II
HYPOTHESIZED CREST SITE GEOACOUSTIC PARAMETERS

| Thickness (m) | Sound speed (m/s) | Attenuation (dB/m/kHz) | Density (g/cm$^3$) |
|---|---|---|---|
| 0.01 | 1680 | 0.8 | 1.9 |
| 0.04 | 1555 | 0.6 | 1.6 |
| 1.5 | 1680 | 0.15 | 1.9 |
| 1.4 | 1555 | 0.1 | 1.6 |
| – | 1680 | 0.05 | 1.9 |

The water sound speed is 1524 m/s.

simulation shown in Fig. 8(g). The layered simulation mimics the data behavior much better below the critical angle, capturing both the "patchy" behavior with frequency and the diminishing amplitude as frequency increases. The layered simulation also captures the near frequency independence of the critical angle. At angles above the critical angle, the simulation captures the broad decrease in amplitude from low angles/frequencies to high angles/frequencies much better than the other models. Also, the evolution of the simulated interference pattern over angle and frequency is similar to that of the data between 30°–60° and 3–10 kHz, though the data show fewer and weaker interferences. It seems plausible that some mechanism has highly perturbed their structure. That is, the simulation has a much more regular structure than the data and does not capture the "highlights" that persist across frequency in the measured data.

Important aspects of the layered simulation [see Fig. 8(g)] include the presence of two identical intercalating sediment layers,[2] and an attenuation gradient with depth (from layer to layer). The layered model is speculative. From a geologic process point of view, it is not clear how sediment layers with a nonnegligible fine-grained component would be present on the ridge crest, but this could be possible from a large storm or hurricane. If such a process did occur, multiple events at different times creating multiple layers would be plausible. Other hypotheses, interface and subbottom roughness, Fig. 8(f) and (i), respectively, will be discussed at a later point (end of Section III).

The modeling here assumes that the sound speed in a given layer is independent of frequency, i.e., no dispersion. This assumption can be examined by inspection of the frequency dependence of the critical angle in Fig. 8. First note that with spherical wave effects, the critical angle increases with increasing frequency due the reduction in Fresnel zone size (and associated averaging over vertical angle). This can clearly be seen in Fig. 8(a) with no dispersion. If positive dispersions (an increase in sound speed with frequency) were present, this would lead to an even greater increase in the critical angle with increasing frequency. However, the data [see Fig. 8(d)] indicate that there is no substantial change in the critical angle with increasing frequency. Thus, with the homogeneous half-space assumption, to fit the frequency dependence of the observed critical angle, negative dispersion (decreasing sound speed with increasing frequency) must be invoked. Negative dispersion can only be invoked when many large scatterers are present of the order of or greater than the wavelength. While shells and shell fragments do exist in the sediment, their size is much smaller than what would produce negative dispersion.[3]

Since the half-space assumption fails to explain the frequency dependence of the critical angle, some kind of structure in the seabed must be presumed. Here, two explanations for the critical angle frequency dependence are posited, gradients [see Fig. 8(b) and (c)] or layering [see Fig. 8(g)]. Either mechanism, or potentially both together, give a reasonable explanation for the frequency dependence of the critical angle.

The "perturbed" somewhat random pattern above the critical angle in the measured data was surprising inasmuch as extensive prior reflection measurements at other locations showed a clear interference pattern (as just one example, consider Fig 4(a) of [14]). Without the interference pattern, it seemed highly likely that inversions based on a plane-layered medium (e.g., [6]) would fail since this is clearly a poor approximation here. Nevertheless, for "completeness," a trans-dimensional Bayesian inversion was attempted, which resulted in an unsatisfactory half-space solution, similar to Fig. 8(a).

The observations at the ridge crest site are summarized as follows.

1) There is clear evidence that spherical wave effects are important, i.e., the presence of the interference structure below the critical angle caused by the lateral wave.
2) The frequency dependence of the observed critical angle:
    a) suggests weak or no sound speed dispersion from 1.5–10 kHz;
    b) cannot be explained by a homogeneous half-space, some kind of structure must be present;
    c) can be explained by layering.
3) The observations below the critical angle:
    a) cannot be explained by a homogeneous half-space, some kind of structure is present;
    b) suggests that layering is present, layering with gradients in sound speed, density, and attenuation is also plausible.
4) The observations above the critical angle:
    a) do not support a homogeneous half-space model. Some kind of structure is present;
    b) the (unknown) sediment structure leads to a broad reduction in the reflection coefficient with increasing frequency and angle and also adds a largely random looking pattern of reflection highlights;
    c) weakly suggest layering due to vestiges of interference patterns seen from 3–10 kHz;
    d) are partially explained by plane layering, but plane layering does not explain the randomness.

*2) Swale Site:* Inspection of the reflection data at the swale site [see Fig. 6(a)] shows no critical angle (i.e., an angle below which the reflection coefficient is approximately

[2]The intercalating model with two identical sediments was the simplest way (following Occam's razor) to build up a layered model, i.e., using known sediment speeds for two distinct sediment types and assuming that some process, e.g., large storms, creates inter-bedding from two different sediment sources (e.g., estuarine and marine). Other different layered models could be postulated.

[3]Unpublished modeling by Todd Hefner based on sediment grain size analysis indicates that negative dispersion is not expected for frequencies below about 100 kHz in this area.

TABLE III
SWALE SITE GEOACOUSTIC PARAMETERS

| Thickness (m) | Sound speed (m/s) | Attenuation (dB/m/kHz) | Density (g/cm$^3$) |
|---|---|---|---|
| 0.65 | 1555 | 0.45 | 1.6 |
| | 1680 | 0.2 | 1.9 |

The water sound speed is 1524 m/s.

unity). This means that the sound speed must be less than $c_s \leq c_w/\cos(\theta_{\min})$, where $\theta_{\min}$ is the minimum observed angle in the measurement. This leads to $c_s \leq 1585$ m/s. The lower sound speed (relative to crest site) was not surprising given that core data taken on the ebb tide delta showed a significant fine fraction [10].

Inspection of the swale site reflection data clearly shows an interference pattern below 30°. The interference pattern is caused by classical quarter-wavelength ($k_{\mathrm{jz}} d_j = m\pi/2$) and half-wavelength resonances ($k_{\mathrm{jz}} d_j = m\pi$), where $k_{\mathrm{jz}}$ is the vertical component of the wavenumber in the jth layer, $d_j$ is layer thickness, and *m* is an integer. These relations indicate a single layer and provide means to estimate layer thickness, ~0.65 m. The layer properties were informed by analysis of normal incidence reflection data (see Section IV) and are given in Table III.

The underlying half-space properties were informed by [10] which indicated that the mid-sand-sheet reflector was below the poorly sorted sediment by about 1 m or less, which conforms closely with the layer thickness, 0.65 m estimated from the wide-angle reflection data. Lacking other specific information, we assume the same properties for the mid-sand-sheet-reflector as the sand at the crest site (see Table III). The simulation result [see Fig. 9(b)] based on this geoacoustic model shows an interference pattern that is reasonably similar to the data [see Fig. 9(a)] at angles below 30°. The interference pattern at steeper angles is not apparent in the data. Fig. 9(c) and (d) will be discussed in the following section.

*3) Effect of Rough Boundaries:* It was hypothesized that perturbation of the interference pattern could be caused by layer roughness. This hypothesis was explored by forward modeling using the same geometry as in the at-sea experiment. The reflected field was computed in the time domain from a point source and receiver above a layered seafloor and the reflected time series data were then processed in the same manner as the measured data. The principle approximations in the model (see [15]) are the tangent-plane approximation, the Born approximation (multiple reflections between interfaces are neglected), and the flat-interface approximation for computing the transmitted field. The latter two approximations follow closely from Langston [16] and thus the model will be referred to as the Langston–Kirchhoff (L–K) model. The roughness is parameterized assuming a von Karman spectrum, $W(k) = w/(k^2 + L^{-2})^{\gamma/2}$, where *k* is the spatial wavenumber, *w* is spectral strength, $\gamma$ is spectral exponent, and *L* is the spectral cutoff length.

The L–K model was verified first with flat interfaces by a comparison with numerical evaluation of the Sommerfeld integral (which is an exact solution of the reflected field from a point source above a plane-layered medium). It was then verified for rough interfaces using a time-domain finite-difference software package Simsonic [17] for the layered environment of Table III and a realization of roughness parameters discussed in the following paragraphs. The L–K model is capable of treating both 2-D and 3-D environments (1-D and 2-D rough surfaces) and a few 3-D simulations were performed. The 3-D computations were 400 times slower than 2-D for the frequency range and spatial domain of the simulation problem here. Since the general trends and features of the 3-D and 2-D models were similar for this environment and geometry, the 2-D model was used most extensively and those results are presented here. The L–K model also treats in-plane and out-of plane dipping layers, but for the simulations here, the mean interfaces were assumed to be parallel to the sea surface.

The goal of the simulations was to determine if general features of the interference perturbations in the data at both swale and crest sites could be explained by interface roughness. As far as was practical, environmental parameters were drawn from measurements at each site.

*a) Swale Site:* The geoacoustic properties at the swale site (see Table III) were inferred by modeling. 1-d roughness statistical parameters, Table IV, were estimated by Hefner [18] from laser line scanner from the water sediment interface. Though the laser line scanner data were collected on a ridge, not a swale, these were assumed to be pertinent to both environments. Since no estimates of the spectral cutoff were available, five realizations were drawn for various values of spectral cutoff length, *L*. Each realization consists in applying the von Karman spectrum with the different cutoff length on an identical white random spectrum (but different between the water-sediment interface and the base of the layer). The Gaussian distributed interface slopes for these parameters have a standard deviation of 3° at $L = 0.03$ m and 9° at the maximum spectral cutoff value, $L = 1.8$ m.

No roughness measurements were available for the lower layer boundary and as a first approximation, the roughness statistics were assumed to be identical at both interfaces. The simulation results are shown in Fig. 10. Note that high reflectivity values near 10 kHz at 15°–25° are numerical artifacts.

Before discussing the simulations, it is helpful to consider effects of the Fresnel zone, or the size of the insonified region on the rough surface (see Fig. 11). The smallest in-plane Fresnel radius is about 1 m, which occurs at the highest angle and frequency. The largest in-plane Fresnel radius is about 10 m which occurs at the lowest angle and frequency. The Fresnel radius is an important spatial scale that significantly affects how the roughness influences reflection. Returning to the reflection simulation with rough boundaries (see Fig. 10), the results in the first row, $L = 0.03$ m, indicate that roughness has practically no effect on the reflection coefficient at all angles and frequencies. This can be understood by comparing $2\pi L$ with the Fresnel radius, $\xi$. When the Fresnel zone is much larger than the cutoff scale, ($\xi \gg 2\pi L$), the acoustic field at the receiver is averaged across many roughness scales, and the roughness has little net effect on the reflection coefficient.

When $2\pi L$ is on the order of and larger than the Fresnel zone and there is sufficient power in the low wavenumber part of the

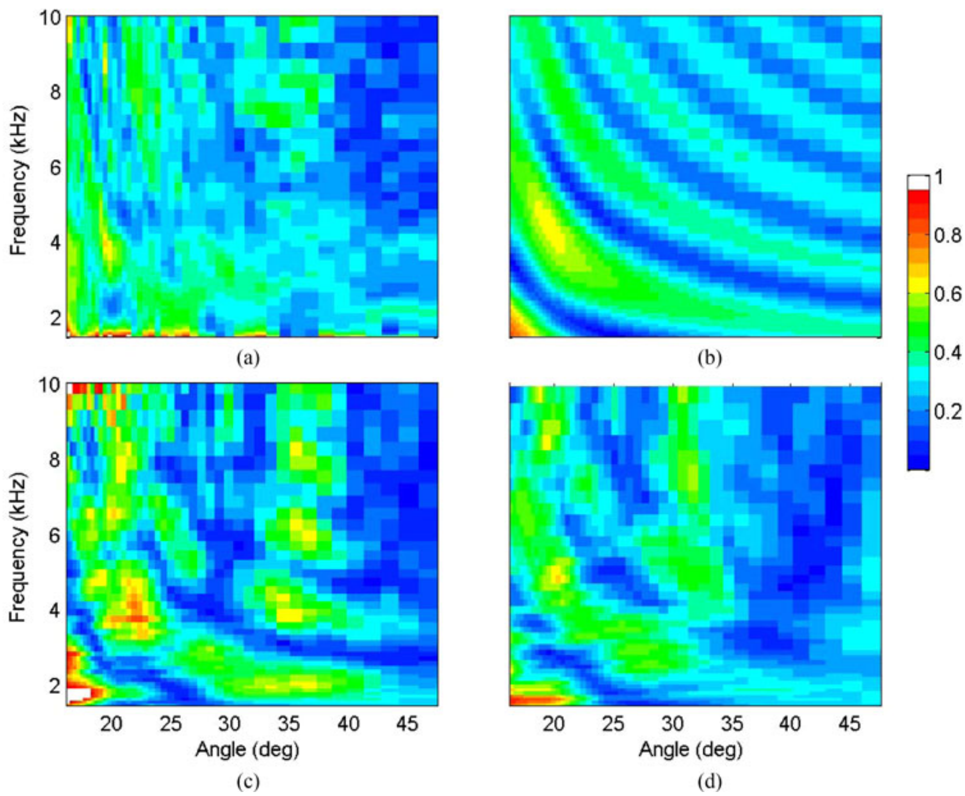


Fig. 9. Swale site seabed reflection (a) data and (b)–(d) simulations. (b) single plane layer over a half-space (see Table III), which roughly captures the measured data below 30°, (c) Table III with roughness parameters of $L = 0.6\,\mathrm{m}\,\gamma_1 = 3.43\,w_1 = 0.0039\,m^4$ for the top and bottom of the layer and (d) same as (b) with $L = 0.3$ m and modified basement parameters of 1640 m/s and 1.65 g/cm$^3$.

TABLE IV
ROUGHNESS PARAMETERS USED IN THE SIMULATIONS

| Data Source | 1-D spectral strength $\boldsymbol{w}_1$ $(m^4)$ | 1-D spectral exponent $\gamma_1$ |
|---|---|---|
| Laser line scanner [18] | $3.9 \times 10^{-3}$ | 3.43 |
| Fit to multibeam and laser line data (Appendix 2) | $2.12 \times 10^{-5}$ | 1.85 |

heterogeneity spectrum, the roughness plays a more significant role and the interference pattern is perturbed. This can be seen in row 2, $L = 0.2$ m (Fig. 10), for the high angles and high frequencies (above ∼5 kHz), where the interference pattern is perturbed. Note that at low angles and frequencies, however, the interference pattern is not perturbed much, since in that region $\xi \gg 2\pi L$.

It is useful at this point to refer back to measured data, Fig. 9(a). The fact that the interference pattern is most clearly visible at low angles can now be understood in light of Fresnel zone effects. Note also that the Fresnel zone (see Fig. 11) is a relatively weak function of frequency at the low angles, say below 30°; the data show this same trend. That is, the interference pattern is most clearly seen in the data below 30° and at all frequencies with some minor perturbation at higher frequencies.

As the spectral cutoff increases further, e.g., $L = 0.6$ m in row 3, Fig. 10, more of the frequency-angle domain is affected by the roughness and broad patterns emerge. For example, in row 3 realization 1, there are reflection peaks at 30°, 40°, 50°, 80° that can be seen across a range of frequencies. The broadband nature can be explained by focusing from seabed curvature (from either layer interface). Theory predicts that the reflection amplitude due to focusing increases with increasing frequency. For example, above a concave hemispherical boundary, the focused field amplitude (i.e., reflection) at a distance equal to the radius increases linearly with frequency (e.g., [19]). This amplitude increase is simply a manifestation of conservation of energy, where the size of the "focal spot" decreases with increasing frequency. One example of this can be seen in row 5 realization 2 at about 55°, where the high reflection coefficient due to focusing increases in amplitude and narrows in angular range with increasing frequency (due to the diminishing in size of the focal spot). The oscillatory behavior of the frequency dependence in this (and other examples in Fig. 10) are caused by the interaction of the focusing with the layer interference pattern.

Adjacent to the broadband focusing highlights, there are broadband nulls. These are caused by defocusing (convex regions of the seafloor within the Fresnel zone). For each roughness realization, the focusing/defocusing regions move to different locations in angle space (as expected). A key point here is that interface curvature can perturb (or even destroy) the interference pattern. The defocusing effects also appear in the measured data. Note that the broadband reflection highlight at about 35°, Fig. 9(a), may be from focusing and the reflection nulls on either side due to defocusing. The data are

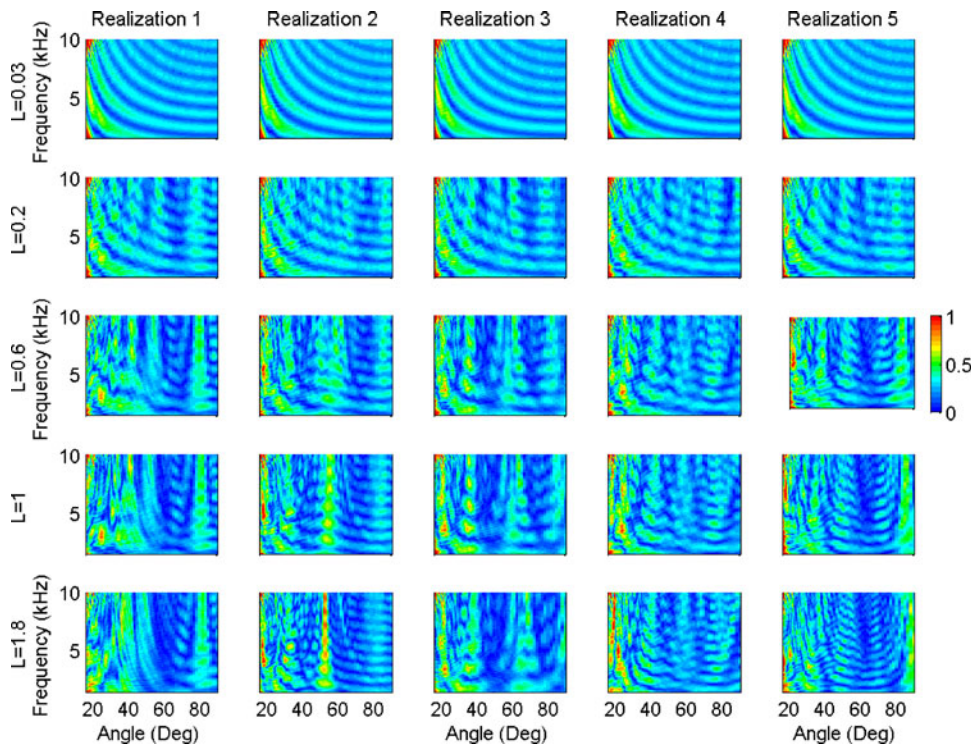


Fig. 10. Simulation of experiment data, i.e., using the same experiment geometry, with estimated roughness values from laser line scanner data, Table IV, for various realizations (columns) and values of spectral cut-off, $L$ (rows). Geoacoustic properties are given in Table III.

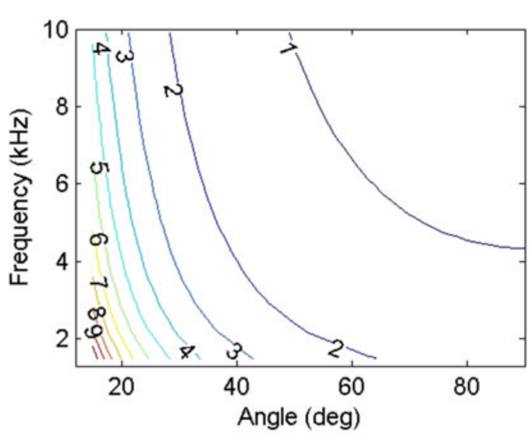


Fig. 11. In-plane Fresnel zone radius for the experimental geometry employed in the reflection measurements.

compared with simulation in Fig. 9(c) ($L = 0.6$ m, realization 3 in Fig. 10). Note that the simulation and observations show a number of similar features as follows:

1) the existence of a broadband reflection highlight at 35°;
2) the highlight oscillates in frequency;
3) there are reflection nulls on either side of the highlight; and
4) the null is less "deep" at shallow angles (25°–32°) than at steeper angles (40°–48°).

The simulation in Fig. 9(c) clearly has stronger perturbations than observed in the data; the simulation result for the same realization with $L = 0.2$ m show weaker perturbations (see $L = 0.2$ m, realization 3 in Fig. 10). A spectral cutoff length $0.2 < L < 0.6$ m was expected to give a closer match to the data, which is the case seen in Fig. 9(d) with $L = 0.3$ m. In Fig. 9(d) results, the basement sound speed and density were reduced (see caption) to mimic a positive density and sound speed gradient in the upper layer. The primary effect of the gradient with respect to the reflection coefficient for this problem is to lower the impedance contrast at the basement. Reducing the basement sound speed and density is commensurate and computationally simpler. The net result of the gradient, or reduction in basement impedance contrast, is to reduce the peak-to-null amplitudes in the interference pattern. The simulation in Fig. 9(d) captures much of the structure in the measured data. Though it appears that in the measured data, the impedance contrast between the two layers was even lower than modeled, further tuning of the geoacoustic or roughness parameters was not attempted.

The simulation is instructive on one other point, i.e., the reflection coefficient is only weakly sensitive to $L$ values much greater than the Fresnel zone. This can be seen in Fig. 10 by examining the similarity of the reflection coefficient for a given realization when $L \geq 0.6$. From an information content point of view, this means that the presence of perturbed interference patterns in measured data can inform a lower bound to $L$, but cannot inform an upper bound if the data space is such that $\xi \ll 2\pi L$.

In addition to the roughness parameters from the laser line scanner (spatial resolution 4 mm), it was desirable to estimate roughness parameters from multibeam bathymetry data [20] (spatial resolution 1 m). This was of interest since the spatial wavenumbers that control reflection are smaller than those estimated by the laser line scanner. The 1-D spectral parameters estimated from the bathymetry data, are quite different (details are given in Appendix II). The roughness parameters used in simulations (see Table IV) were derived by a fit across the multibeam and laser line data, ignoring the low wavenumber part of the laser line data.

The reflection coefficient simulation with these parameters showed a weak perturbation of the interference pattern for all values of *L*. Even at large values of *L*, the perturbations to the interference pattern were much weaker than those in the data. This is so because for a relatively low spectral exponent, the small-scale roughness (high wavenumbers) imposed on the large-scale curvature (low wavenumbers) prevent high coherence required for significant focusing. When the spectral exponent is relatively high, the power in the large-scale roughness/curvature is large compared to the small-scale roughness so that strong focusing can occur (as in Fig. 10). Thus, two conditions are needed for focusing, a relatively high spectral exponent and $2\pi\mathrm{L}\sim > \xi$.

It was clear that the multibeam bathymetry-derived roughness parameters at the top and bottom of the layer could not explain the observations. This left the possibility that a subbottom interface with higher roughness at low wavenumbers could explain the data. This seems plausible since the lower layer is coarser grained in nature, and could have formed in a higher energy environment (e.g., lower sea level) than the upper layer. This possibility was explored using the bathymetry-derived spectral parameters at the water sediment interface with $L_{\mathrm{top}} = [\,0.15, 1, 3, 5, 9]$ m, and the laser line scanner parameters on the lower layer with $L_{\mathrm{bottom}} = [\,0.03, 0.2, 0.6, 1, 1.8]$ m. Note that the spectral cutoff value of *L* is five times smaller at the bottom of the layer than at the top; this was done because using the $L_{\mathrm{top}}$ values for the bottom layer would lead to unreasonable values of rms roughness in the bottom layer.

The reflection simulation results using a higher roughness at the lower layer showed generally weaker perturbations than Fig. 10 (as expected) and most of the 25 results (5 realizations times 5 values of *L*) showed weaker interference perturbations than the data. One realization showed strong perturbations, but this was due to a peak in the bottom layer height. The peak led to a very thin layer thickness (0.2 m) at ∼30° and a highly perturbed interference pattern, but quite dissimilar to the data. The case of equal (laser line scanner) roughness statistics at both interfaces (see Fig. 10) exhibited features more similar to the data than did this simulation.

*b) Crest Site:* Returning now to the crest site, interface roughness effects were explored also using the L–K model. Before discussing the roughness simulations, the L–K model was tested with a flat interface [see Fig. 8(e)] and comparing it with the exact solution [see Fig. 8(a)]. Note that the L–K model captures the relevant physics quite well both at and below the critical angle. This gave some confidence in applying the model to the crest site. Roughness effects were simulated using the laser line scanner roughness parameters (see Table IV) with $L = 0.03, 0.2, 0.6, 1.8$ m for five different roughness realizations. The result that was most similar to the crest site data is shown in Fig. 8(f), where the high levels from 9–10 kHz and 15°–25° are numerical artifacts. Note several broadband features from focusing/defocusing. Though a few similar features are seen in the observations [see Fig. 8(d)], the similarities are not compelling and the differences are significant. The agreement below the critical angle is rather poor and roughness does not explain the reduction in the reflection coefficient at high frequencies and high angles. The other simulations L ≥ 0.2 m had much stronger focusing/defocusing effects than observed in the data.

Simulations were also performed at the crest site for roughness in the layered case. Again, the L–K model with flat layer interfaces [see Fig. 8(h)] was compared with the exact solution [see Fig. 8(g)]. The model performs well above the critical angle, but poorly below the critical angle due to the neglect of multiple interactions within a layer, and the presence of thin layers in the geoacoustic parameters (see Table II). Both roughness parameter sets from Table IV were employed to model roughness at all and combinations of several layers. For many of the realizations, there were strong focusing/ defocusing effects not observed in the data. The realization shown, Fig. 8(h), approximately captures the higher levels at about 60° across a wide frequency band seen in the data, Fig. 8(d). However, the simulation still has a more organized frequency-angle behavior than does the data.

In summary of the crest site simulations, interface roughness added to the half-space and layered cases led to some (modest) changes in predicting trends observed in the data. The angular and frequency dependence with roughness do not closely mimic the observations. Another possibility for explaining the observations is sediment volume heterogeneities. This was not explored.

## IV. Normal Incidence reflection

The wide-angle reflection analysis considered two locations —a ridge and a swale separated by ∼6 km (see Fig. 2). The motivation for the normal incidence measurements was to understand the lateral variability of the water-sediment interface at smaller scales, from O(1) m to O(100) m.

The normal incidence reflection coefficient was measured using a reference hydrophone approximately 2 m above the source on the same tow cable and was collected at the same time as the wide-angle measurements. Reference phone problems rendered data viable only along one 440-m track (May 9, 2013) but fortuitously this was close to the swale site wide-angle reflection track, see Fig. 12(a). Due to the tight geometry constraints on the source depth and maximum depth of the source tow cable required by the wide-angle data, the sea surface reflected path on the reference hydrophone arrived before the bottom reflected path by only ∼1.6 ms. On the track with viable data, the sea surface was sufficiently rough so that the scattered coda from the sea surface path obscured the arrivals following the bottom reflection, but did not bias the bottom reflection peak. Thus, instead of being able to use the bottom reflected time series and form a frequency domain reflection coefficient, the magnitude of the peak broadband (1.4–12 kHz) bottom reflection coefficient was used to make inferences of the sediment properties near the water-sediment interface (∼upper 0.15 m).

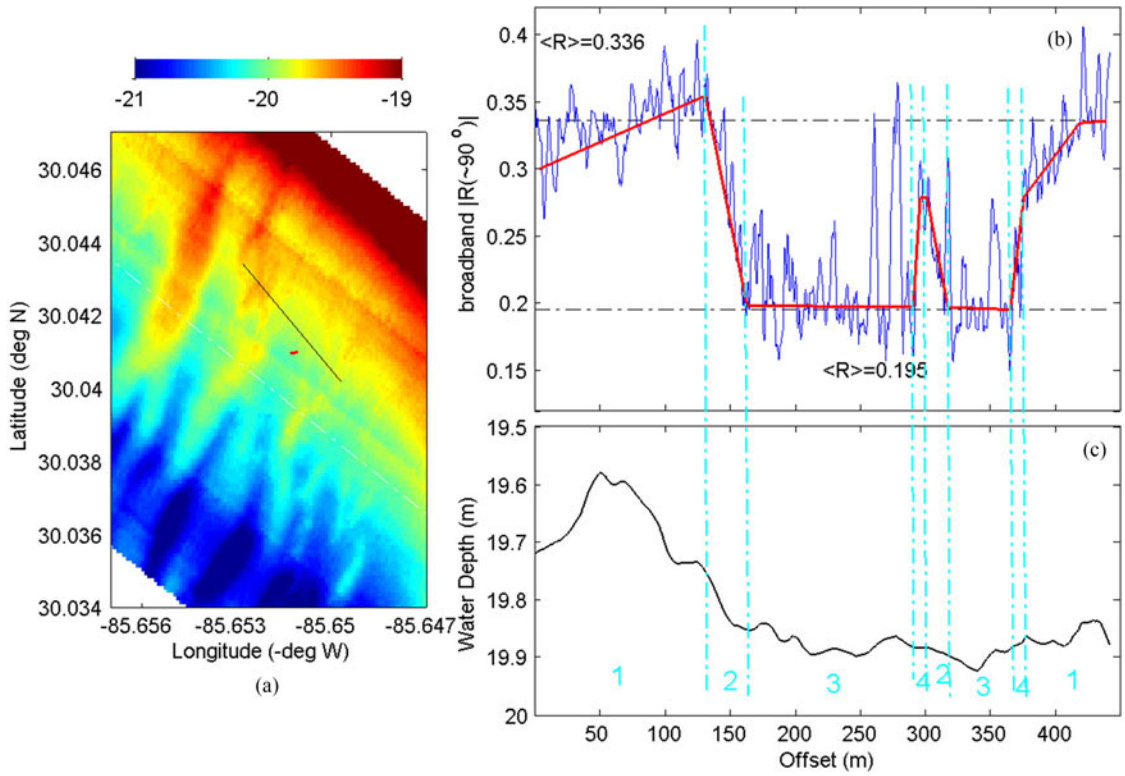


Fig. 12. (a) Bathymetry (meters) with normal incidence reflection track (black line) from northwest to southeast. The swale site wide-angle reflection track is shown in red trending west-southwest (the line indicates only the bottom interacting portion of the track); (b) Normal incidence reflection coefficient data (blue) along with interpreted "reflection regimes" (cyan dotted lines and numbers) and a simplified fit (red) to the data. (c) Along-track 10 m resolution bathymetry data from [20].

The reflection coefficient was computed by taking the ratio on every ping of the bottom reflected path peak and the direct path peak, correcting each for spherical spreading. Source amplitude variations were negligible, but were accounted for. The transit speed was about 1.5 m/s, and the pulse repetition rate 0.5 s, so the pulse-to-pulse offset in the specular point on the seabed is 0.75 m. Thus there is significant overlap in the Fresnel zone on consecutive pings: 72%, 53%, 32% at the lower, center, and upper end of the band, respectively (see the Fresnel zone radii in Fig. 11 at 90°).

### A. Seabed Lateral Variability at the 1–10-m Scale

The reflection results were averaged over three pings (a lateral extent on the seabed of 3.5 m at the center of the band) and are shown in Fig. 12(b) (blue line). Note the substantial drop in reflectivity at $\sim$150 m, where the change is almost a factor of 2 in amplitude. Both system (e.g., source depth or amplitude variation) and environmental factors to explain this drop were explored. However, the observed variations are not due to system effects; both the source and receiver were essentially omnidirectional, so motion from towing would have negligible impact and the source–receiver positions were carefully measured on each ping. The variability in the reflection coefficient must be due to seabed effects.

There are two other large changes (a factor of $\sim$2) in reflection amplitude: at 260 and 275 m. These were examined on an individual ping basis and it was found that each peak occurs from a single ping. Since the neighboring pings exhibit significantly lower amplitude but significant Fresnel zone overlap, the only reasonable explanation is focusing from bathymetric curvature. The increased reflectivity at 300 m by contrast occurs over many consecutive pings.

There is a spatial periodicity clearly observed in the reflection data [see blue curve in Fig. 12(b)], which was estimated from normalized data using a split window normalizer (averaging window of 9.5 m and a guard band of 12.75 m). The main peak of the spatial periodicity is at 26 m with a secondary peak at 43 m. These periodicities do not correspond with any motion of the source or receiver, thus they are not artifacts related to system effects. It is possible that there are small-scale bedforms unresolved in the bathymetry leading to either slight focusing and defocusing or that other geological processes lead to fluctuations on those scales.

### B. Seabed Lateral Variability at the 10–100-m Scale

A comparison between reflectivity and bathymetry is shown in Fig. 12(b) and (c). It should be noted first that the reflection data positions may be biased forward along the track by some meters because the source and receiver trailed slightly behind the GPS receiver fixed on the back of the catamaran. Given the measured length of cable between source and catamaran (13.4 m) and the estimated source depth, $\sim$10 m, the maximum

GPS-to-source horizontal offset, i.e., for a straight line cable, is ~9 m. The expected catenary cable geometry would reduce that offset. Currents may have deflected the source from the plane of the tow direction, but cross-track deflections would be much, much less than 9 m. In summary, the track position may be biased up to 9 m along track and a few meters cross-track. Positional errors on the extracted multibeam data are less than 1 m.

One salient point is the lack of obvious correlation between the reflection coefficient and the bathymetry. The sand ridge crest peak (at 46 m) is separated by more than 80 m from the peak of the reflection coefficient (130 m). Also, near the end of the track, there is a sharp rise in the reflection coefficient, but the bathymetry is nearly flat. Only the central and lowest part of the track has a reasonable correlation with the lowest reflection coefficient values. It is important to observe that the bathymetry varies only 30 cm along the track; the water depth changes are very small.

The reflection data suggest four regimes, which are delineated in Fig. 12(b) and (c) in the vertical dotted cyan lines and numbered 1 to 4. First, the major features are described, i.e., neglecting the small feature at about 300-m offset. Regime 1 seems related to the sand ridge crest, but oddly, the reflection coefficient steadily increases from the lee side to almost precisely halfway down stoss side (from ridge peak to trough). The current direction is from the Southeast. At this point, there is a rapid drop in reflectivity and this zone is called Regime 2. Regime 3 has generally low reflectivity values (with many peaks) and corresponds with the deepest part of the bathymetry. At about 375 m, the reflectivity rises sharply (Regime 4), even faster than the decline in Regime 2. The final portion of the track looks similar in reflectivity values to Regime 1, though with a steeper slope.

Returning now to the 23-m-long feature at 300 m, note that this occurs on the stoss side of a very small ridge or mound in the swale (the mound is about 85 m in length, ~250–335 m offset, and only 5 cm high). The rapid rise in the reflection coefficient at ~300 m has a similar slope with that at 375 m and thus is designated as Regime 4. This regime is followed by a decrease in the reflection coefficient very similar to Regime 2. In fact, the Regime 2 slope, $dR/dx = -0.005$ m$^{-1}$, where $R$ is the reflection coefficient and $x$ is offset distance, is essentially identical at 150 and 310 m. The slope in Regime 4 is about twice as large and with the opposite sign, $\mathrm{dR/dx} = 0.0123$ m$^{-1}$ at 300 m and 0.0096 m$^{-1}$ at 375 m.

In an effort to quantify the geoacoustic variability along this track, the density and sound speed were first estimated at the average value of the simplest regimes 1 and 3 (shown in black dash-dotted line). It is well known that there are numerous difficulties (i.e., ambiguities) in estimating density and sound speed from normal incidence reflection data. Reflection amplitudes are influenced by many mechanisms including roughness, sediment volume scattering, seafloor curvature, layering, gradients, and impedance changes. Resolving contribution from individual mechanisms is generally not possible and for simplicity, here, all mechanisms are ignored except the latter, i.e., the seafloor is assumed to be a perfectly flat homogeneous half-space for each consecutive ping. Ignoring the roughness can be justified by noting the reflection coefficients are averaged in space, across many roughness scales and thus should average out to the flat case. With these assumptions, it is possible to estimate the along-track sediment impedance Z (product of density and sound speed)

$$Z = Z_o \left(1 + R(\pi/2)\right)\left(1 - R(\pi/2)\right)^{-1} \quad (1)$$

where $Z_o$ is the seawater impedance. From the sediment impedance Z, the sediment sound speed and density are estimated from the empirical relations of Bachman [13]. These assumptions applied to Regime 1 ($R = 0.336$) result in a sound speed of 1684 m/s and density of 1.87 g/cm$^3$, which compare closely with the estimated sound speed (from the critical angle) of 1680 m/s from the wide-angle data at a ridge crest along the clutter track. The two crests are about 6 km apart, but the congruence of the sound speed suggests ridge crest geoacoustic properties may be similar in this region. In the swale, Regime 2 ($R = 0.195$) yields a sound speed of 1544 m/s and a density of 1.68 g/cm$^3$. This is in concordance with the nearby swale site wide-angle measurements, which indicated that the sound speed must be less than about 1585 m/s.

The fact that the approximate and average results in regimes 1 and 2 do not appear to be in gross error, suggested that including all the regimes would not be unreasonable. In this analysis, smoothing was performed such that only relatively large-scale fluctuations with a high probability of being related to geoacoustic variability were preserved. The smoothed reflection data for this part of the analysis is shown in Fig. 12(b) in the red line.

The result of applying the flat homogeneous assumptions and the empirical equations to the spatially smoothed reflection data is shown in Fig. 13. Note that there is a substantial variation in both density and sound speed across the short track. This is somewhat surprising given that the swale and crest differ in water depth only by 0.3 m. It is not understood at this time why the geoacoustic properties (impedance) increase from the ridge lee side to the crest and then continue increasing until halfway down the stoss side.

The lower sound speed and density in the swale (Regime 3) clearly indicates a higher concentration of clay and silt particles than on the ridge. In the swale, there is a significant (ostensible) change in impedance at 300 m which likely represents a band of coarser grained sediment. The width of the band is about 23 m, which is comparable to the secondary peak in the spatial periodicity (at 43 m for a full cycle, 21.5 m for a half cycle or band).

It is of interest to examine any correlations between the normal incidence reflection data and 400-kHz backscatter; see Fig. 14. It is difficult to see any clear correlation. There are two or three higher backscatter (lighter color) lines perpendicular to the track in the first one-third of the track (from Northwest to Southeast). At other locations in the survey, the high backscatter occurred on the lee side of ridges, though it is not clear here if these features are related bathymetry [see the first 135 m; Fig. 12(c)]. In general, there does not appear to be strong correlations between the 400-kHz backscatter and the 1.5–10-kHz reflection data, except to note that the third lineal feature is roughly the end of Regime 1 (which may be coincidental) and

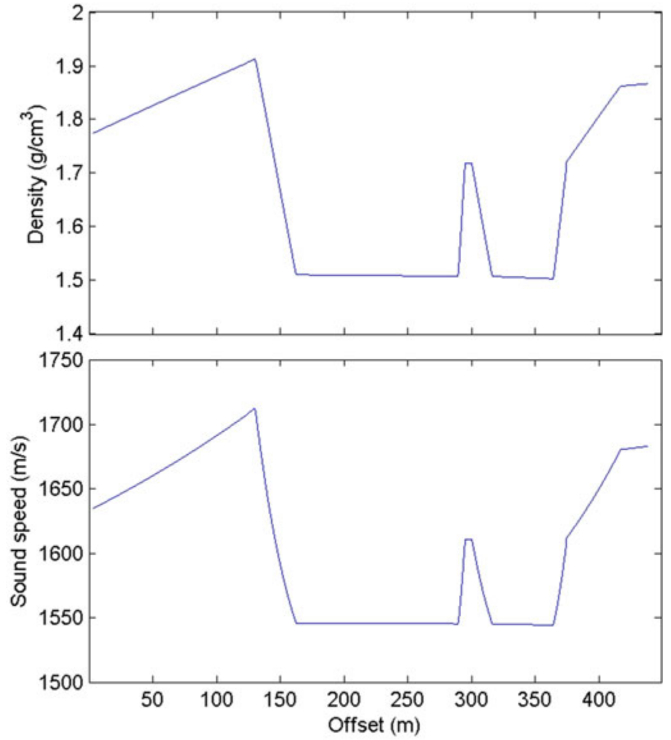


Fig. 13. Estimated density and sound speed from smoothed normal incidence reflection data along a track [see red line in Fig. 12(b)] from Northwest to Southeast near the TREX13 main reverberation line.

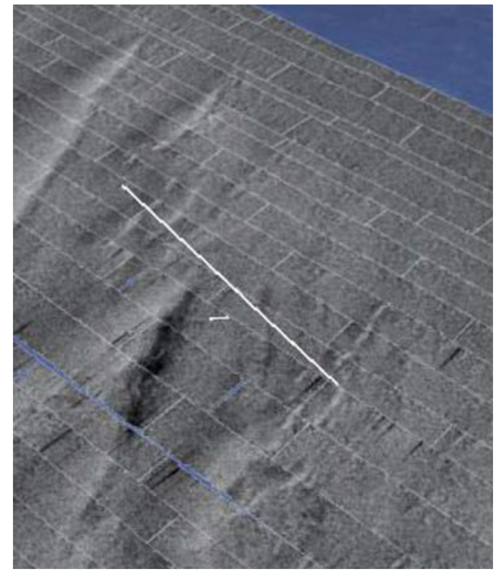

Fig. 14. Multibeam backscatter data [20] with normal incidence track (white line trending from Northwest to Southeast, ~440 m in length) and wide-angle track (short East-west white line, ~25 m in length). The gray scale spans 23 dB with 0 dB in black and 23 dB in white.

the lineal features are separated by about 40 m, which was a scale apparent in the reflection data. One potential correlation is that the band of high reflection (likely coarser sediment) at 300 m [Fig. 12(b)] is near the slightly lower (darker) backscatter, at about 2/3 of the distance along the track (from Northwest to Southeast).

The backscatter data do not show any strong variations along the wide-angle reflection track (short white line trending East–West). There is, however, a thin lower backscatter (darker) arc which intersects the track near its center. It is not clear what the implications of this are. Also note that the otherwise apparent uniformity of the backscatter for the rest of the short track should not necessarily suggest surficial sediment homogeneity (given the lack of correlation of the high frequency backscattering with the normal incidence reflection track).

## V. Summary and Conclusion

Measured wide-angle and normal incidence seabed reflection coefficients off the coast of Panama City, FL, USA, contain valuable information on the geoacoustic properties. However, the most potentially informative (wide-angle) observations at two sites also raised a puzzling question. Neither dataset showed the usual (in our experience) interference pattern caused by classical one-half and one-quarter wavelength resonances that occur in plane-layered media. Though there is evidence for layering at the swale site and the crest site, a mechanism (or mechanisms) exists that perturbs the interference patterns. Since the interference patterns require flat parallel boundaries, boundary roughness is one hypothesis for the perturbations. A second possibility is the presence of strong volume heterogeneities which would lead to decorrelation of the up and down-going wave fields in a layer.

Only the roughness hypothesis was examined. Simulations performed at the swale site explored the effects of roughness on the wide-angle interference patterns. The simulations showed similarities with measured data when 1) the spectral exponent was large, i.e., much greater power in the low spatial wavenumber spectrum relative to that in the high wavenumbers; and 2) the Fresnel zone was of the order or smaller than $2\pi L$, where $L$ is the spectral cutoff. The main mechanism was focusing and defocusing of the acoustic field due to interface curvature, which results in broadband peaks and valleys superposed on the interference pattern and in some cases destroying the interference pattern entirely.

The broadband peaks/nulls in the swale site data appear to be due to focusing/defocusing. The roughness hypothesis appears to be correct at this site inasmuch as simulations showed features similar to the measured data. Furthermore, an alternative hypothesis of scattering from volume heterogeneities would not produce focusing and defocusing. Though the evidence is strong, the roughness hypothesis cannot be completely verified inasmuch as layer roughness statistics are insufficiently known. The lower layer roughness statistics are not known at all (and very difficult to obtain), and the water-interface statistics are incomplete (lacking an estimate of spectral cutoff) and uncertain. Two estimates of the roughness statistics were considered: one derived from laser line scanner data which indicated focusing comparable to the data when the spectral length was employed as a free parameter. The roughness statistics derived from multibeam bathymetry data did not show comparable focusing for any reasonable value of spectral cutoff length. In summary, simulations indicate interface roughness is the likely explanation for the swale data interference perturbations.

Normal incidence reflection data were employed to estimate surficial sediment sound speed and density along a track extending from one ridge to the swale and partially onto another ridge. The track was located ~3.5 km Southeast from the TREX13 moored reverberation source and receiver, where poorly sorted sediments associated with the ebb tide delta dominate the surficial sediment fabric. The elevation change between ridge and swale there is rather small, about 0.3 m. The normal incidence data showed clear signs of focusing effects, adding additional credence to the roughness hypothesis as an explanation for the nearby swale site measurements.

In summary, the sediment geoacoustic observations from the wide-angle and normal incidence reflection measurements indicate the following.

1) The wide-angle reflection data at the crest site show the following.
    a) The data cannot be modeled with the assumption of a homogeneous half-space. The half-space assumption does not correctly model the angle or frequency dependence of the data below the critical angle, at the critical angle or above the critical angle.
    b) The data can be modeled reasonably well with the assumption of layering. The layered assumption leads to general correspondence with the data below the critical angle, at the critical and (largely) above the critical angle. It does not capture seemingly random perturbations at some angles above the critical angle. These perturbations might be explained by the addition of layer roughnesses, but more likely by the addition of volume scattering within the layer. Sound speed, density, and attenuation gradients also seem to be important in explaining the data.
    c) The data indicate that the sound speed was nearly independent of frequency, 1.5–10 kHz, due to the behavior of the critical angle.
    d) The data yield a sound speed and density similar to that at a ridge close to the swale site 6 km to the east.
2) The wide-angle data at the swale site can be modeled with a single layer with roughness at both boundaries. Since there is a low-angle interference pattern, the data cannot be modeled by the half-space assumption. The roughness parameters that reasonably explain the data were derived from laser-line scanner data measured at the water-sediment interface and applied also at the subbottom layer interface with spectral cutoff treated as an unknown (free) parameter. A spectral cutoff value of $L = 0.3$ m yields simulated results comparable to the measured data.
3) Normal incidence reflection along a 440-m-long track near the swale site indicates the following.
    a) The clear presence of focusing/defocusing, which strengthens the focusing/defocusing interpretation at the nearby swale site.
    b) Four distinct geoacoustic regimes from one ridge crest to another that appear loosely correlated with bathymetry: lee to stoss side of ridge crest, halfway down the stoss side to the base of the swale, the swale, and the transition between the swale and the lee side of the next ridge crest [see Figs. 12(b) and 13]. In the swale regime, there is a small mound, 5 cm in height that exhibits regimes that are similar to those on the larger ridges.
    c) Substantial geoacoustic lateral variability. For example, the sound speed changes from 1550 to 1700 m/s in a lateral distance of 20 m on the stoss side of the ridge. The change appears to be related to water depth and position on the ridge, but water depth differences that separate the two sound speeds are only about 0.1 m [see Figs. 12(b) and 13].
    d) Spatial periodicities of 26 and 43 m, suggesting a spatial periodicity in the sediment structure in the swale.

The underlying cause of the geoacoustic variations, e.g., the geologic and/or hydrodynamic mechanisms that control the geoacoustic spatial variability are not understood at present.

The analysis did not employ the planned plane-layered inversion methods. Nevertheless, the sediment properties presented here, though somewhat crudely estimated from theory and forward modeling, may have some value for future scattering, propagation, and reverberation studies.

## APPENDIX I

### A. *Geometry Reconstruction*

Neither the time nor position was measured with sufficient accuracy at the source and receiver to determine the precise time of signal transmissions. Thus, instead of having absolute travel times, relative travel times between direct and bottom reflected, and direct and sea surface reflected arrivals were employed to estimate source–receiver offset and other parameters of interest. A ray-based forward model [21] was applied in a Bayesian inversion framework to estimate the source–receiver offsets (ranges), reflection angles at the seabed, source depth, and water depth together with rigorous uncertainties for all parameters.

Fig. 15 shows a representative result for the measured relative travel time data (blue) and the fits (red) for two receiver depths. The first 120 data points are the direct-bottom relative travel times for the upper receiver. The second 120 data points are the direct-surface relative travel time data and fits for the upper receiver. The variation in measured travel time fits from sea surface swell is apparent (blue line from 120–240) compared to the smooth (assumed flat surface) of the model. The remaining 240 data points pertain to the lower receiver.

The uncertainties associated with the four parameters of interest are shown in Fig. 16. The minimum source–receiver offset (range) for this leg was about $4 \pm 0.1$ m, with an uncertainty that increases with increasing range. The resulting uncertainties in the seabed angle estimation are shown in the top plot, and are about $1^\circ$ or less.

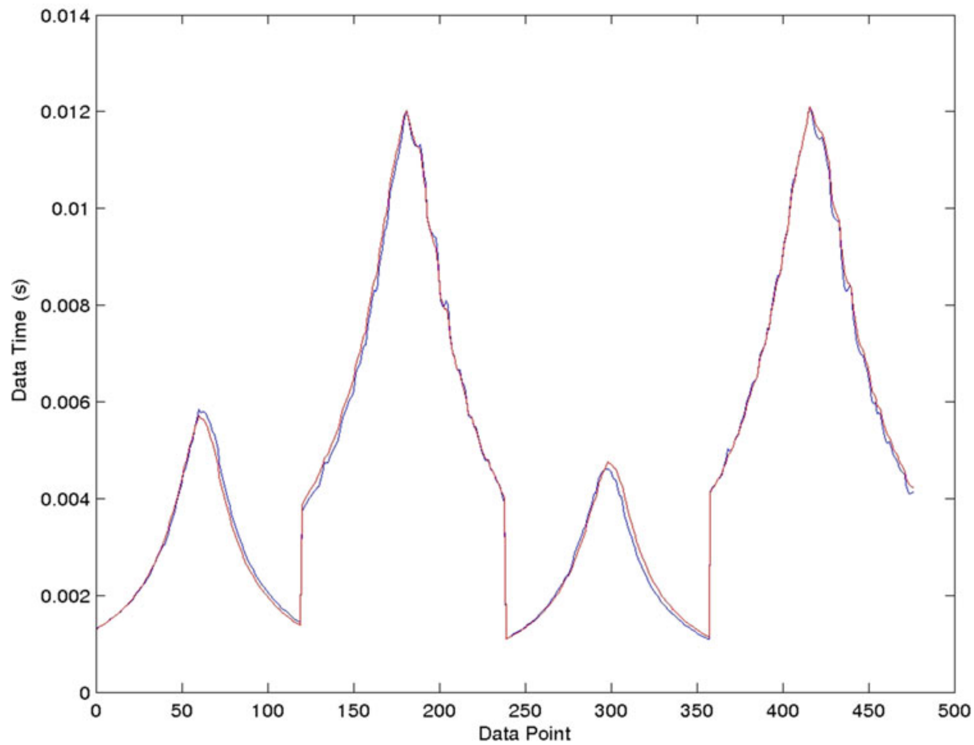


Fig. 15. Relative travel times for the direct-bottom and direct-sea surface paths for the measured data (blue) and the fits (red) using a ray-based inversion.

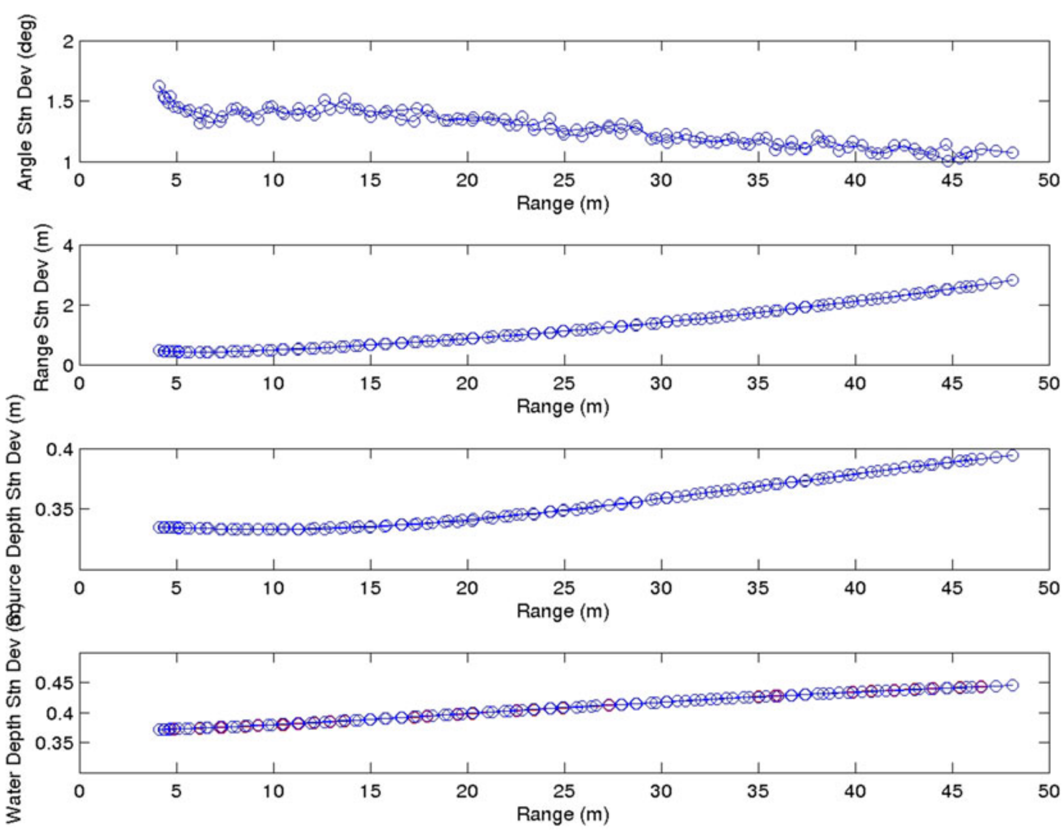


Fig. 16. Uncertainty estimates for the parameters of interest from the ray-based relative travel-time inversions (data fits shown in Fig. 15).

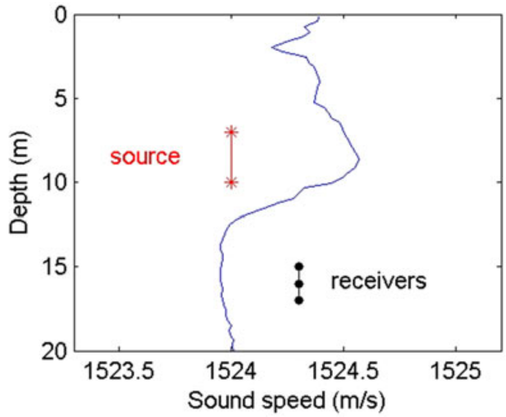


Fig. 17. Sound speed profile on May 5 with the range of source and receiver depths indicated.

The sound speed profiles were nearly isospeed (an example is shown in Fig. 17), though refraction was not negligible in estimating the experiment geometry. Refraction effects were included in the ray-based Bayesian estimation. The Bayesian estimates of the source–receiver geometry were compared with independent measurements by computing source tow speed, $v$

$$v = \frac{|r_j - r_{j-1}|}{\eta \cos\theta} \tag{2}$$

where $r_j$ are the estimated source–receiver offset ranges, $\eta$ is the pulse repetition rate (in seconds), and $\theta$ is the angle in the horizontal between the tow radial and the receiver

$$\sin\theta = \frac{\min|r_j|}{r_j}. \tag{3}$$

The ray-based travel-time Bayesian inversion tow speed estimates were compared with those from a catamaran-mounted GPS, and from relative-velocity estimation using the Doppler cross-power spectral phase [12] as well as the traditional ambiguity function approach, see Fig. 18. The latter three methods are sampled at the pulse repetition rate, 0.5 s, whereas the GPS data are sampled at 5 s. The source–receiver depth difference estimated from the ray-based inversion results was used to convert relative velocities to tow speed.

The instantaneous source tow speed is a function of the ship speed (slowly varying) and the dynamics of the coupled catamaran-suspended source system moving over passing waves. Visual observations showed that the catamaran sped up when advancing down a front of a wave crest, then slowed near the trough. These fluctuations in the speed are not captured in the slowly sampled GPS data, but are captured in the other three methods, see Fig. 18. While the non-GPS methods give similar results, some differences/errors are evidence. The Doppler formula appears to underestimate the speed for transmissions 4 and 5 and perhaps 113 and 116. The ambiguity function method greatly overestimates the speed for transmission 8–13, 17, and 31. The relative travel-time inversion (Bayesian) appears robust at far ranges (small and large transmission numbers), but has two errors near CPA, which is at transmission 62. In summary, all three methods follow the GPS data reasonably well. The ray-based travel-time inversion (Bayesian) results indicate the methodology for estimating source and receiver depths and range is robust except near CPA.

## Appendix II

### A. Seabed Interface Roughness Power Spectrum Estimate

Roughness power spectra were estimated using multibeam bathymetry collected by de Moustier and Kraft [20], and laser line scanner measurements collected by Hefner *et al.* [19]. In both cases, roughness measurements exist as 2-D digital elevation maps (DEMs). 1-D marginal roughness power spectra are obtained by removing a linear trend in a particular direction, applying a Hann window, performing a fast Fourier transform, and incoherently averaging in the orthogonal direction. Power spectra are normalized such that the windowing processes preserves the root mean square roughness of the original measurement.

The multibeam bathymetry estimates have a spatial resolution of 1 m $\times$ 1 m and are known to have minor residual noise from tides. Data used to estimate power spectra were confined to a square with a side length of 750 m centered at the swale site. The square was oriented such that its sides were either perpendicular or parallel to the ridge-swale crests. Marginal spectra were obtained by taking Fourier transforms both along and across the crest principle directions. Laser line scan measurements were taken near the swale site and have spatial resolution of 1 mm $\times$ 1 mm. The laser scanner was not outfitted with a compass, so the precise direction of the power spectrum estimates is unknown. Laser scanner spectra are also averaged over independent locations, as 2-D DEMs were measured at multiple locations near the swale site.

Results for marginal spectra are displayed in Fig. 19 as a function of spatial wavenumber in rad/m. Spectra are shown from multibeam bathymetry across and along the crest directions, which cover the low-wavenumber regime, as well as the spectra from the line scan measurements, which cover the high-wavenumber regime. For the multibeam spectra, attention is restricted to the wavenumber region above $2\pi$/10 m, which is approximately the scale corresponding to the largest Fresnel zone in the reflection measurements. The highest wavenumber portion of multibeam roughness spectra is not shown because it is subject to processing artifacts. For the spectrum derived from the laser scanner, attention is restricted to wavenumbers below 1100 rad/m. Above this wavenumber, the spectrum appears to be contaminated by noise.

A model power spectrum of the form $W(K) = w_1 / K^{\gamma_1}$ was fit to the measured data, where $K$ is the wavenumber magnitude, $w_1$ is the spectral strength, and $\gamma_1$ is the spectral slope. Model parameters were fit to multibeam and line scanner data independently, and by using both spectra together. Parameters were estimated using linear least-squares in log-log space, and can be found in Table V. The model fits are displayed as dashed and dotted lines in Fig. 19. Visually, fits to the multibeam and laser scanner spectra are quite consistent with one another and appear to form a continuous power-law spanning over three orders of magnitude. Numerically, estimates of the model parameters are

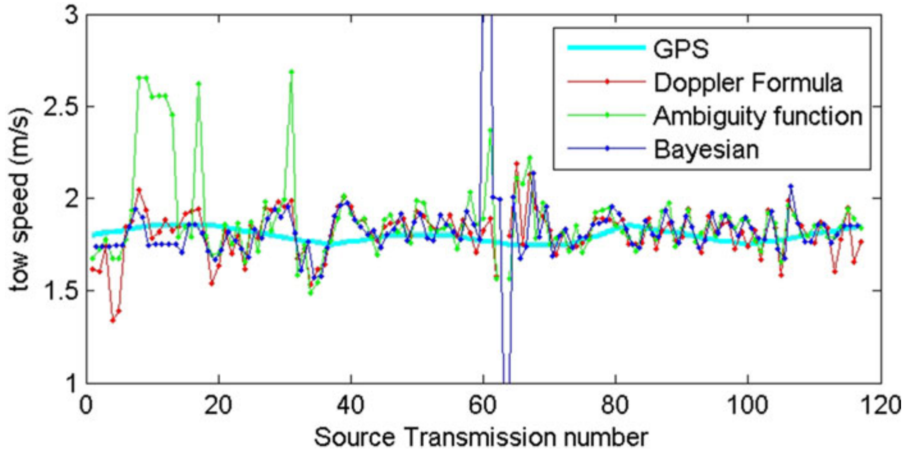


Fig. 18. Comparison of ray-based travel time geometry estimates (Bayesian) converted to ship speed Eq. (2) with other measurements, including GPS (every 5 s), and Doppler estimation using a newly derived formula [12] (every 0.5 s) and the traditional ambiguity function method. The CPA is at transmission 62.

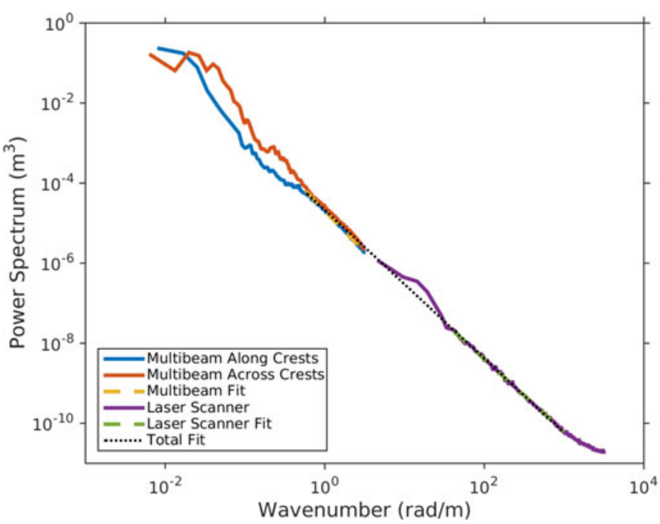


Fig. 19. Spectra of multibeam data [20] and APL-UW laser line scanner data [19] with fits.

TABLE V
MODEL PARAMETERS ESTIMATED FROM MEASURED ROUGHNESS SPECTRA FROM MULTIBEAM BATHYMETRY AND LASER LINE SCANNER DATA SCANNER IGNORING THE LOW WAVENUMBERS FROM BOTH DATA SETS

| Data Source | 1-D spectral strength $\boldsymbol{w}_1$ $(m^4)$ | 1-D spectral exponent $\gamma_1$ |
|---|---|---|
| Multibeam | $2.04 \times 10^{-5}$ | 1.98 |
| Laser line scanner | $2.27 \times 10^{-5}$ | 1.86 |
| Total | $2.12 \times 10^{-5}$ | 1.85 |

very similar, although they exhibit slight discrepancies between the multibeam and line scanner measurements.

The multibeam-derived spectral parameters used in the text have Gaussian distributed interface slopes with a standard deviation of about 14°. The slope distribution is independent of the spectral cutoff values employed here, i.e., the slope distribution is dominated by the high-spatial wavenumbers. In this case (relatively small $\gamma$), the slopes depend somewhat on the discretization. The modeling in this paper samples the boundary at 30 points per (acoustic) wavelength, thus, the 14° slopes are higher than a more typical sampling of 10 points per wavelength. Nevertheless, the 14° slopes do not seem unrealistic.

## ACKNOWLEDGMENT

The authors would like to thank the Canadian Forces Auxiliary Vessel (CFAV) *Quest* captain, crew, and especially the Engineering Coordinator J. Scrutton who helped solve a number of challenging ocean engineering challenges and the captain who skillfully managed the navigation at very low speeds. C. W. Holland would like to thank J. Goff for helpful discussions about the geology of the area and helpful discussions with T. Hefner, DJ Tang, and C. de Moustier. The authors would also like to thank the Office of Naval Research Ocean Acoustics program for their support of this work and the collaborative opportunities it presented.

## REFERENCES


[1] F. Jensen, W. A. Kuperman, M. B. Porter, and H. Schmidt, *Computational Ocean Acoustics*, 2nd ed. New York, NY, USA: Springer-Verlag, 2011, Sec. 2.4.3, p. 93.

[2] D. R. Jackson, R. I. Odom, M. L. Boyd, and A. N. Ivakin, "A geoacoustic bottom interaction model (GABIM)," *IEEE J. Ocean. Eng.*, vol. 35, no. 3, pp. 603–617, Jul. 2010.

[3] C. W. Holland and J. Dettmer, "In-situ sediment dispersion estimates in the presence of discrete layers and gradients," *J. Acoust. Soc. Amer.*, vol. 133, pp. 50–61, 2013.

[4] C. W. Holland, P. L. Nielsen, J. Dettmer, and S. E. Dosso, "Resolving meso-scale seabed variability using reflection measurements from an autonomous underwater vehicle," *J. Acoust. Soc. Amer.*, vol. 131, pp. 1066–1078, 2012.

[5] C. W. Holland and J. Osler, "High resolution geoacoustic inversion in shallow water: A joint time and frequency domain technique," *J. Acoust. Soc. Amer.*, vol. 107, pp. 1263–1279, 2000.

[6] J. Dettmer, S. E. Dosso, and C. W. Holland, "Trans-dimensional geoacoustic inversion," *J. Acoust. Soc. Amer.*, vol. 128, pp. 3393–3405, 2011.

[7] C. W. Holland, J. Dettmer, and S. E. Dosso, "Remote sensing of sediment density and velocity gradients in the transition layer," *J. Acoust. Soc. Amer.*, vol. 118, pp. 163–177, 2005.

[8] J. Dettmer, C. W. Holland, and S. E. Dosso, "Resolving lateral seabed variability by Bayesian inference of seabed reflection inversions," *J. Acoust. Soc. Amer.*, vol. 126, pp. 56–69, 2009.

[9] J. A. Goff, "Seismic and core investigation off Panama city, Florida, reveals sand ridge influence on formation of the shoreface ravinement," *Continental Shelf Res.*, vol. 88 , pp. 34–46, 2014.

[10] J. Goff, Unpublished notes from a seismic reflection and coring campaign along the main reverberation line.

[11] C. W. Holland, "Seabed reflection measurement uncertainty," *J. Acoust. Soc. Amer.*, vol. 114, pp. 1861–1873, 2003.

[12] S. Pinson and C. W. Holland, "Relative velocity measurement from the spectral phase of a match-filtered linear frequency modulated pulse (EL)," *J. Acoust. Soc. Amer.*, vol. 140, pp. 191–196, 2016.

[13] R. T. Bachman, "Acoustic and physical property relationships in marine sediment," *J. Acoust. Soc. Amer.*, vol. 78, pp. 616–621, 1985.

[14] J. Dettmer, S. E. Dosso, and C. W. Holland, "Model selection and Bayesian inference for high resolution seabed reflection inversion," *J. Acoust. Soc. Amer.*, vol. 125, pp. 706–716, 2009.

[15] S. Pinson, J. Cordioli and L. Guillon, "Spherical wave reflection in layered media with rough interfaces: Three dimensional modeling," *J. Acoust. Soc. Amer.*, vol. 140, pp. 1108–1115, 2016.

[16] C. A. Langston, "The effect of planar dipping structure on source and receiver responses for constant ray parameter," *Bull. Seismological Soc. Amer.*, vol. 67, no. 4, pp. 1029–1050, 1977.

[17] E. Bossy, "SimSonic suite user's guide for SimSonic2D," 2012. [Online]. Available: http://www.simsonic.fr/(07/30/2013)

[18] T. Hefner and D. J. Tang, "Seafloor laser scanner measurements at TREX13."

[19] M. Vercammen, "The reflection of sound by curved surfaces," in *Proc. Acoust.*, Paris, France, 2008, pp. 3473–3478.

[20] C. de Moustier and B. J. Kraft, "Bathymetry and 400-kHz seafloor acoustic backscatter imagery offshore," Panama City Beach, FL, USA.

[21] S. E. Dosso and G. R. Ebbeson, "Array element localization accuracy and survey design," *Can. Acoust.*, vol. 34, pp. 3–14, 2006.


**Charles W. Holland** received the B.S. degree in engineering from the University of Hartford, West Hartford, CT, USA, in 1983 and the M.S. and Ph.D. degrees in acoustics from the Pennsylvania State University, State College, PA, USA, in 1985 and 1991, respectively. His Ph.D. dissertation addressed acoustic propagation through and interface waves in poro-viscoelastic marine sediments.

From 1985 to 1996, he conducted research in sediment acoustic modeling and seafloor classification techniques at Planning Systems, Inc. In 1996, he joined the NATO Undersea Research Centre, La Spezia, Italy, where he developed seabed reflection and scattering measurement and parameter estimation techniques. In 2001, he joined the Applied Research Laboratory at the Pennsylvania State University where he continues his research in both theoretical and experimental aspects of ocean waveguide and seafloor acoustics.

Dr. Holland is a Fellow of the Acoustical Society of America.

**Samuel Pinson** received the Engineer's degree in acoustics and vibration from ENSIM, Le Mans, France, in 2007, the M.S. degree in mechanics and acoustics from the Universié du Maine, Le Mans, France, in 20017, and the Ph.D. degree in underwater acoustics from the Université de Bretagne Occidentale, Brest, France, in 2011.

In summer 2012, he was a Visiting Researcher at the Center for Maritime Research and Experimentation, La Spezia, Italy. Between 2012 and 2013, he was a Postdoctoral Researcher at the Applied Research Laboratory of the Pennsylvania State University, State College, PA, USA. Between 2014 and 2016, he was a Postdoctoral Researcher at the Universidade Federal de Santa Catarina, Floriaónopolis, Brazil. His research interests include wave propagation in complex media and signal processing.

**Chad M. Smith** (M'09) received the B.S. degree in electrical engineering technology from the Pennsylvania College of Technology, Williamsport, PA, USA, in 2006 and the M.S. degree in acoustics from The Pennsylvania State University, University Park, PA, USA, in 2010, where he is currently working toward the Ph.D. degree in acoustics.

He is a Senior Research Assistant for the Applied Research Laboratory, The Pennsylvania State University. From 2008 to 2010, he was a Graduate Research Assistant for the Applied Research Laboratory, The Pennsylvania State University. From 2006 to 2008, he was an Electrical Engineer for QorTek, Inc., Williamsport, PA, USA. His research interests include underwater and atmospheric acoustic propagation, array and transducer technology, and signal processing.

Mr. Smith is a member of the Acoustical Society of America.

**Paul C. Hines** received the B.Sc. degree (honors) in engineering-physics from Dalhousie University, Halifax, NS, Canada, in 1981 and the Ph.D. degree in physics from the University of Bath, Bath, U.K., in 1988.

He joined Defence R&D Canada, Dartmouth, NS, Canada, in 1981. His research on acoustic scattering from ocean boundaries earned him the Chesterman Medal from the University for "Outstanding Research in Physics." From his return to DRDC in 1988 until his departure in March 2014, he led several groups and managed a variety of acoustic research projects for both DRDC and the US Office of Naval Research. He is a Seasoned Experimentalist and has been the Chief Scientist for several collaborative international research trials. He is currently the President of Hines Ocean S&T, Inc., in addition to conducting research in the Department of Electrical and Computer Engineering and Department of Oceanography, Dalhousie University, Halifax, NS, Canada. During his career, he has conducted research in antisubmarine warfare, mine and torpedo countermeasures, rapid environmental assessment, acoustic scattering, sound-speed dispersion, vector sensor processing, sonar classification and tracking, continuous active sonar, and the application of aural perception in humans, to target classification in sonar.

Dr. Hines is a Fellow of the Acoustical Society of America, and a Distinguished Lecturer of the IEEE Ocean Engineering Society.

**Derek R. Olson** received the A.B. degree (*cum laude*) in physics from Vassar College, Poughkeepsie, NY, USA, in 2009 and the Ph.D. degree in acoustics from The Pennsylvania State University, University Park, PA, USA, in 2014.

He is currently a Research Associate at the Applied Research Laboratory, The Pennsylvania State University. He was a National Defense Science and Engineering Graduate Fellow. His research concerns theoretical, numerical, and experimental investigation of acoustical scattering from ocean boundaries.

Dr. Olson is a member of the Acoustical Society of America, the IEEE Oceanic Engineering Society, Phi Beta Kappa, and Sigma Xi.

**Stan E. Dosso** received the B.Sc. degree in physics and applied mathematics and the M.Sc. degree in physics from the University of Victoria, Victoria, BC, Canada, in 1982 and 1985, respectively, and the Ph.D. degree in geophysics from the University of British Columbia, Vancouver, BC, Canada, in 1990.

From 1990 to 1995, he was in Ocean Physics (Arctic Acoustics) at the Defence Research Establishment Pacific, Victoria, BC, Canada. In 1995, he was appointed to an Ocean Acoustics Research Chair in the School of Earth and Ocean Sciences, University of Victoria, where he is currently a Professor and the Director of the School. His research interests involve probabilistic inverse problems in ocean acoustics and geophysics.

Dr. Dosso is a Fellow of the Acoustical Society of America and a member of the Canadian Acoustical Association (President 2003–2007) and the American Geophysical Union.

**Jan Dettmer** received the Diplom Geophysiker degree in geophysics from the University of Hamburg, Hamburg, Germany, in 2002 and the Ph.D. degree in earth and ocean science from the University of Victoria, Victoria, BC, Canada, in 2007.

He was with the Office of Naval Research and a Postdoctoral Fellow in 2007 and 2008, a Research Scientist at the University of Victoria from 2009 to 2013, and a Research Fellow at Australian National University from 2013 to 2016. Since 2016, he has been an Assistant Professor of Geophysics at the University of Calgary, Calgary, AB, Canada. His research interests include seismology and acoustics, in particular earthquake sources, earth structure, seabed structure, inverse problems, and uncertainty quantification.

# ATTACHMENT 4

# SCEX 2017
# Experimental Trip Report

Submitted to: Dr. Robert Headrick
Date: April 12, 2017
Grant Title: Analysis of Spatiotemporal Clutter Statistics and Support of the Five Octave Research Array
Grant #: N00014-16-1-2561

Written by: Mr. Chad Smith
The Pennsylvania State University
Applied Research Laboratory
State College, PA 16801

## Table of Contents

## Summary

This report provides a brief summary of the efforts of the Penn State Applied Research Laboratory (PSU-ARL) Five Octave Research Array (FORA) team during the recently concluded Seabed Characterization Experiment (SCEX). This work took place aboard the R/V Neil Armstrong, roughly 70 miles south of Woods Hole Oceanographic Institution near the coordinates 40° 28'N latitude and 70° 35'W longitude. The primary goals of SCEX were related to research towards understanding the effects of an acoustically muddy (soundspeed less than that of seawater) water-sediment interface on acoustic propagation and geoacoustic inversion. It is the hope of the researchers involved that this region's water-sediment interface is dominated by an acoustically muddy layer. The experimental work discussed in this document took place between March 23rd and April 6th of 2017, and includes participation in SCEX using the ONR FORA acquisition system as well as other experimental equipment including a towed coherent source, towed impulsive source, and several moored acquisition system deployments. Measurements were made in a variety of geometries advantageous for wide-angle geoacoustic inversion techniques developed by Charles Holland, the Chief Scientist of the R/V Neil Armstrong for this cruise. In total, acoustic data was collected by the PSU-ARL team for 6 days using a combination of the cardioid aperture of the FORA and various autonomous data logging systems for a combined total of about 900 GB of raw hydrophone data. The FORA team consisted of lead FORA technician Jim Dorminy, engineer Zack Lowe, and researcher Chad Smith. Early analysis has shown data from FORA measurements as well as other acoustic recorder deployments is of high quality.

The first two days of this trial proved challenging for PSU-ARL due to a combination of a damaged cable connection on the FORA tow cable in addition to a fiber hub within the FORA data acquisition rack which was operating intermittently (both assumedly due to shipping and transport). Unfortunately, these two separate acquisition system faults each manifested themselves as communication line errors causing this FORA malfunction to be particularly challenging to diagnose. Fortunately, Charles Holland and the science party as a whole was able to rearrange the data acquisition schedule in order to efficiently utilize the downtime of the FORA system and not waste valuable measurement time. After the FORA team was able to localize and repair each fault, the FORA system was used in full capacity as weather and marine mammal siting's permitted in configurations never before used. A lightweight (~15 lb) coherent source was attached to the FORA forward VIM in order to increase the angular aperture available for wide-angle reflection measurements. Additionally, autonomous acoustic recorders were attached to the forward VIM and drogue for the same purpose. Although time consuming during deployment/recovery (due to the placement and removal of the source, cabling, and recorders for each deployment) this arrangement proved to tow stably and in addition to providing wide-angle measurements appeared to greatly limit the roll of the array (an important note for future work as the roll stability of the cardioid system directly effects processing). As a final interesting highlight of FORA measurements during SCEX, the FORA team was able to do an absolute timing analysis of the FORA acquisition system during this work. Due to engineer Zack Lowe's development of an accurately GPS sync'd coherent transmit system and the marrying of the source and FORA tow cables, transmit system crosstalk could be used to verify the absolute accuracy of

the FORA. It is important to note that this crosstalk did not degrade geoacoustic measurements since it is both low in amplitude and easily time-gated out of analysis.

In addition to measurements using the FORA system, for this particular cruise the FORA team was also tasked with preparation and operations of two source systems (one coherent and one impulsive) and several mooring configurations used to deploy autonomous hydrophones near the seafloor. As previously discussed, the coherent source was physically attached to the FORA VIM with the cabling married with the FORA tow cable. The impulsive source was towed behind the ship on a pontoon platform. Both of these systems performed well throughout the cruise. The moorings designed by PSU-ARL incorporated soundspeed and depth recordings in addition to acoustic recordings for wide-angle reflection measurements. Mooring deployments and measurements also went well aside from weather and marine mammal related delays.

Charles Holland will be submitting a more thorough cruise report incorporating the operations aboard the R/V Armstrong, while this document briefly outlines the specific experimental work addressed by the FORA team during the SCEX trial. This trial was a wonderful collaboration between very capable research teams. PSU-ARL is very thankful to have been involved with this work!

## Experimental Operations and Data Collection

### FORA Data Collection

Figure 1 displays the two chief configurations in which the FORA acquisition system was used during SCEX. The port configuration was used in order to incorporate wide-angle measurements using moored autonomous hydrophones on days when sea state did not permit the use of the towed impulsive source (boomer system, shown during deployment in Figure 10, Appendix A). The right figure is was typical configuration used with FORA to cover large measurement tracks. Both of these configurations had a coherent source attached to the FORA VIM and the source cable married with the FORA tow cable. Although the process of attaching the source and marrying its cable to the tow cable creates longer deployment and recovery times, this configuration gave the angular geometries necessary for this work and towed surprisingly stable at 3.5-4.5 knots. Roll for both the forward and aft roll sensors varied less than ±5° during most measurements.

An additional positive note of the married FORA/source configuration was that it allowed an accurate timing assessment of the FORA acquisition system. The transmit system designed for this experiment by engineer Zack Lowe is accurately GPS time sync'd, while the married cable configuration caused crosstalk to be recorded on the FORA system at the onset of each pulse transmitted. Generally crosstalk is a non-desired phenomena during measurements, in this case however, the crosstalk does not degrade data quality and can be used to accurately verify absolute FORA timing (a question that has been encountered during past experiments). Timing analysis will be discussed in the Early Analysis Highlights section.

Autonomous hydrophones were also attached to the FORA VIM and drogue (one on each) during several deployments in order to further increase the available angular measurement aperture. Like the source, these deployments did not seem to have any negative effect on the stability of the FORA array at normal tow speeds (3.5-4.5 knots). Figure 7 (Appendix A) shows the FORA's home at the aft-port of R/V Armstrong while Figure 8 (Appendix A) displays the attachment location of one of the autonomous recorders deployed on the FORA VIM.

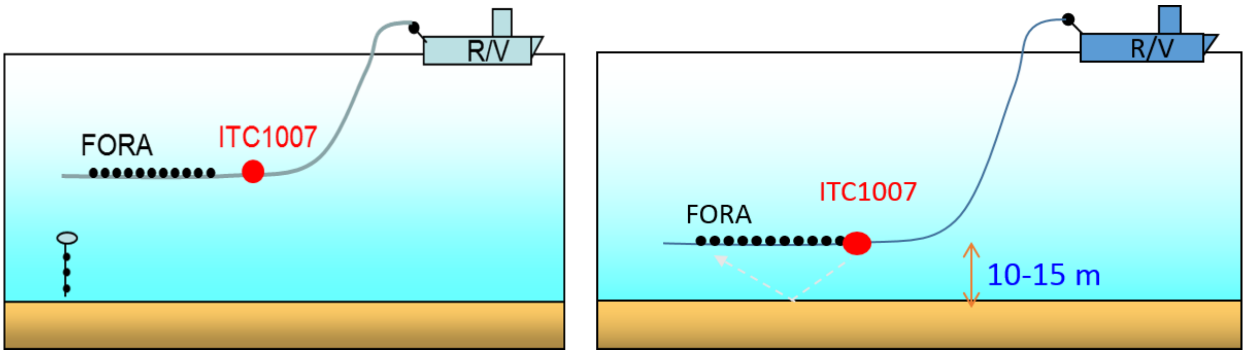


*Figure 1: FORA measurement schemes used during SCEX. The port schematic was used in order to incorporate wide-angle measurements using stationary moorings on days when sea state did not permit the use of the towed boomer system. The right figure is a typical configuration used with FORA to cover large measurement tracks. (figures created by Charles Holland)*

**Boomer Data Collection**

Figure 2 shows a basic schematic of wide-angle measurements made using the impulsive source or boomer system and moorings with autonomous hydrophones and environmental data recorders. These measurements did not use the FORA acquisition system. Figure 9 (Appendix A) shows an example of one configuration of these moorings prior to deployment while Figure 10 (Appendix A) shows the impulsive source pontoon during deployment. Although this particular measurement required the lowest sea state and nicest weather of PSU measurements during SCEX, this system was deployed twice and early data analysis by Charles Holland show high quality and highly interesting data.

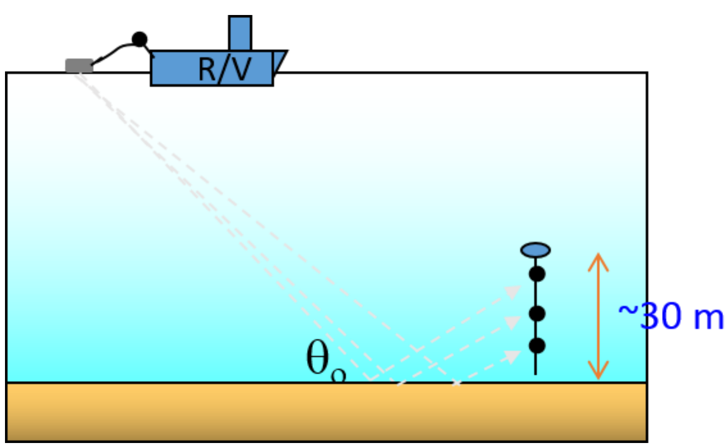


*Figure 2: Schematic of wide-angle reflection measurements using a towed boomer system and moored autonomous hydrophones. (figures created by Charles Holland)*

### Performance of FORA Winch

During the Littoral Continuous Active Sonar (LCAS) experiment of 2015 it became apparent that the FORA winch system must be completely overhauled. During 2016, PSU-ARL contracted Electric Motor & Supply (EMS) in Altoona, PA to complete a full system overhaul of the winch control cabinet and Breon's Inc. of Pleasant Gap, PA to overhaul the 440V, 3-phase winch motor system. These companies overhauled the winch motor and completely rewired the motor control cabinet electrical system including electrical and hydraulic safety switches. They also verified proper operation of the hydraulic system. Speaking to the work of these companies, the FORA winch system performed flawlessly throughout the SCEX17 experiment.

## Early Analysis Highlights

### Data Quality of FORA Measurements

FORA data recordings went well throughout the experiment without a single data packet lost during the entire experiment (the FORA acquisition system uses asynchronous UDP for data communications). Early analysis shows the data to be of high quality and without excessive in-band noise due to ship- or system-noise. Figure 4 shows an example of match filtered FORA data for a single phone in fast-time verses slow-time for consecutive pulses. Fast-time (y-axis) is shown in milliseconds from transmit and slow-time (x-axis) is converted to ship travel using nominal tow speed and pulse spacing. This figure gives a rough look at the complexity of the seafloor subsurface using a single phone. The consistent arrival near 30mS is the arrival of the specular water-sediment return (~42°). The light arrival near 43mS may be a subsurface interface. Much analysis is needed, but early data evaluations such as this allowed PSU to verify satisfactory data quality during experimental execution. Figure 4 shows the geographic description of the mudbase in this region base on prior surveys, the black X in this figure shows the measurement location of the data displayed in Figure 3.

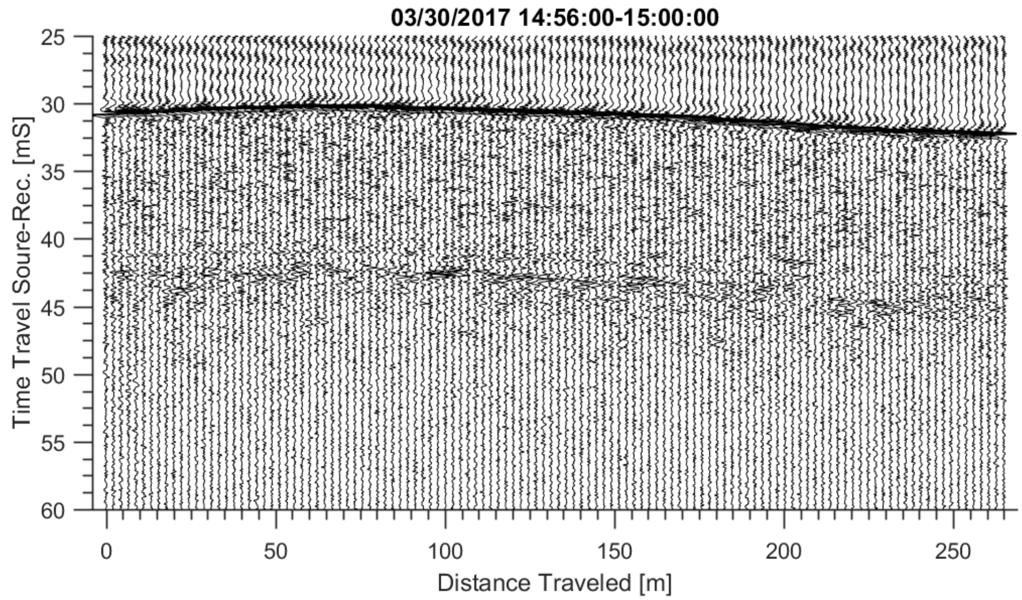


*Figure 3: Example of early analysis using match filtered FORA data. This figure is a fast-time verse slow-time plot of consecutive pulses for a single FORA hydrophone. Fast-time (y-axis) is shown in milliseconds from transmit and slow-time (x-axis) is converted to ship travel using nominal tow speed and pulse spacing. This figure gives a rough look at the complexity of the seafloor subsurface using a single phone. The consistent arrival near 30 mS is the arrival of the specular water-sediment return (~42°). The light arrival near 43mS may be a subsurface interface.*

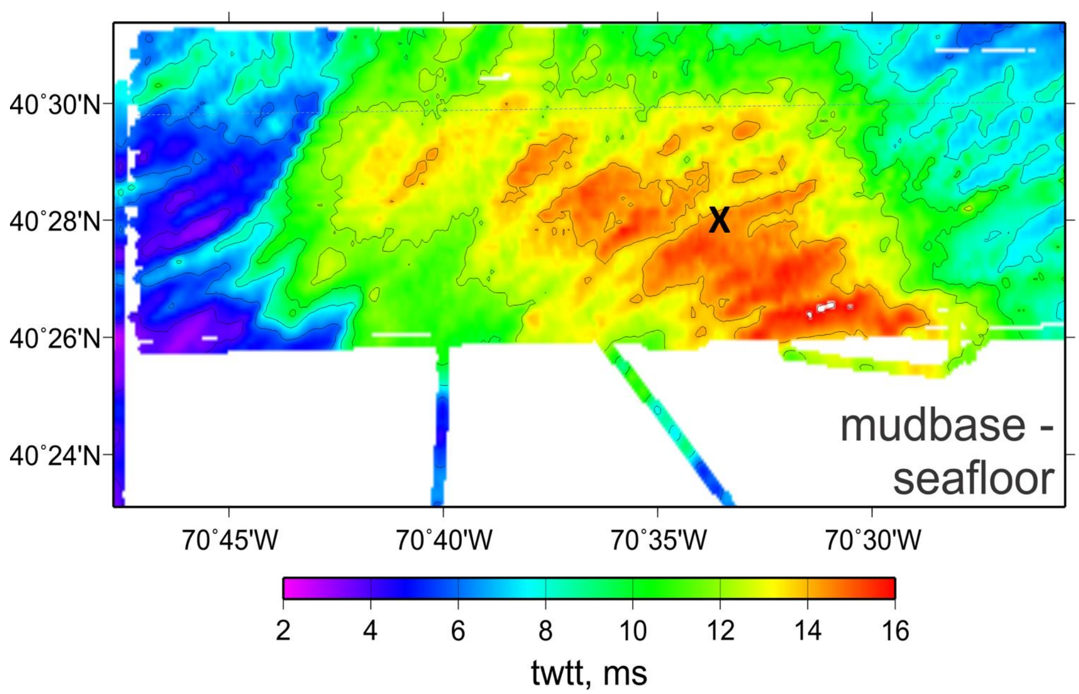


*Figure 3: Geographic description of mudbase in this region base on prior surveys. Black X shows the measurement location of the data displayed in Figure 3.*

## Absolute Timing Analysis

During this experiment PSU-ARL had responsibility of operation of the FORA and design and operation of a coherent source system which was deployed upon the FORA VIM with the source cable married to the FORA tow cable. Resources were committed to properly designing a transmit system with accurate absolute GPS timing. Because of this time-accurate transmit system, it was possible to analyze the absolute accuracy of the FORA system using the crosstalk recorded by all phones on the FORA system when each pulse was transmitted. It is important to mention that this advantaged was gained without sacrificing the data quality of FORA data since this crosstalk is easily time-windowed out of geoacoustic analysis.

The transmit system used for SCEX17 is based on National Instruments Multi-device Clock Disciplining software. Combined with the correct hardware (PXI-6683H GPS Card, PXIe-6674T Timing Card, and a PXIe-1082 Chassis), this software allows a 10MHz backplane chassis clock to be disciplined to GPS time. COTS LabVIEW drivers are used to check for an accurate timing source (PXI-6683H GPS) and command the hardware to discipline the oven-controlled crystal oscillator (OCXO on the PXIe-6674T). Once locked, the transmit system is ready to be used, and the offset between the 10MHz clock and the reference can be monitored. During testing the offset was observed to be within +/-20ns. This is the time-accuracy of the coherent source system during FORA measurements during SCEX17 and this provides and valid reference to compare the FORA acquisition clock to.

Timing analysis of the TX/FORA data found a small, consistent time offset between the transmit system and the FORA acquisition system. This offset is, on average, a positive offset of 2.69mS and causes the initial arrival of the source direct blast to appear 2.69mS early. However, due to the very consistent nature of this time offset it is simple to correct for and this analysis has given a well calibrated look at the absolute temporal accuracy of the FORA system. Figure 5 provides an example of the time difference (y-axis) of each transmitted pulse from the FORA recorded time verse recording time (x-axis). The quickly noted discretized nature of this figure is due to the 12.5kHz FORA sampling rate, while the negative sloped trend of the data is due to FORA clock slew. This figure shows that while the FORA clocking system does have jitter and slew, it is continually correcting itself so as to always be within ±200nS of the source time. Adding the source system's timing uncertainty of 20nS with the FORA's gives a total system uncertainty of ±220nS for this work as well as a good estimate for previous work using only the cardioid array section (see Appendix B) of the acquisition system. Figure 6 shows histograms of this timing offset for data prior to correction of the 2.69mS (top) and after (bottom).

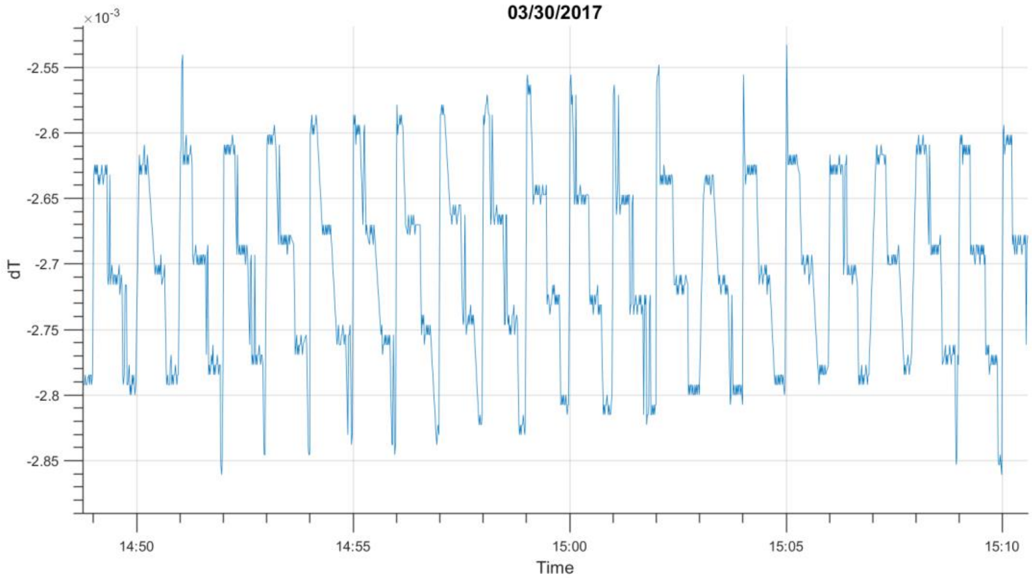


*Figure 4: Example of the time offset of FORA measurements referenced to the TX system, verse time. The transmit system is accurate to GPS time within ±20nS. Because of this, the crosstalk between the source cable and the FORA cable can be used to investigate the absolute timing offset of the FORA data collection system. This provides and accurate way to estimate the absolute FORA system timing without error from the propagation path and physical system dynamics.*

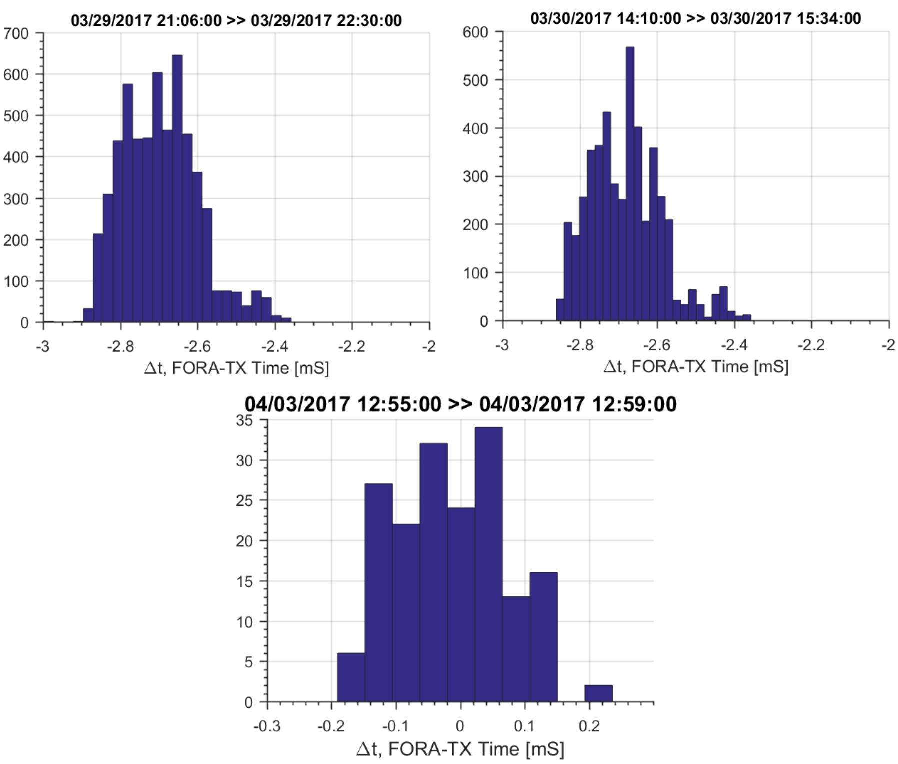


*Figure 5: Histograms of the timing offset for individual pulses referenced to the transmit system. The upper figures are non-time-corrected examples from data taken near the beginning of the experiment while the lower figure shows the histogram of the time offset after being corrected using the offset found in previous data. This analysis shows that the FORA system is keeping proper absolute time within ±220nS but has a relative offset of 2.67mS.*

## Looking Forward

The FORA system is currently in a fully operational state, however, one cable termination should be made more robust prior to any future experiments using the FORA acquisition system.

## Conclusions

The FORA team had a rough start to the SCEX17 experiment but managed to troubleshoot FORA and repair the system in a timely manner and complete the measurements required for this trial. Additionally, PSU-ARL provided much additional support of Charles Holland's experimental goals, acquiring and operating specialized source and mooring equipment for this effort. In total, acoustic data was collected by the team for 6 days using a combination of the cardioid aperture of the FORA and various autonomous data logging systems for a combined total of about 900 GB of raw hydrophone data in the interest of geoacoustic inversion research. This trial was a wonderful collaboration with many very capable research teams. PSU-ARL is thankful to have been involved with this work!

## Acknowledgements

Many thanks to the crew of the R/V Armstrong. Without their very experienced help this work could not have been realized. Additionally, a special thank you to the R/V Armstrong SSSG Joe Futrelle who went above and beyond in assisting the FORA team with fiber repairs and helped save valuable measurement time.

## Appendix A: Operational Figures

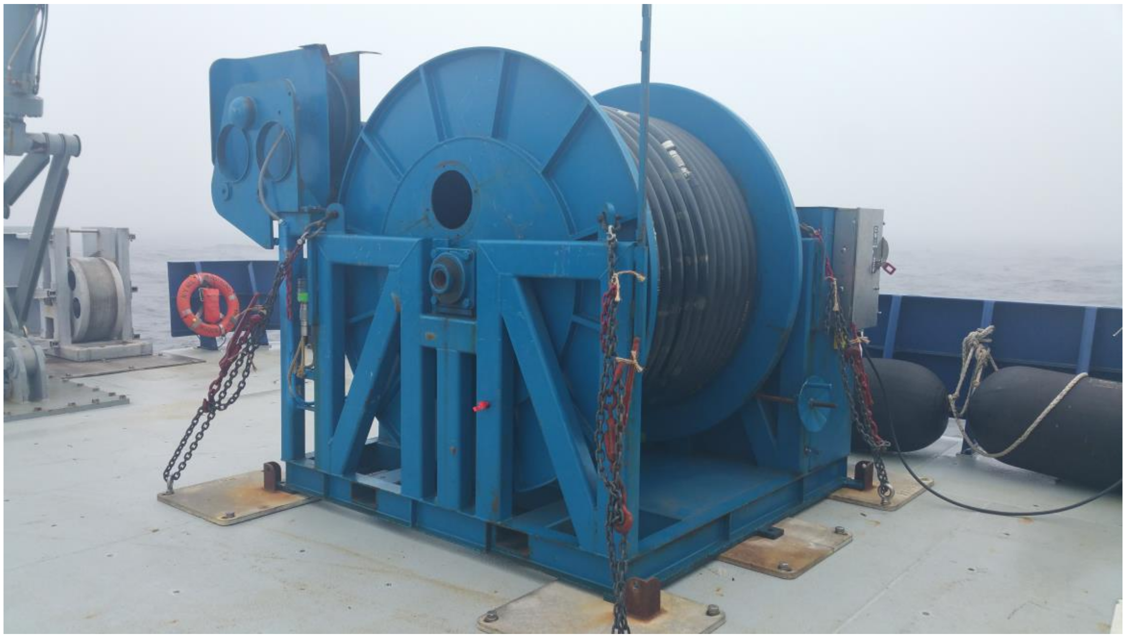

*Figure 6: FORA found a home at the aft-port of the Armstrong.*

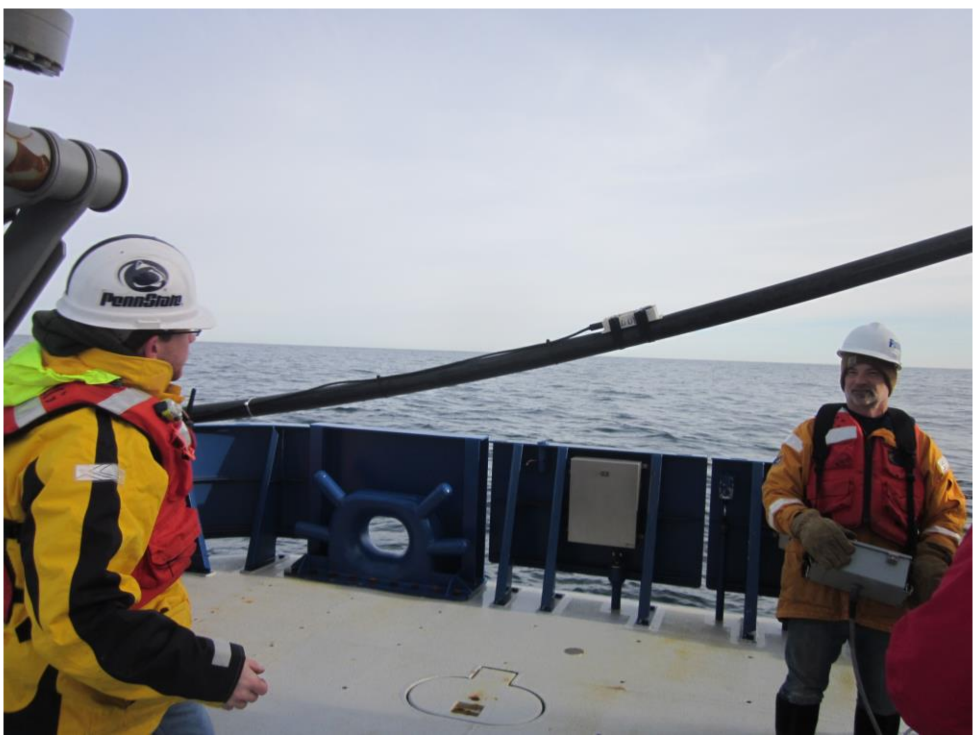


*Figure 7: Example of attaching an autonomous recording system (in this case a DSGmini) to the FORA VIM to increase the azimuthal aperture for Charles Holland's geoacoustic inversion research.*

*Figure 8: One of the subsurface moorings used in this work just prior to deployment. These moorings were purposefully designed as light (referring to the line and chain, etc.)  as possible in an attempt to minimize the acoustic influence for single bounce reflection measurements. These moorings contained autonomous hydrophones and temperature/pressure in addition to the required acoustic release and short-baseline homing systems.*

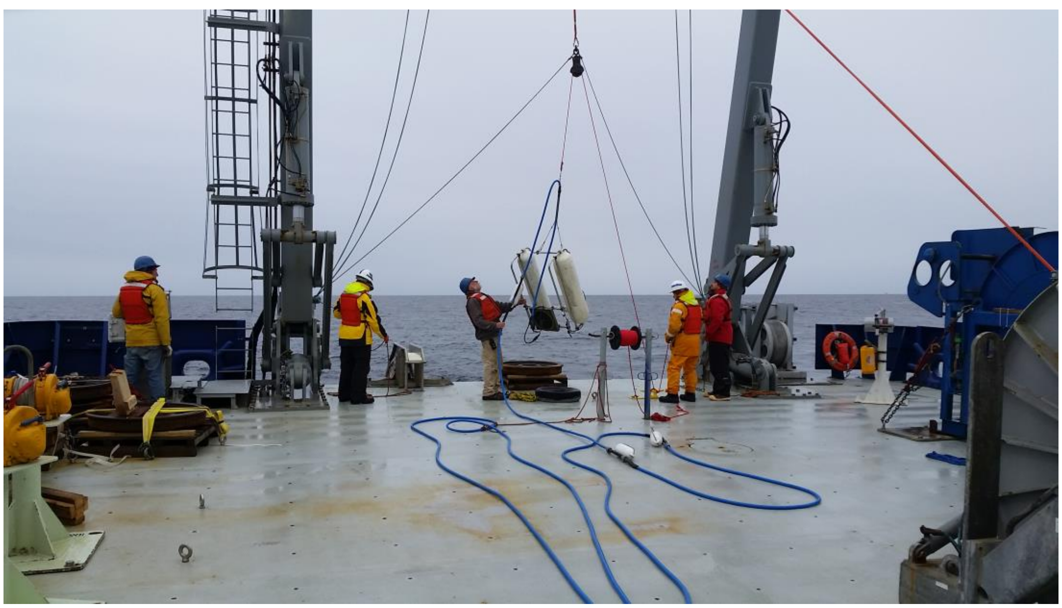

*Figure 9: Deployment of impulses source "boomer " system used during moored wide-angle measurements.*

## Appendix B: Array Aperture Schematic

The figure below displays a schematic of the FORA system and the physical length (not acoustic aperture) of each individual module. Only the triplet (cardioid) module and forward VIM modules and drogue were used in this work. These modules are circled in red.

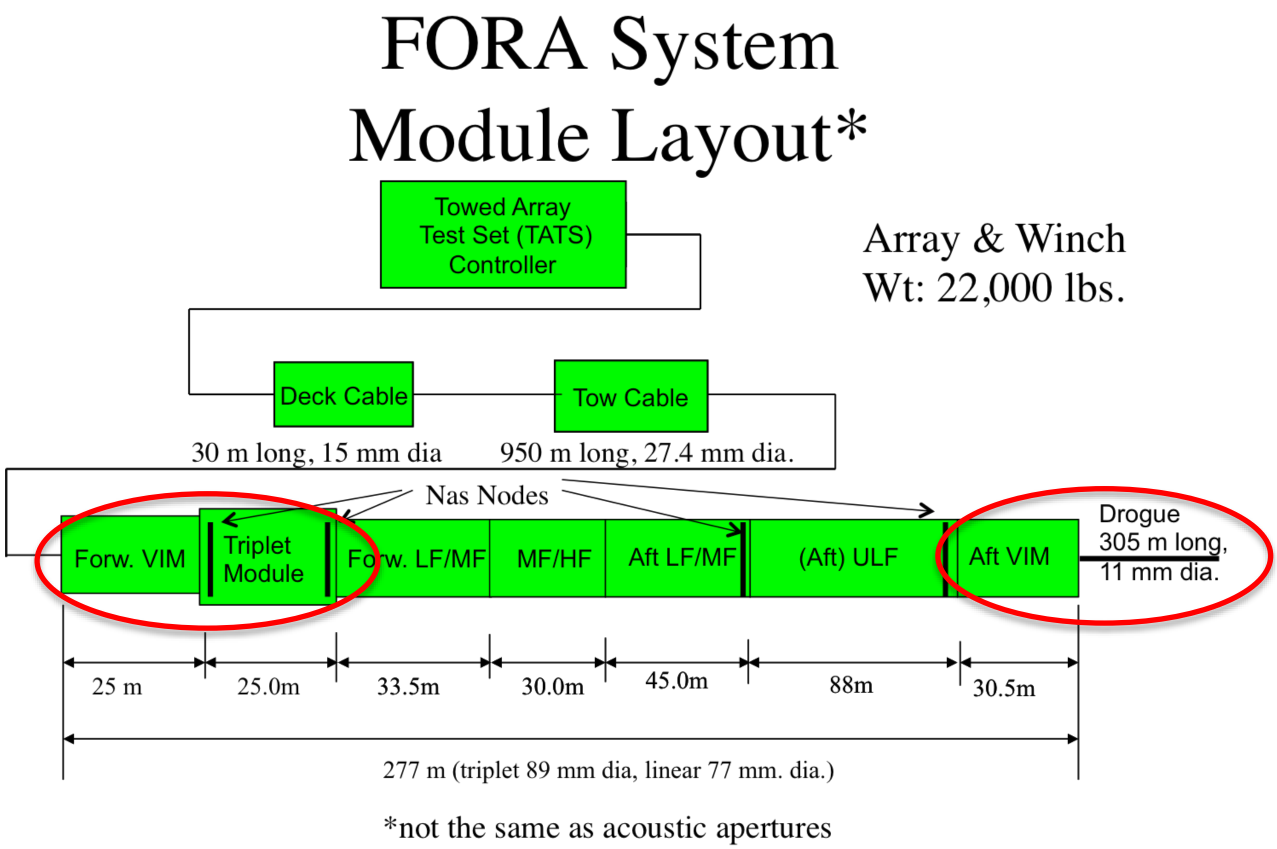

# ATTACHMENT 5

ıce and Technology Organization
Maritime Research and Experimentation
le San Bartolomeo 400
ı26 La Spezia, Italy



# Penn State University/ARL
# Contract/PO 940779
# FORA Replacement Array

# FAT Specification and Results

**DOCUMENT No. ED/LT/2021_03**

---

Revision History

| ISSUE | DRAFT | DRAFT 2 | FINAL | | |
|---|---|---|---|---|---|
| DATE | July 2021 | Aug 2021 | 3 Sept 2021 | | |

**Principal Author:** ……………………………………………………………………………………

Luigi Troiano (CMRE Project Manager)

**Co-Authors:** R. Dymond, M. Bernardini, A. Sapienza, D. Pinzani, R. Azzarini, G. Sambucetti

**Accepted:** ...........................................................................................

Chad Smith (Penn State University/ARL Project Manager)

# 1 Introduction

This report details the final FAT testing of the completed "FORA Replacement Array System" for Penn State University, with the aim of satisfying the requirements for payment #5 in the contract.
According to the payment schedule [see Annex], the milestones required for authorisation of instalment 5 are "Factory Acceptance Test (Bench Test in air)".
Tests described in the following sections will demonstrate that all the system components (see table 1) are functioning correctly.

*Table 1. FORA-Replacement Array Deliverable Components*

| ITEM |
|---|
| ACPS (Acquisition, Control, Power Supply Rack) |
| Deck Cable |
| Winch Junction Box (incl. towcable dry-end termination) |
| Towcable Electro-mechanical termination with integrated E/O converter |
| VIM |
| Array Module |

# 2 FORA-Replacement Array; Component Identification

## 2.1 Acoustic Module

The Acoustic Module [1] consists of 128 hydrophone-preamplifier pairs, four 32-channel digitisers, four NAS units (containing depth, heading and attitude sensors) plus power supply DC/DC converters. The electronic components are fixed to PVC bulkheads in a string assembly with two Dyneema ropes used as strength members. The complete assembly is housed in a 77mm diameter polyurethane hose 50.5m in length and filled with ISOPAR-V oil (see figure 1). The module is connectorised with a Souriau M-32-pin connector [1] at the leading end and the same connector but socket and unwired at the trailing end. The latter connector is provided for addition of extra modules in future.

## 2.2 Vibration Isolation Module (VIM)

The VIM contains no active electronic components; only wiring between the Acoustic Module and E/O converter. The string assembly is composed of PVC bulkheads attached to strength member pairs: Nylon (25m in length) and Dyneema 27m in length (ensuring a maximum of 10% elongation). The VIM assembly housed in a 77mm diameter polyurethane hose, 25m in length and filled with ISOPAR-V oil. The Leading end connector is a Souriau M-32-pin; the trailing end is a Souriau M-32-socket (visible in figure 1)

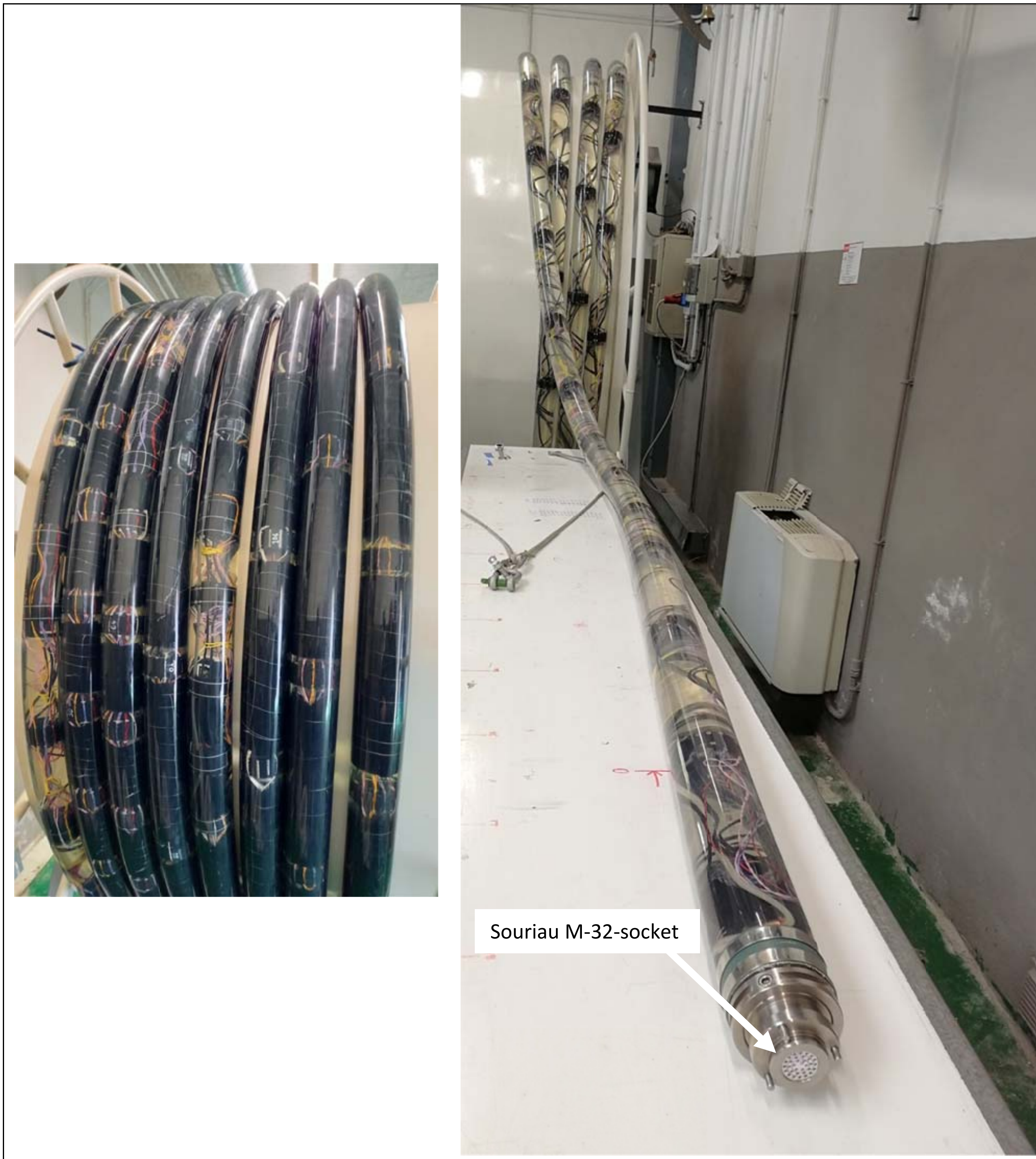


*Figure 1 Acoustic Module (left), VIM (right)*

## 2.3 E/O Converter and Tow Cable Termination

The tow cable Electro-Opto-Mechanical termination is a 5-component universal joint design and houses the single-mode E/O converter [3]. The finished product is shown in figure 2.

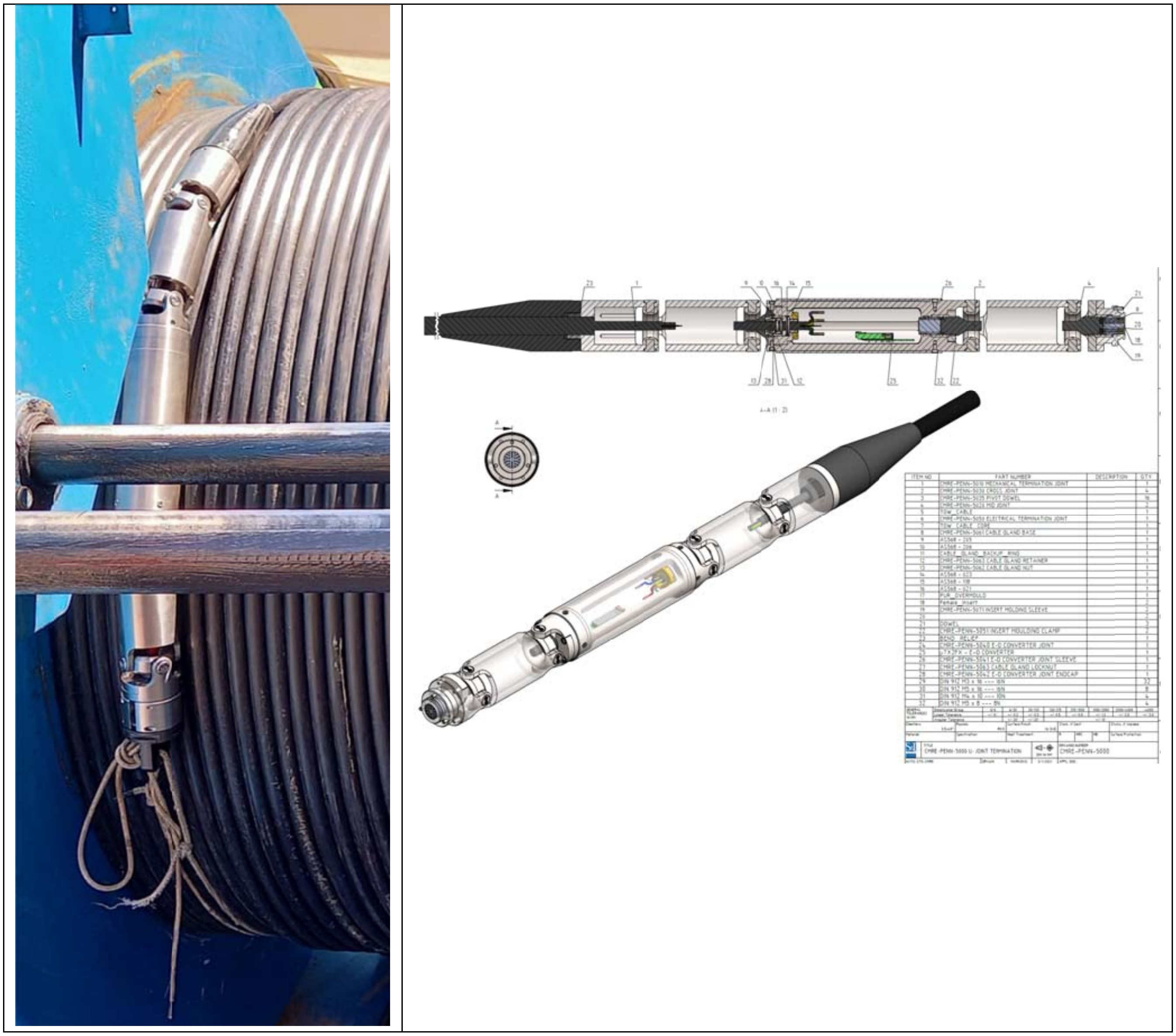

*Figure 2 The* 5-component universal joint that makes up the Electro-Opto-Mechanical termination with integrated E/O converter (left), and schematic (right)

## 2.4 Tow Cable and Winch

The original FORA winch is functioning well and has been left substantially untouched, apart from maintenance on the seized pulley [3]. The tow cable has been re-terminated at both ends; the wet end with the Electro-Opto-Mechanical termination and the dry end with a Junction Box (fixed inside the drum).

*Figure 3. FORA Winch and Towcable (provided by Penn State University)*

## 2.5 Winch Junction Box

The winch junction box provides the dry-end termination point for the tow cable and provides electro-optical connections to the deck cable. It is bolted to a plate inside the winch drum and is accessed through a side opening. Electrical connector is a Burton 55-series, 10-pin connector. Optical connectors are standard LC type with water resistant housing (figure 4).

*Figure 4 Winch Junction Box: tow cable entering box via a cable gland (left), Electrical and optical connectors from the deck cable (foreground)*

## 2.6 Deck Cable

The deck cable provides the connection between the winch junction box and the Laboratory unit (Acquisition, Control, Power-Supply - ACPS). Connectors are Burton 55-series 10-pin and Optical LC on winch end; Amphenol and Optical LC at the laboratory unit.

*Figure 5 Deck Cable entering winch drum for connection to J-Box (left). Mechanical strain releif is provided via a Kevlar eye-grip. Deck cable on drum (right)*

## 2.7 Acquisition, Control, Power-Supply Rack (ACPS)

The ACPS houses array power supply, Precision Time Protocol (PTP) clock, Gigabit Ethernet switch and data acquisition/storage PC (see table 2 and figure 6)

*Table 2 List of components comprisng the ACPS*

| Item | Model/description |
|---|---|
| Case with 19" Rack | Watertight 19" rack-mount, 9U |
| Acquisition/data Storage PC | DELL Precision 3930 |
| Ethernet switch | TP-Link T1600G-28TS |
| PTP Grandmaster Clock & GPS antenna | Sonifex AVN-GMCOS-OCXO |
| Array power supply | TDK-Lambda Z100-4-LAN-U |
| GPS Antenna | Quadrifilar Helix, 32dB Gain |

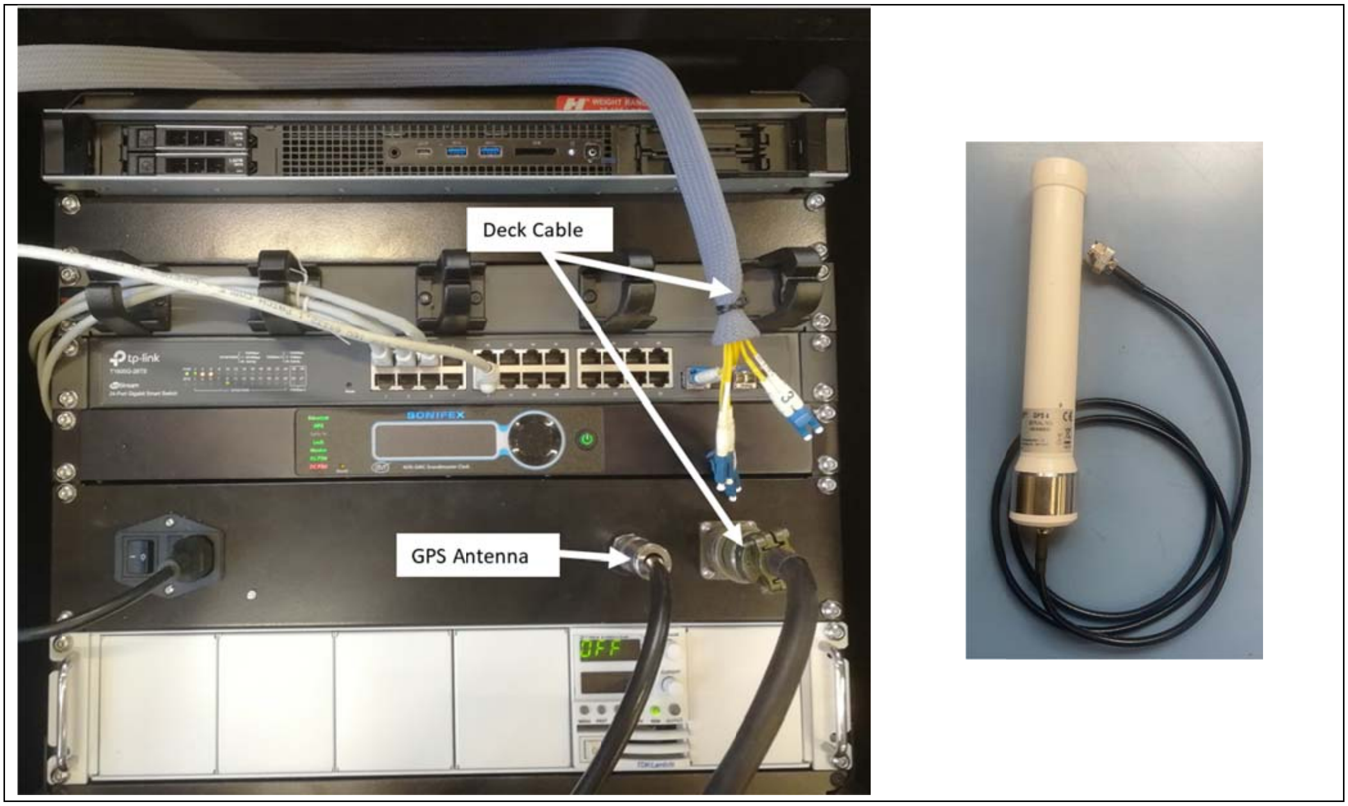


*Figure 6 Acquisition, Control, Power-Supply Rack (ACPS). From top to bottom: DELL Precision 3930, TP-Link Ethernet Switch, Sonifex PTP clock (GPS antenna on right), Connection panel, TDK-Lambda power supply (for array)*

## 3 Array and VIM, Length and Weights (17th May 2021)

Acoustic Module and VIM were weighed using a KERN FH 5K digital force gauge. The modules were loaded in turn, onto a drum and lifted with a fork-lift (figure 7). The results are shown in table 3. The VIM is about 1kg above target weight, whilst the Acoustic module is 1.6kg above target weight. This is considered an excellent result and will allow any fine trimming to take place at sea by the addition/removal of oil. Acoustic module length was measured under tension. VIM length was measured without load.

*Table 3. Target and measured weights and lengths of the Acoustic Module and VIM*

| Item | Target length | Measured length | Target weight (Note 2) | Measured weight |
|---|---|---|---|---|
| | metres | metres | kg | kg |
| **VIM** | 25 | 25.3 | 121.19 | 122.2 |
| **Acoustic Module** | 50.565 | 50.581 (Note 1) | 242.3 | 243.9 |
| Note 1: measured with 400N tension | | | | |
| Note 2: assume nominal diameter of 77mm, water density=1028.7kg/m3 (density at 10bar, 15°C, 38ppt) | | | | |

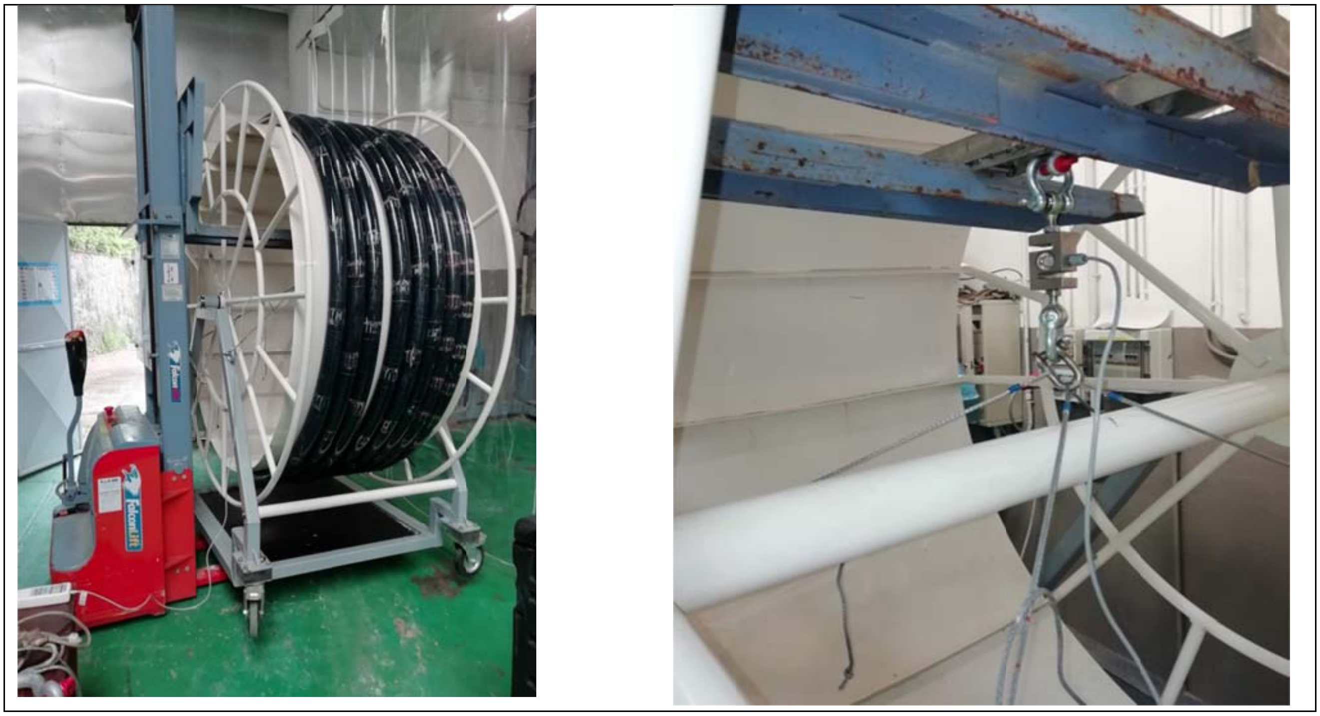

*Figure 7. Acoustic module on drum, being weighed (left). Close up of Force Gauge load cell (right)*

## 4 Power-on test of complete System (23rd June 2021)

- **Deliverable equipment used:** ACPS with GPS antenna, Deck Cable, Winch J-Box, Tow cable, E/O Converter, VIM & Acoustic Module
- **Non-Deliverable equipment used:** PC running Dashboard/monitoring software

The complete system is assessed in this test. The following components: ACPS with GPS antenna, Deck Cable, Winch J-Box, Tow cable, E/O Converter, VIM & Acoustic Module (on 1.9m diameter drum), were connected, and the system started as follows:

- Switch on ACPS Rack, and wait for Acquisition PC to boot and the PTP clock to 'Lock' (figure 8)
- From the Dashboard PC, run the power supply monitoring utility (*startCAPSM.sh*)
- From the Acquisition PC, launch the configuration script, '*BOOTandSTARTALL.sh'*. This will standby, listening for boot messages from the µDASS units, before proceeding automatically to the µDASS setup stage.
- Switch on TDK-Lambda PSU. The display should read about 70V and 1A. These values are repeated in the Dashboard PC display (figure 8) and summarised in table 4.
- Acquisition PC displays the 5 µDASS 'successful boot' messages, and subsequently configures the units as follows:
    - Sets up control ports, number of modules present, master/slave, acoustic channel sampling frequency
    - Sets up NAS streaming, one per active module (4 NAS units total in the Acoustic Module)
    - Starts the µDASS data streaming
- Current consumption increases from 1A to 1.4A when the µDASS units are streaming data (table 4)
- From the Dashboard PC lauch the Acoustic and NAS monitoring utilities (*startCAAN.sh and startCANAM.sh*)

- Screenshot of acoustic channel monitor is shown in figure 9. The LFM sweep seen on the spectrogram was generated by a cellphone. The RMS barchart display shows all 128 hydrophones functioning correctly.
- Figure 10 is a screenshot of the NAS monitor. Depth and heading sensors are functioning correctly. Pairs of heading sensors are pointing in opposite directions (180 degrees apart). This is explained by the position of the sensors on the drum: two are near the top of the drum and two near the bottom (the 4 NAS sensors spacings are approximately 13.9m, 11.7m, 11.3m [1] and the drum diameter is 1.9m)

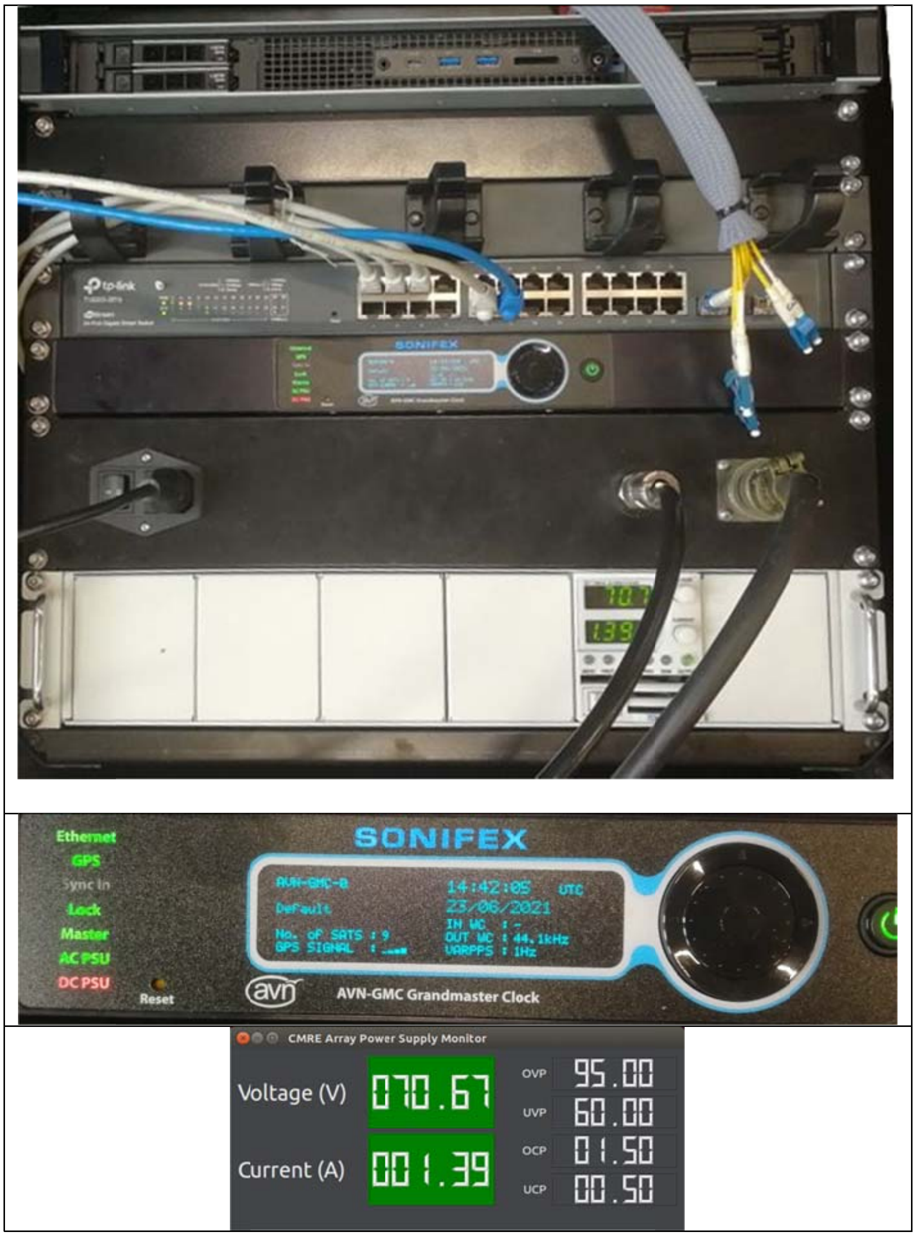


*Figure 8. Top: ACPS Rack Powered on with Array PSU indicating 70.7V, 1.39A. Centre: Close up of PTP clock showing 'Locked' status. Bottom: PSU monitor/control display*

*Table 4. System Power-On Test*

| | | | |
|---|---|---|---|
| Array Supply Voltage | 70.7 V | Array supply current (standby) | 1.04 A |
| Array Supply Voltage | 70.7V | Array supply current (acquisition) | 1.39 A |

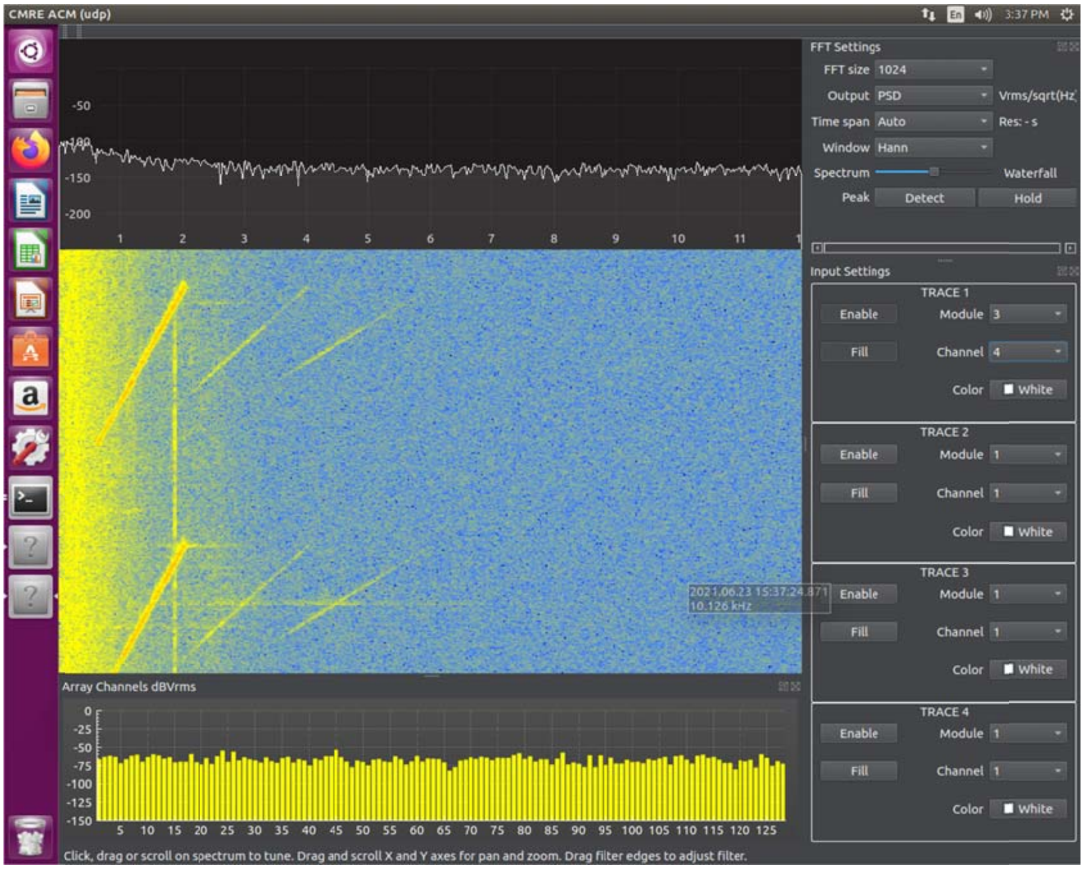


*Figure 9 Screenshot of Acoustic Channel Monitor with Acoustic Module wrapped around a drum. Spectrogram is of µDASS module 3, channel 4 (hydrophone number 2*32 + 4 = 64). The LFM visible is generated by a cellphone placed close to the array.*

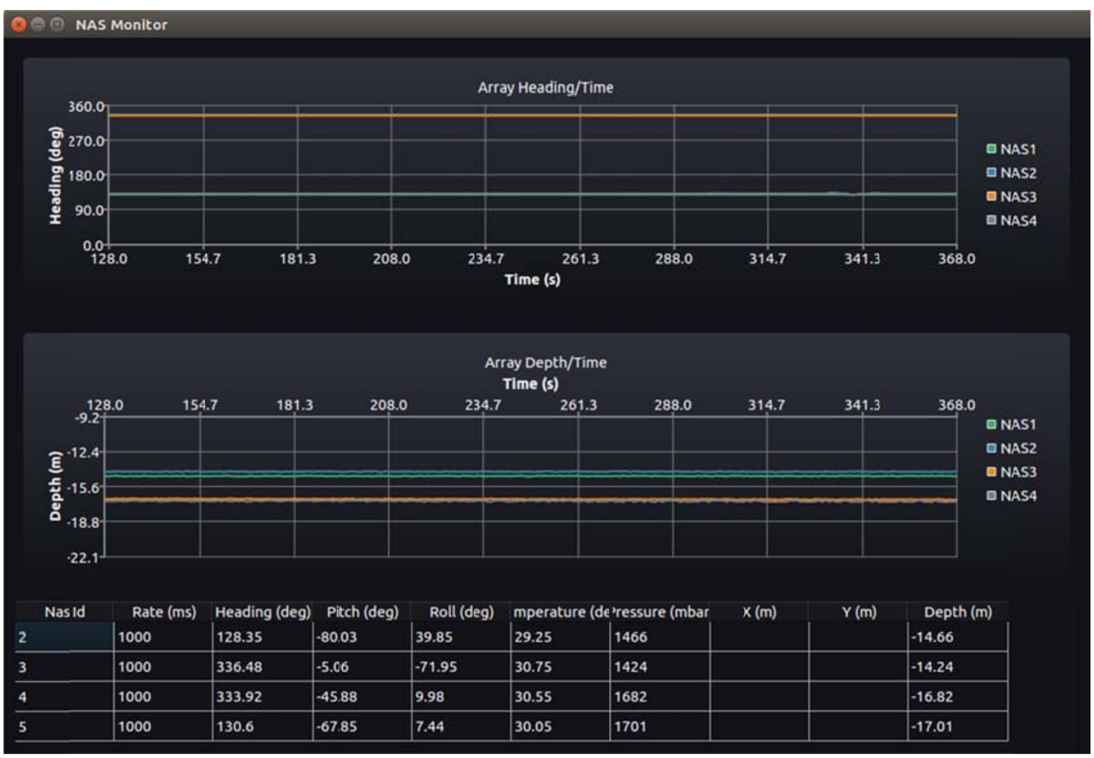


*Figure 10 NAS monitor screendump, showing heading sensors (top) and depth sensors (bottom). The 4 sensor readings have grouped into pairs, due to their positioning on the drum.*

# 5 Data-Link Throughput Test (24th June 2021)

- **Deliverable eqipment used:** E/O converter, Towcable, J-Box, Deck Cable, TP-Link Ethernet Switch
- **Non-Deliverable equipment used:** Data generation PC, Data reception PC

The aim of this test is to estimate the bandwidth of the **E/O convereter → Towcable → J-Box→ Deck Cable→ACPS (Ethernet Switch)** data telemetry chain. The tool used to check the link is '*iperf*': a Linux tool for performing network throughput measurements. To perform an '*iperf*' test the user must establish both a server (to accept traffic) and a client (to generate traffic) on 2 PCs equipped with Gigabit Ethenet Cards. The following sequence of measurements was performed.

## 5.1 Determine maximum throughput of the test equipment

The first step is to establish the maximum data throughput of the measurement system; connect the server and the client PCs directly to the Gigabit Network Switch using two standard RJ45 cables (see figure 11. Start with a high data throughput, which generates lost packets (figure 12), and reduce in steps until **zero** lost packets are reported

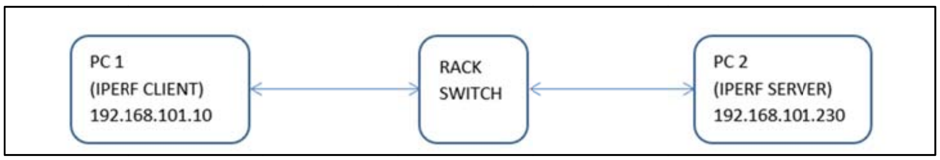


*Figure 11. Connection used to verify the data throughput of the measurement system*

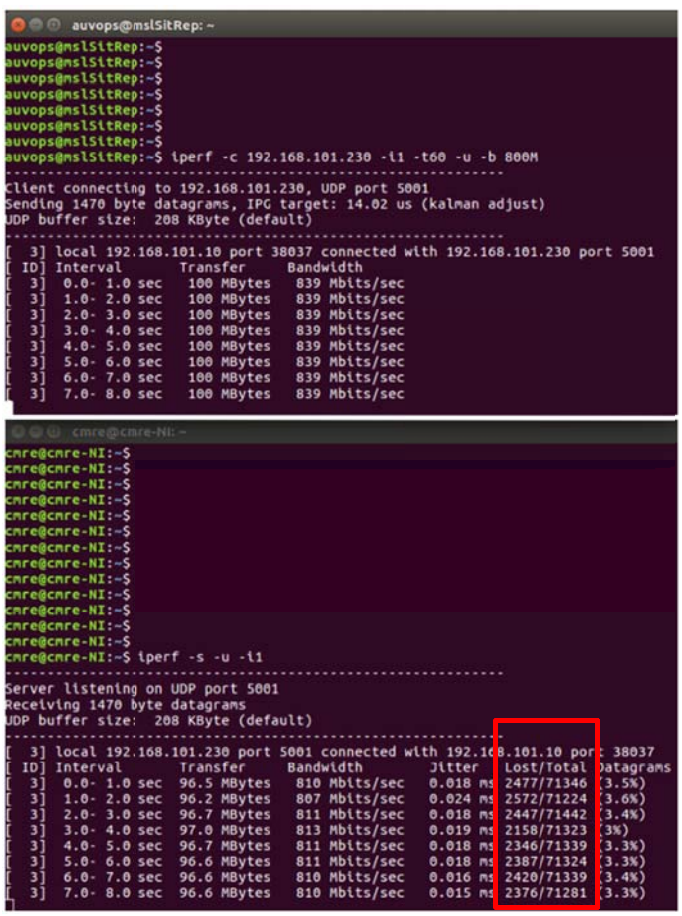


*Figure 12 Top: 'iperf' data generation (client) generating UDP packets at a rate of 839Mbits/s. Bottom: 'iperf' data reception (server). The server display indicates lost packets at this data rate.*

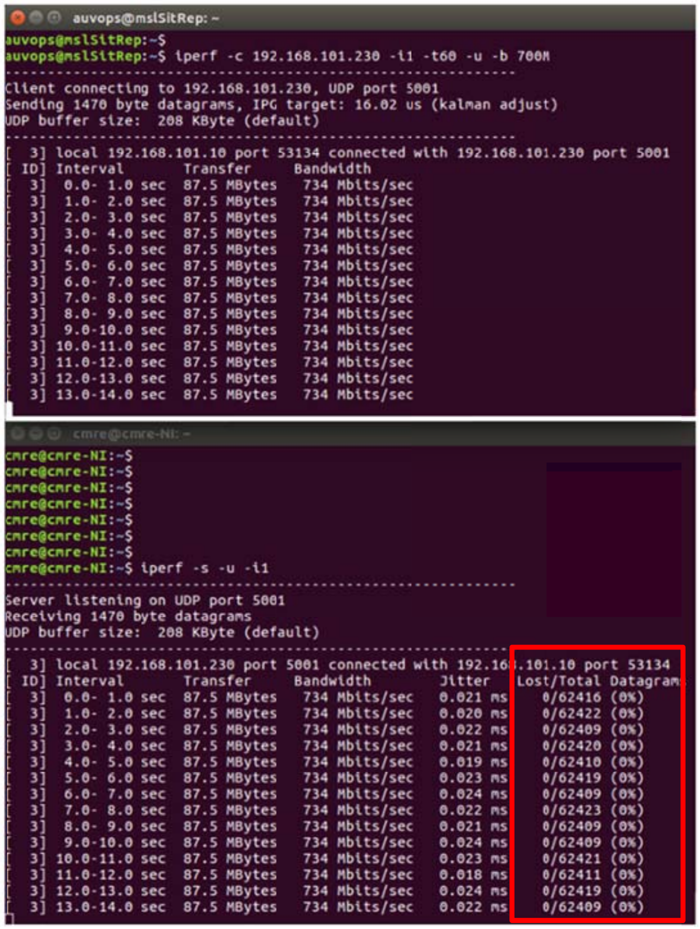


*Figure 13 Top: 'iperf' data generation (client) generating UDP packets at a rate of 734Mbits/s. Bottom: 'iperf' data reception (server). The server display indicates ZERO lost packets at this data rate*

Measurement system bandwidth (throughput) is thereby detemined to be 734Mbit/s.

## 5.2 Determine data throughput of: E/O Convereter→Tow Cable→ J-Box→Deck Cable →ACPS(Switch)

The following components were subsequently added to the 'throughput measurement loop': E/O convereter, Towcable, J-box, Deck Cable. Figure 14 is a block diagram of the final setup. Figure 15 shows the RJ-45 cable from the data generation PC connected to the E/O converter.

The results are shown in figure 16. There are no lost packets at a data thoughput of 734Mbit/s, which implies that the array telemetry components have not degraded the 734Mbit/s capacity of the measurement setup.

Data throughput from the array is currently around 100Mbit/s, which imples a large unused capacity; ideal for any subsequent future additions to the current three-octave system.

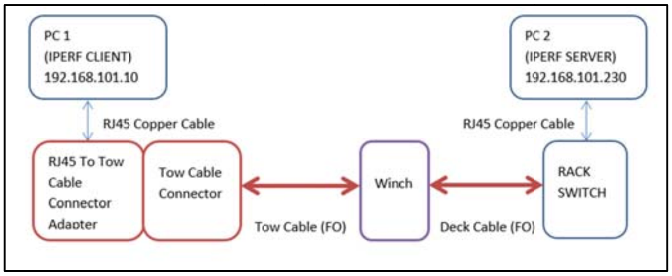


*Figure 14. Data Telemetry Capacity (throughput) measurement setup for the complete system*

*Figure 15. Connection from the Data Generation PC (client) to the Array E/O converter*

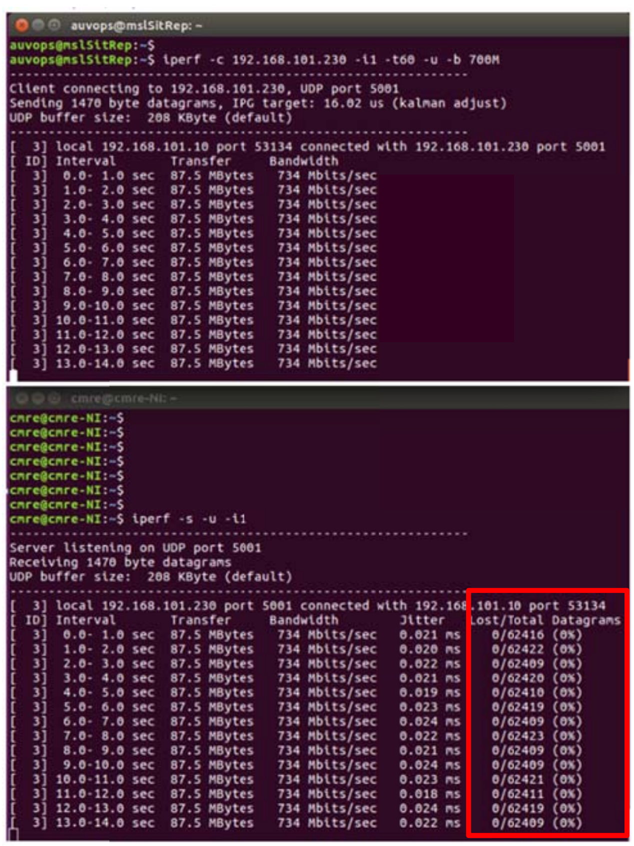


*Figure 16 Complete System Data Telemetry Capacity measurement: There are no lost packets at a data thoughput of 734Mbit/s, which implies that the Array Telemetry components have not degraded the 734Mbit/s capacity of the measurement setup. Therefore 734Mbit/s can be considered a lower bound for the channel capacity (throughput).*

# 6 Acoustic Tests (21-22 June 2021)

- **Deliverable equipment used:** ACPS with GPS antenna, VIM & Acoustic Module
- **Non-Deliverable equipment used:** Test cable (ACPS Rack to VIM connection), PC running CMRE real-time acoustic monitoring software, signal generator, loudspeaker & housing

## 6.1 Hydrophone relative sensitivity

Measurements of relative sensitivity at 609Hz were taken for each channel. The technique involved a loudspeaker enclosure moved along the bench and centred at each hydrophone, whilst emitting a tone at 606Hz. Level in dBV was measured using monitoring software running on the notebook PC, connected to the ACPS ethernet switch (figure 17). At the same time, a noise measurement at 6kHz was taken.

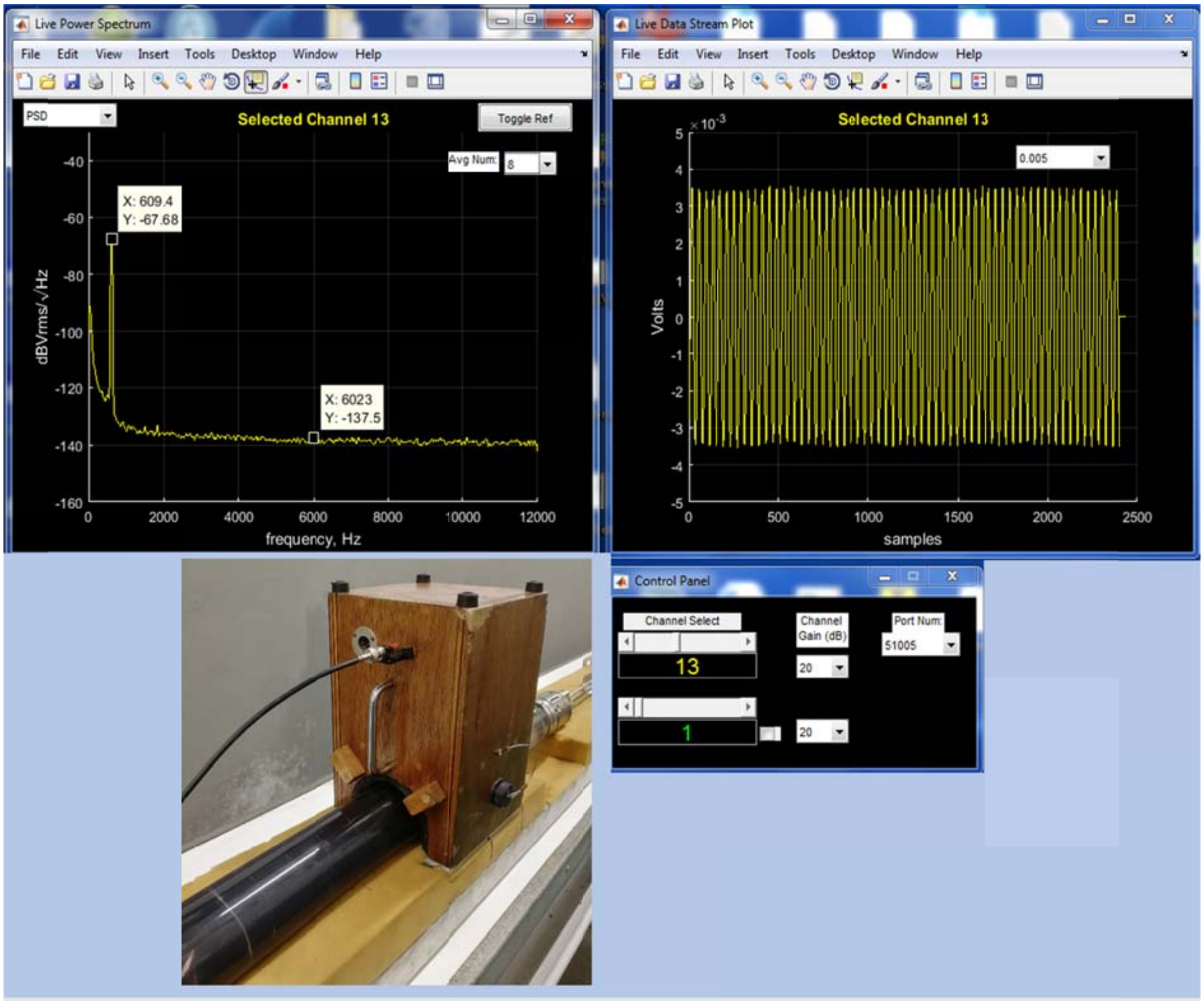


*Figure 17. Real-time acoustic monitoring software for determining: relative sensitivity, channel noise and hydrophone polarity. The cursors on the spectrum plot (left) indicate a level of -67.7dBV @ 606Hz and a noisefloor of -137.5dBV/√Hz. The measurement is for µDASS module #5, channel 20 ( hydrophone # = (5-2)*32+20=116). The loudspeaker is show positioned on the last hydrophone (#128).*

The results are plotted in figure 18 and show a mean value of -67.5dBV with a standard deviation of 0.5dB. Note that the condition of the array has not changed after hosing and oil filling; the same three outlier channels are evident, as stated previously in the Pre-FAT report [3].

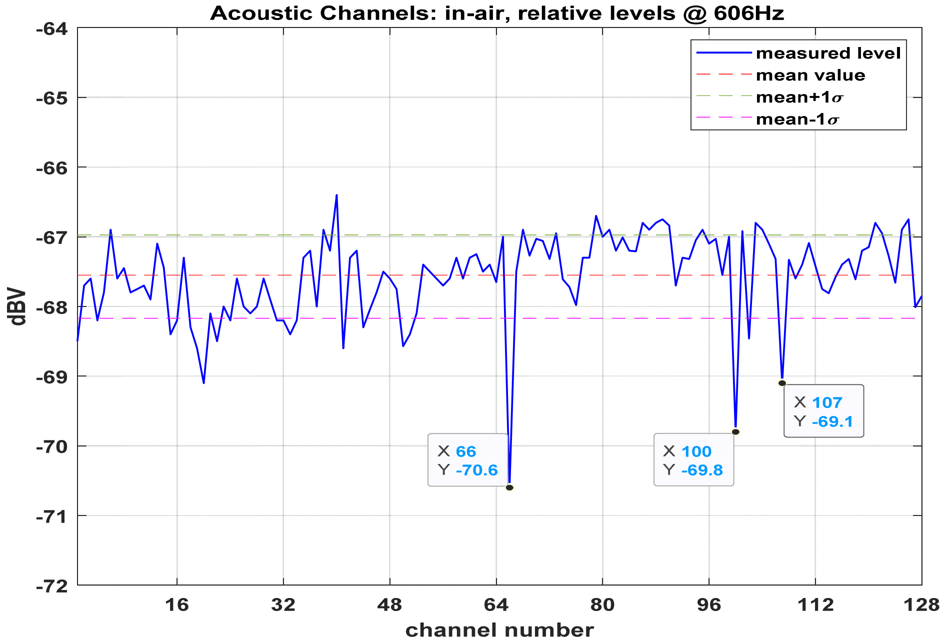


*Figure 18. Acoustic level at 606Hz for each hydrophone, The standard deviation is 0.5dB. Outlier channels 66, 100 and 107 are evident*

## 6.2 Channel Noise Floor at 6kHz

In parallel with the above measurements, the channel noise floor was measured at 6 kHz, using the same software with an 8-FFT average. The resulting measurements (in dBV/√Hz) are shown in figure 19. The same measurements converted to equivalent pressure in dB re 1V/µPa are also shown in the figure (using channel gain of 32dB and SEA-L16 hydrophone sensitivity of -201dB re 1V/µPa).

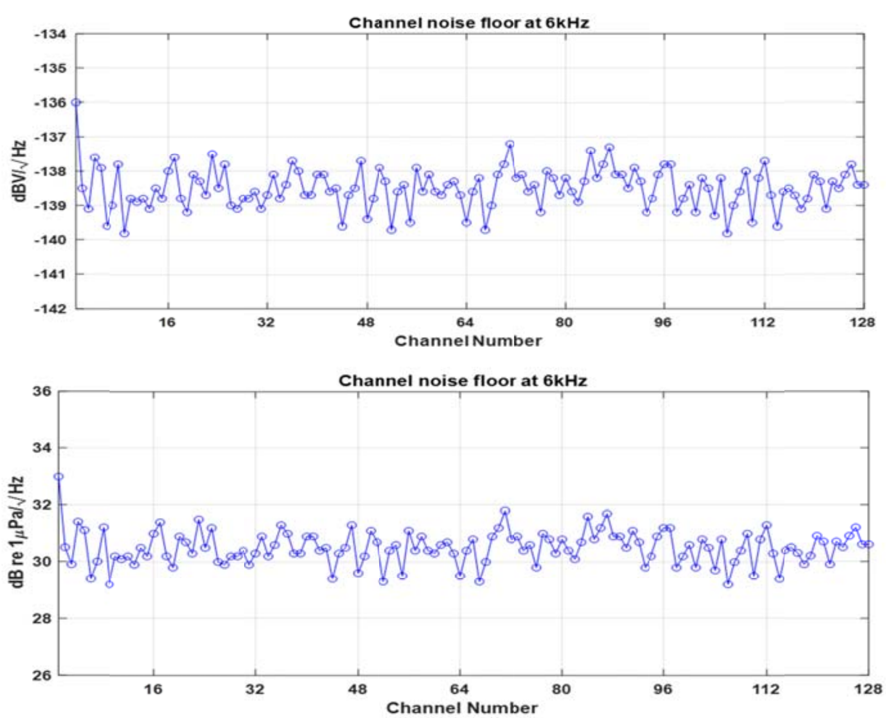


*Figure 19. Channel noisefloor at 6kHz. Top: the raw measurements in dBV/√Hz. Bottom: converted to equivalent pressure using channel gain and hydrophone sensitivity.*

## 6.3 Hydrophone Polarity

By switching the signal generator to pulse mode, the polarity of the leading edge of the received pulse could be measured. The results (all positive) are shown in figure 20.

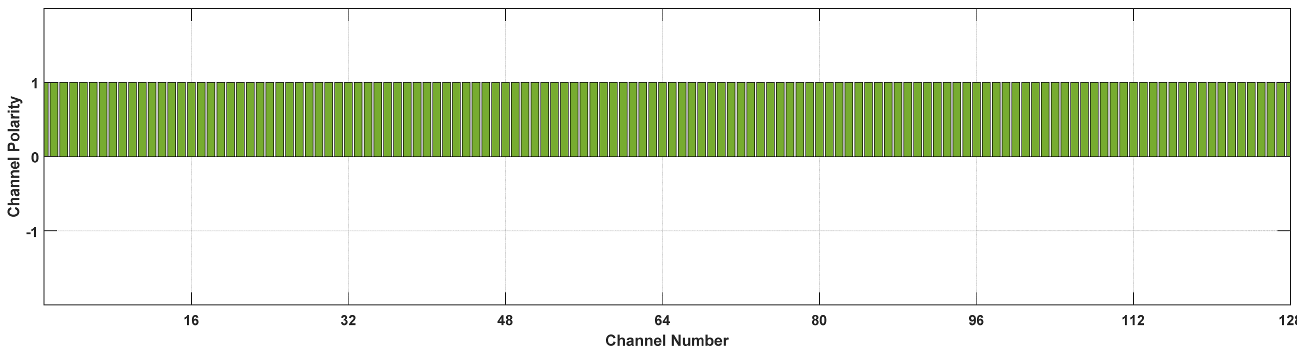


*Figure 20. Hydrophone channel polarity*

## 6.4 Phase measurement on 3 outlier channels (21st June 2021)

- **Deliverable equipment used:** ACPS with GPS antenna, VIM & Acoustic Module
- **Non-Deliverable equipment used:** Test cable (ACPS Rack to VIM connection), PC running Wireshark & MATLAB script to align received signals, signal generator, loudspeaker & housing

The issue of the 3 outliers (channels 66, 100,107) was previously raise in the Pre-FAT report [3]. Penn State University project manager requested phase measurements to be taken on these 3 channels.

The technique was to use the PPS generated by the Sonifex PTP clock, to trigger a signal generator, transmitting a 600Hz tone burst which was in turn connected to the loudspeaker. The UDP stream from the array was captured on a laptop PC running Wireshark, and the resulting pulses were aligned using a MATLAB script. This data alignment with PPS technique had been developed previously [4].

For each outlier channel, the signal from the preceding channel was acquired as a reference. Subsequently the following processing was used to extract the phase information:

- Calculate the coherence between the outlier channel and its reference channel
- Calculate phase of the cross-spectrum of the two channels at 600Hz

The processing steps are shown in figures 21 – 24, with the results summarised in table 4.

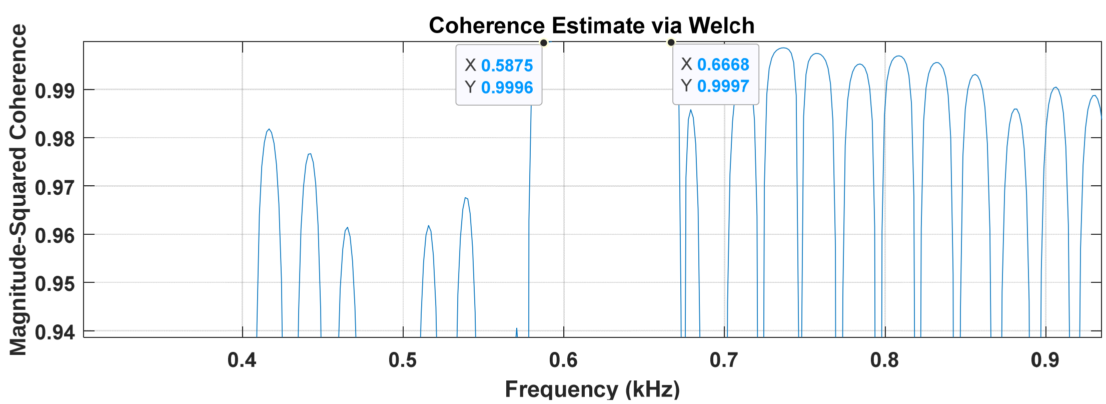


*Figure 21. Coherence of channels 65 and 66. It shows that measurements between between roughly 590Hz and 670Hz can be considered reliable.*

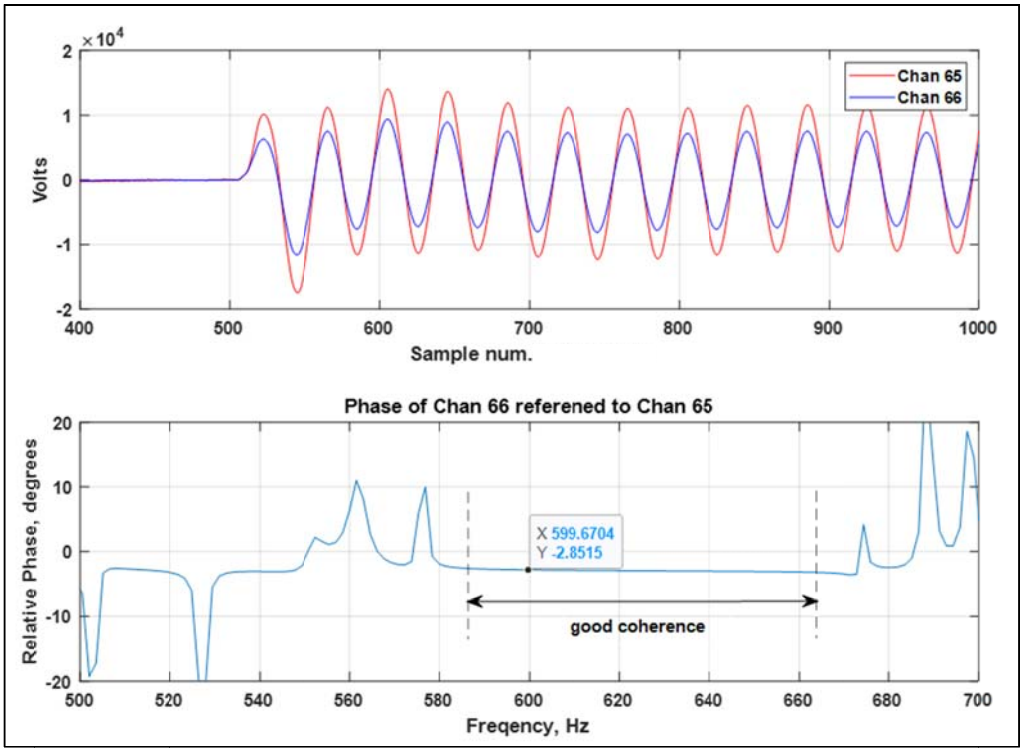


*Figure 22. Channel 66 synchronised time-series (top) and cross-spectrum phase (bottom) with reference to channel 65*

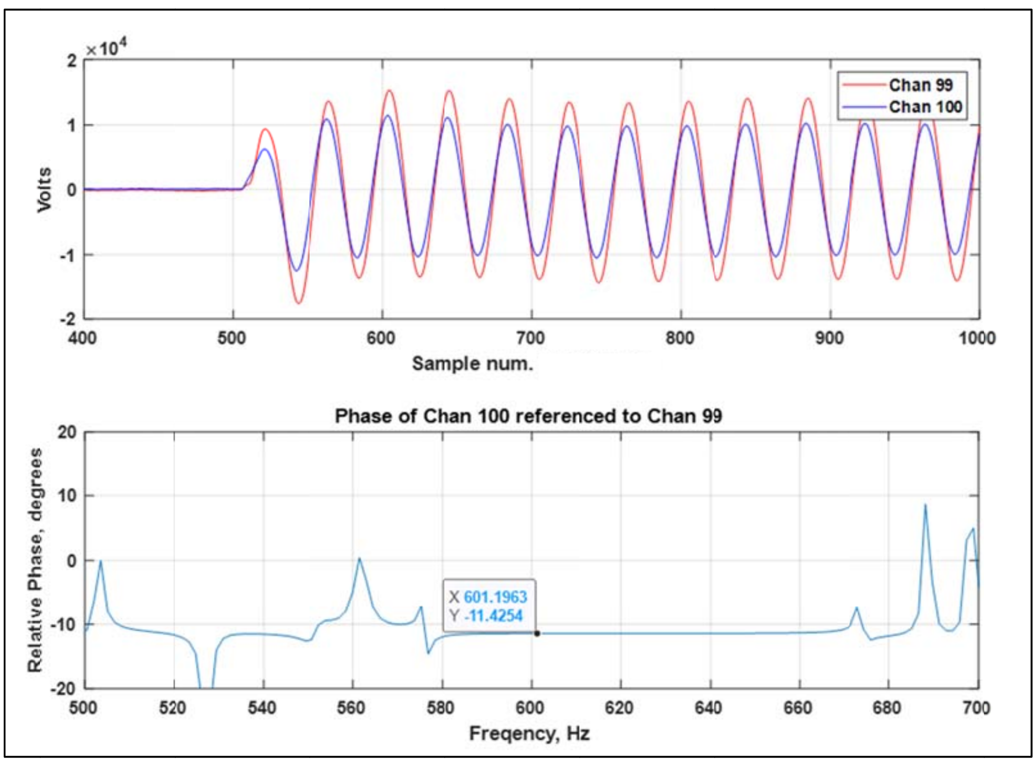


*Figure 23. Channel 100 synchronised time-series (top) and cross-spectrum phase (bottom) with reference to channel 99*

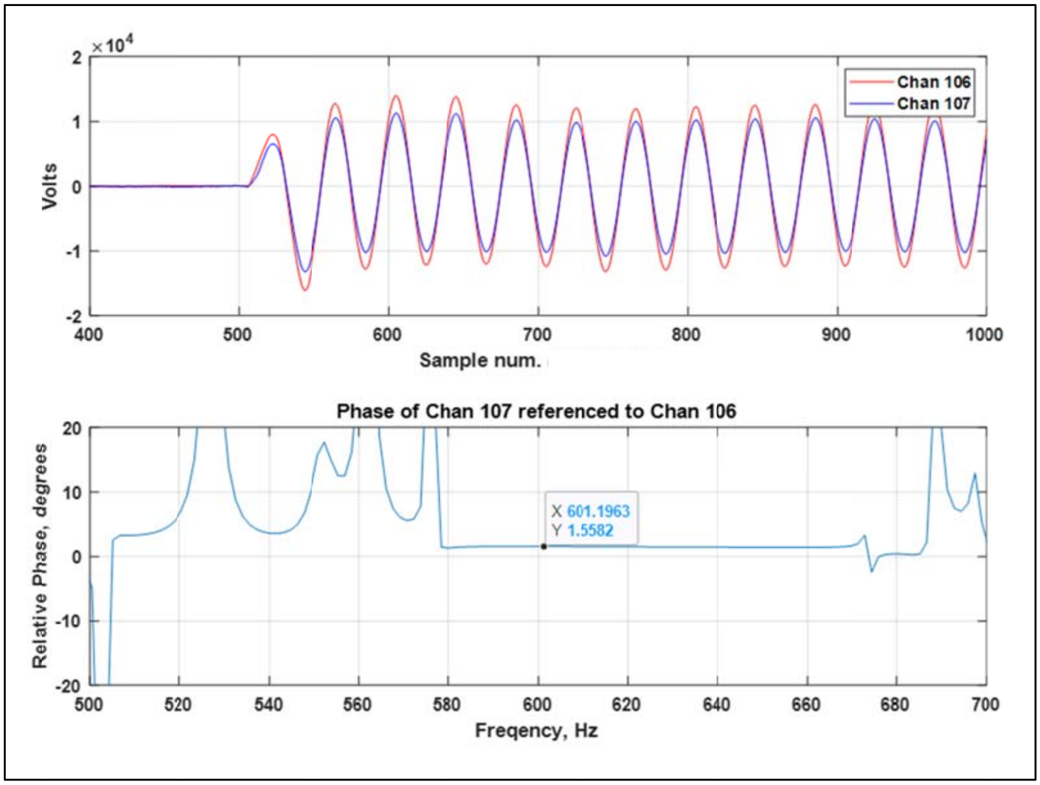


*Figure 24. Channel 107 synchronised time-series (top) and cross-spectrum phase (bottom) with reference to channel 106*

*Table 4. Summary of outlier channel phase measurements at 600Hz*

| Outlier Channel # | Phase @ 600Hz Degrees |
|---|---|
| 66 | -2.9 |
| 100 | -11.4 |
| 107 | +1.6 |

## 6.5 Data Acquisition: Transmission of LFM chirp with loudspeaker positioned at forward end-fire (22nd June 2021)

- **Deliverable equipment used:** ACPS with GPS antenna, VIM & Acoustic Module
- **Non-Deliverable equipment used:** Test cable (ACPS Rack to VIM connection), Signal Generator, Loudspeaker

The aim of this test was to acquire data using the ACPS acquisition hardware/software, subsequently providing Penn State University with the raw data files.

A loudspeaker was positioned at one end of the workbench, closest to the array leading end (hydrophone 1). The array was arranged in a straight line along the bench (figure 25), and an LFM chirp with the characteristics in table 5 was transmitted, triggered by PPS. The 8 data files acquired using the deliverable software *'FORA_sw.exe'* running on the acquisition PC (ACPS rack), are shown in figure 26. Each consists of around 20 seconds of data.

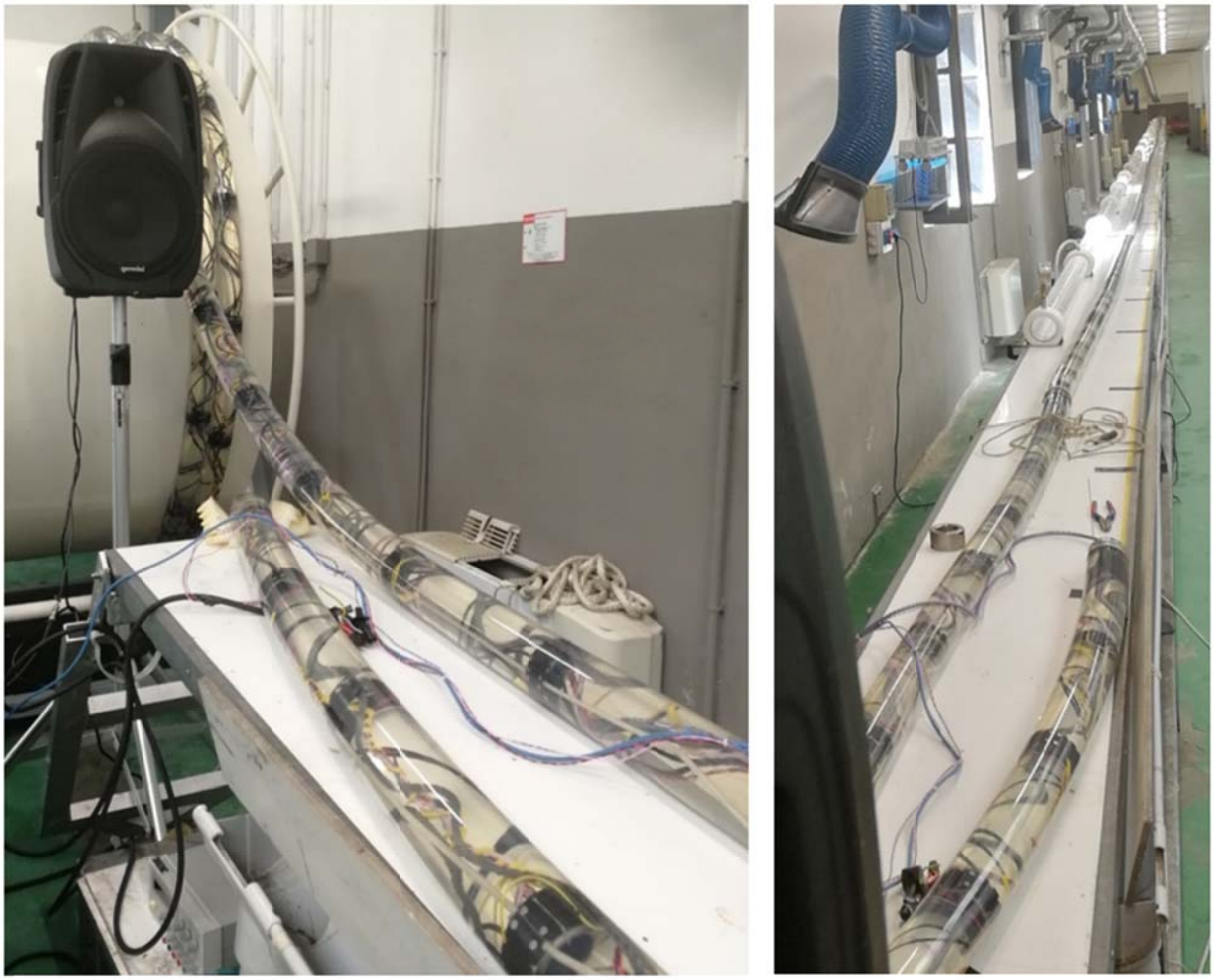

*Figure 25. Experimental setup used to generate raw data files for Penn State University. Louspeaker (left) transmits LFM (see table 5). Array laid out on the bench in a straight line is visible (right)*

*Table 5. Characteristic of the LFM chirp used as a test signal for the Data Acquisition test*

| LFM characteristics | |
|---|---|
| Start frequency (Hz) | 100 |
| Stop frequency (Hz) | 10000 |
| Duration (ms) | 500 |
| Window | Tukey (1%) |
| Repetition interval (PPS) | 1s |

| Name | Date modified | Size |
|---|---|---|
| fora_2021173154700.dat | 22/06/2021 15:48 | 235,815 KB |
| fora_2021173154700.head | 22/06/2021 15:48 | 1 KB |
| fora_2021173154720.dat | 22/06/2021 15:48 | 240,000 KB |
| fora_2021173154740.dat | 22/06/2021 15:48 | 239,993 KB |
| fora_2021173154800.dat | 22/06/2021 15:48 | 240,000 KB |
| fora_2021173154820.dat | 22/06/2021 15:48 | 239,993 KB |
| fora_2021173154840.dat | 22/06/2021 15:48 | 240,000 KB |
| fora_2021173154900.dat | 22/06/2021 15:48 | 239,993 KB |
| fora_2021173154920.dat | 22/06/2021 15:48 | 129,008 KB |

*Figure 26. List of the files acquired with LFM chirp*

A snippet of one of the files; `fora_2021173154720.dat,` is plotted in figure 27.

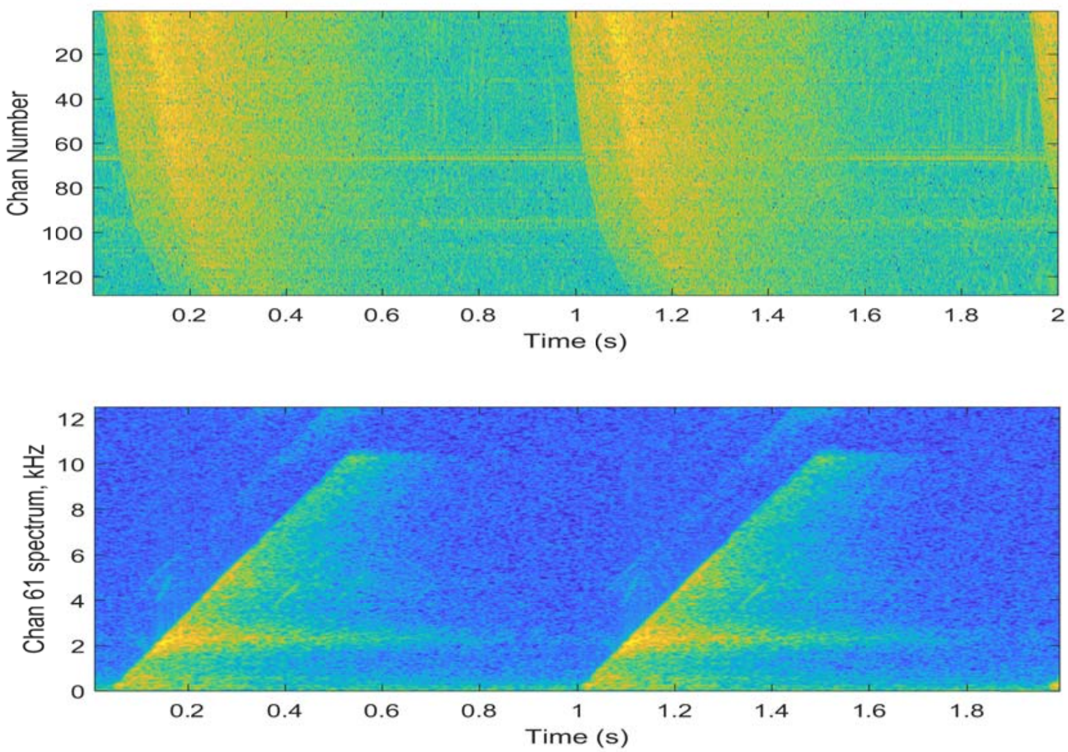


*Figure 27. A two-second snapshot of* `fora_2021173154720.dat.` *Top: RMS level for all channels. Bottom: spectrogram of channel 61*

The procedure was repeated, but without signal transmissions, acquiring only background noise. The acquired file list is shown in figure 28. A snippet of data from the file `fora_2021173161220.dat` is shown in figure 29

| Name | Date modified | Size |
|---|---|---|
| fora_2021173161200.dat | 22/06/2021 16:22 | 228,278 KB |
| fora_2021173161200.head | 22/06/2021 16:21 | 1 KB |
| fora_2021173161220.dat | 22/06/2021 16:21 | 240,000 KB |
| fora_2021173161240.dat | 22/06/2021 16:22 | 239,993 KB |
| fora_2021173161300.dat | 22/06/2021 16:22 | 240,000 KB |
| fora_2021173161320.dat | 22/06/2021 16:21 | 239,993 KB |
| fora_2021173161340.dat | 22/06/2021 16:21 | 240,000 KB |
| fora_2021173161400.dat | 22/06/2021 16:22 | 239,993 KB |
| fora_2021173161420.dat | 22/06/2021 16:21 | 240,000 KB |
| fora_2021173161440.dat | 22/06/2021 16:22 | 34,785 KB |

*Figure 28. List of files acquired with only background noise*

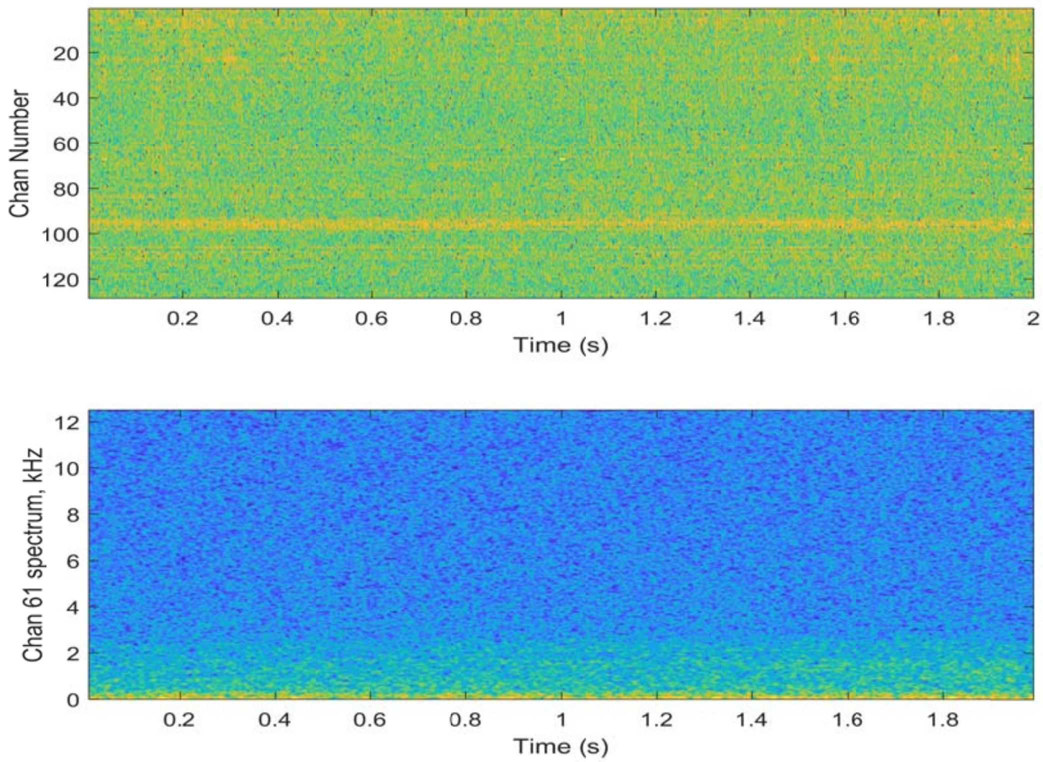


*Figure 29. Two-second snapshot of '`fora_2021173161220.dat`'. Top: RMS level for all channels. Bottom: spectrogram of channel 61*

# 7 Non-Acoustic Channel (NAS) Tests

## 7.1 Test NAS: Pitch (date 10th May 2021)

- Deliverable equipment used: ACPS, VIM & Acoustic Module
- Non-Deliverable equipment used: Test cable (ACPS Rack to VIM connection), 20° Calibration wedge

Switch on and configure the array as outlined in setion 4. Place the wedge under each of the 4 PNI-Seatrax heading sensors (which provide the pitch measurement), in both directions (figure 30). Use the NAS Monitor software (*CANAM.sh*) to acquire the data. Expect values to vary between +/-20°. However, it was noted that the angle of 20° in such a short lenth, was excessive; it was difficult to align the bulkheads inside the array with the wedge (see figure 30, right). The values reported in figure 32 are therfore not representitive of the accuracy of the sensor. The test is anyhow considered adequate for the requirement to evaluate the functionality of the pitch sensors.


*Figure 30. One of the Acoustic Module NAS (Compass) units placed on a 20° wedge. Misalignment of the array bulkheads is evident (right)*

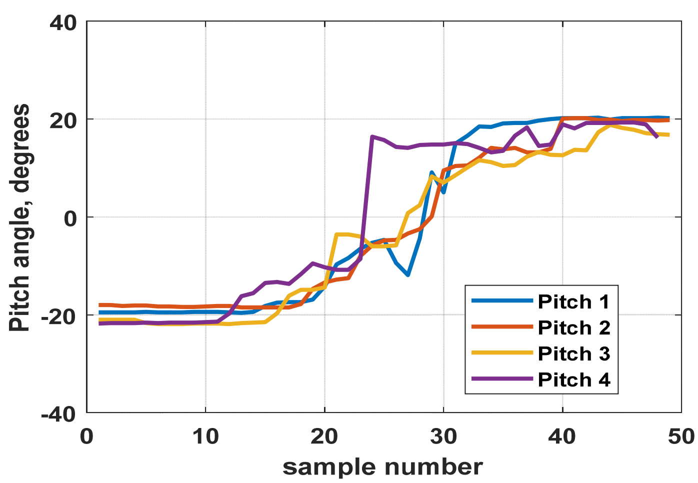


*Figure 31. Pitch measurements varying roughly between +/- 20° for the 4 Compass units*

## 7.2 Test NAS: Magnetic Heading (date 10th May 2021)

- Deliverable equipment used: ACPS, VIM & Acoustic Module
- Non-Deliverable equipment used: Test cable (ACPS Rack to VIM connection), 3-axis Helmholtz coil magnetic calibration system

The technique was previously described [3]. The array contains 4 magnetic heading sensors (PNI-Seatrax). Figure 32 shows the equipment setup. Raw data for a 360° magnetic field rotation for all 4 sensors is plotted in figure 33. Applied heading verses measured heading is plotted in figure 34.

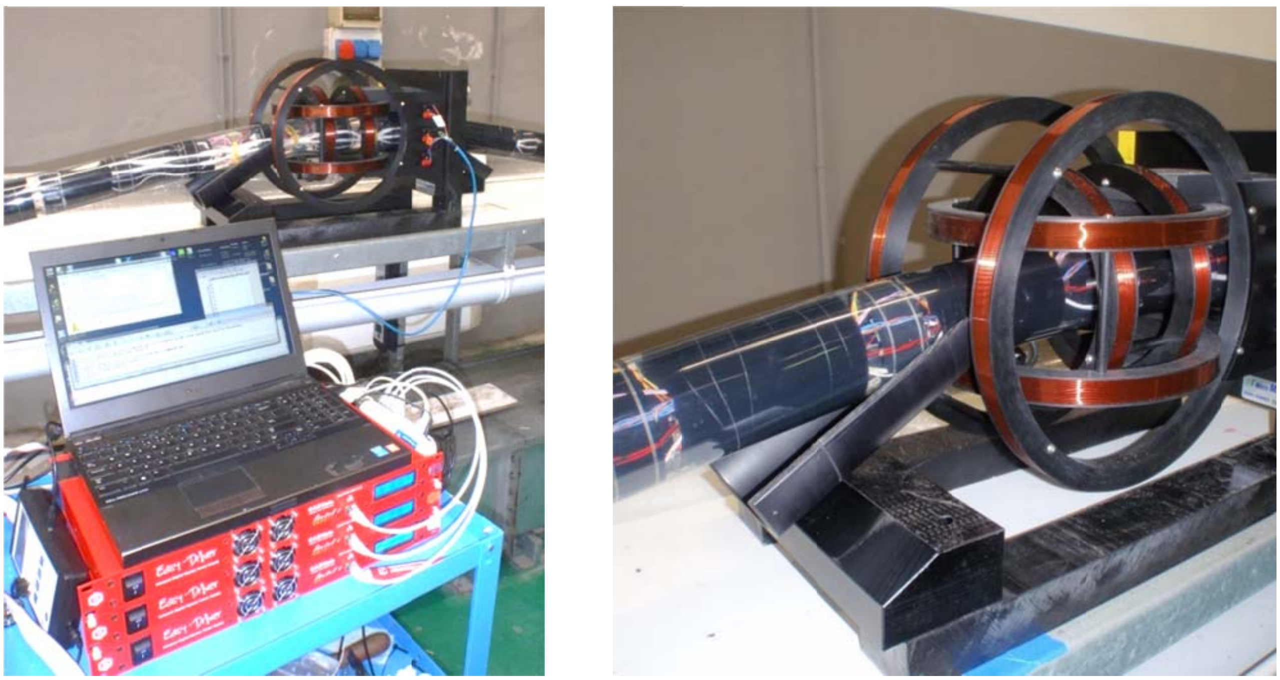

*Figure 32. Measurement setup for testing the 4 heading sensors (PNI-Seatrax). Control PC and power supplies (left), closeup of Acoustic Module threaded through the Helmholtz coils (right).*

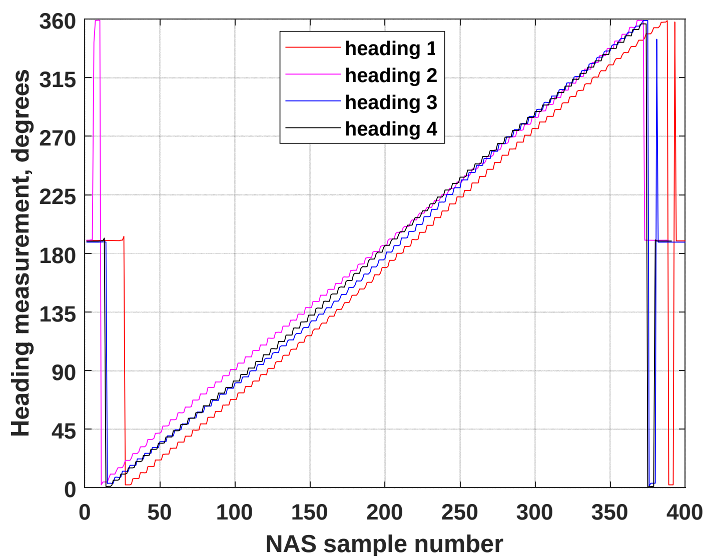


*Figure 33. Raw data from all 4 of the heading sensors. The heading within the Helmholtz coil is varied from 0° to 360° in 5° steps, by varying the current in the coils. Note: x-axis is not aligned between channels.*

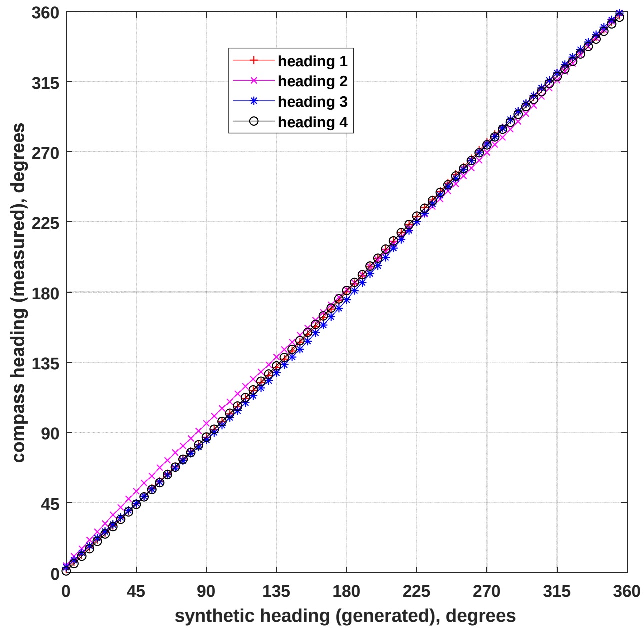


*Figure 34. Applied heading vs. measured heading for the 4 heading sensors, showing a unit slope*

## 7.3 Test NAS: Depth Sensor Test (21st June 2021)

### 7.3.1 'Squeeze Test' (21st June 2021)

- Deliverable equipment used: ACPS, VIM & Acoustic Module
- Non-Deliverable equipment used: Test cable (ACPS Rack to VIM connection)

The four pressure sensors in the acoustic module (Keller PA-20D) are no longer accessible after hosing. A full calibration has been presented previously, prior to the hosing operation [3]. To demonstrate that the depth sensors are functioning with the acoustic module on the bench, the hose was squeezed rhythmically by hand, at each of the sensor positions. The result (using the deliverable *CANAM.sh* software) is shown in figure 35. It is worth noting that the mean depth indicated by the 4 sensors is around 15.6m. This is due to the oil-pressure in the hose of around 1.5bar. The standard procedure during a normal at-sea deployment, is to stream the array on the surface, measure these offsets and subsequently subtract them to obtain the true array depth.

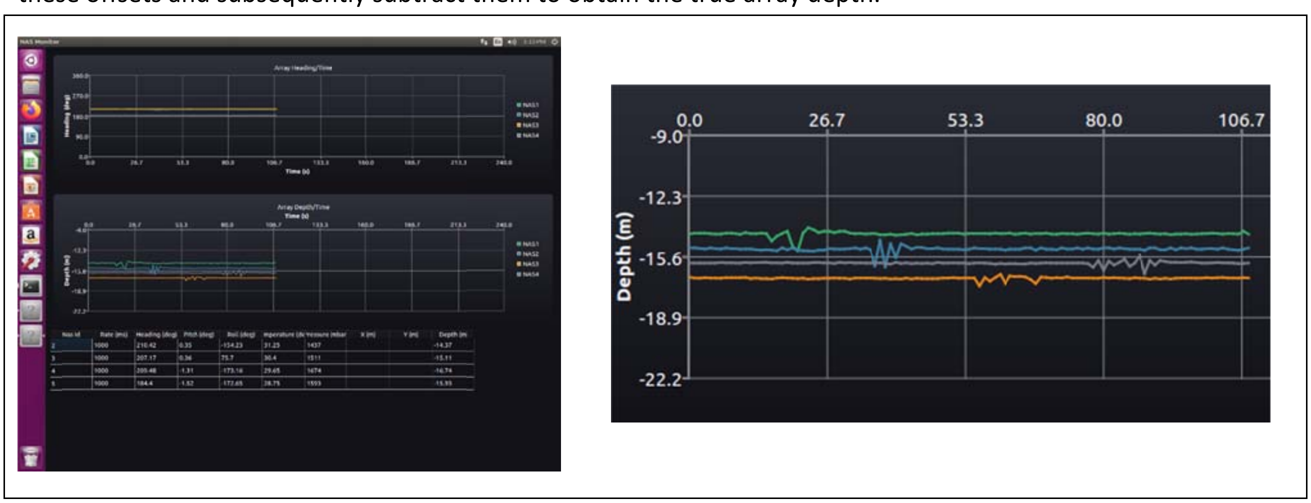


*Figure 35. Depth sensor 'Squeeze Test'. Hose is squezed in the vicinity of the sensor. The sequence of the squeezing is: Nas1 (green), NAS2 (blue), NAS3 (orange), NAS4 (grey). The mean depth offset is due to oil pressure inside the hose.*

### 7.3.2 Pressure Gauge Calibration (19th February 2021)

- Deliverable equipment used: ACPS, VIM & Acoustic Module (prior to hosing)

Non-Deliverable equipment used: Test cable (ACPS Rack to VIM connection), Fluke 700HTPK Hydraulic Test Pressure Kit.

Since the 'squeeze test' described in section 7.3.1 is purely functional, calibrations taken prior to hosing of the acoustic module and previously reported in [3] are reproduced in figure 36, for completeness.

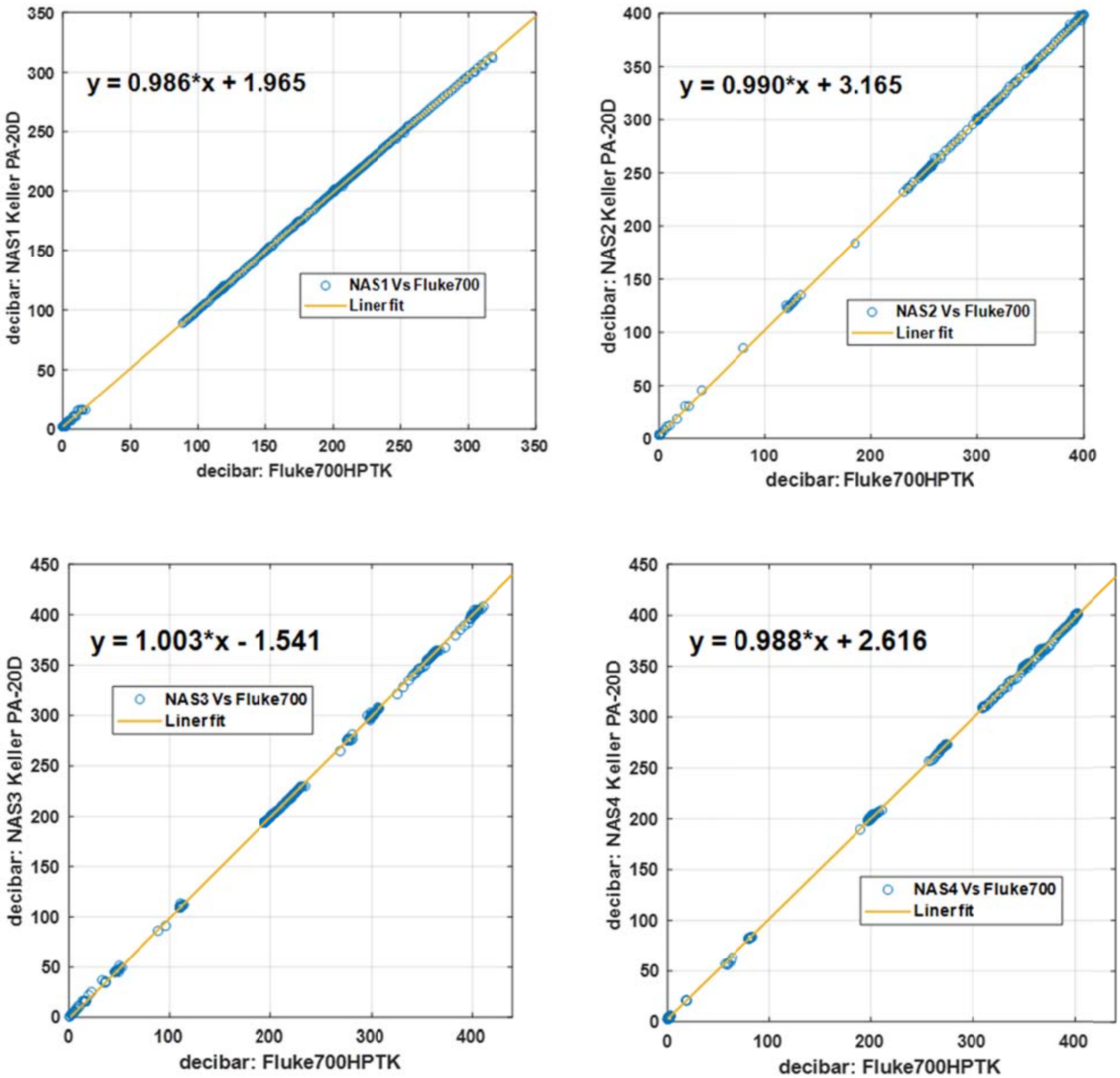


*Figure 36. Applied pressure vs. Measured pressure for the 4 pressure sensors in the array. The slopes are close to unity with offsets varying between -1.5 decibar to 3.5 decibar.*

# 8 Hydrophone Spacing Measurements (15 June 2021)

- Deliverable equipment used: Acoustic Module
- Non-Deliverable equipment used: LASER rangefinder, dynamometer and hand operated winch (applying 400N of tension).

The method was previously described in [3]. The resulting distance measurements (relative to hydrophone 1) are shown in figure 37. The 3 slopes visible in this plot are the 3 octave spacings of the array (18.75cm, 37.5cm and 75cm). This is seen more clearly in figure 38, which plots spacings between hydrophone pairs. Finally, figure 39 shows the spacings for each octave together with standard deviations.

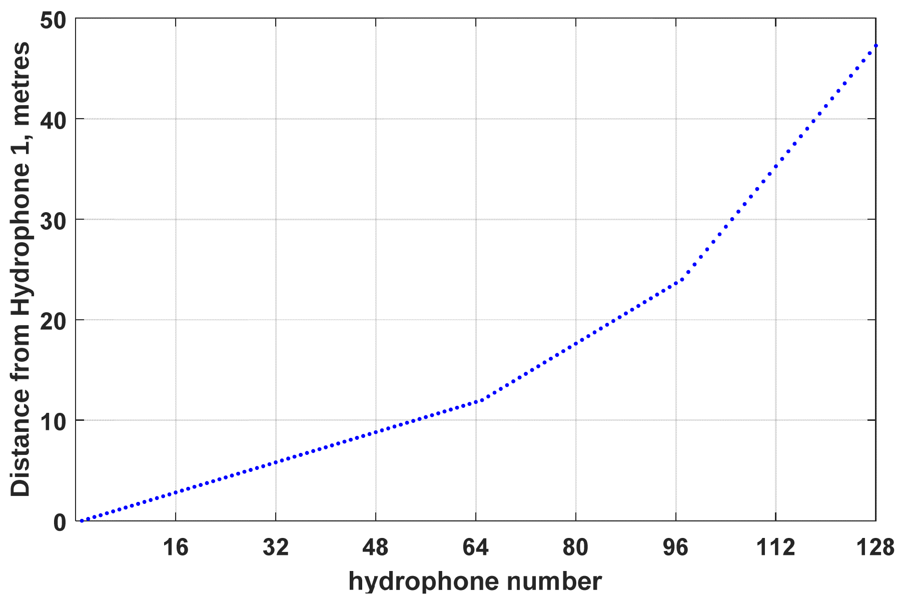


*Figure 37. Distance measurements af all hydrophones with respect to hydrophone 1. The 3 slopes represent the 3 different spacings within the array*

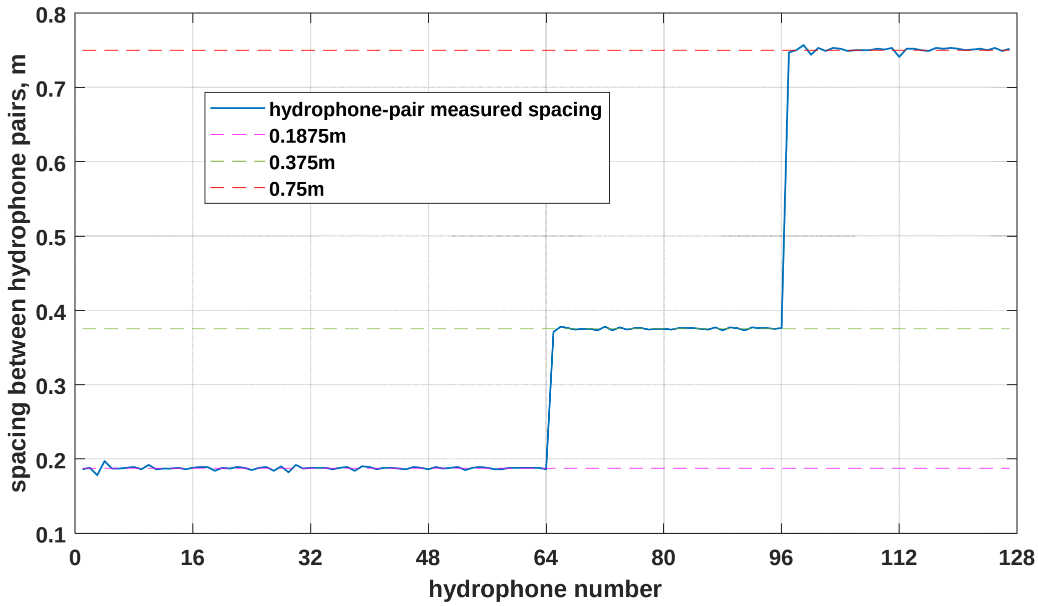


*Figure 38. Range data plotted as hydrophone pair spacing. The 3 spacings (0.1875m, 0.375m, 0.75m) are evident.*

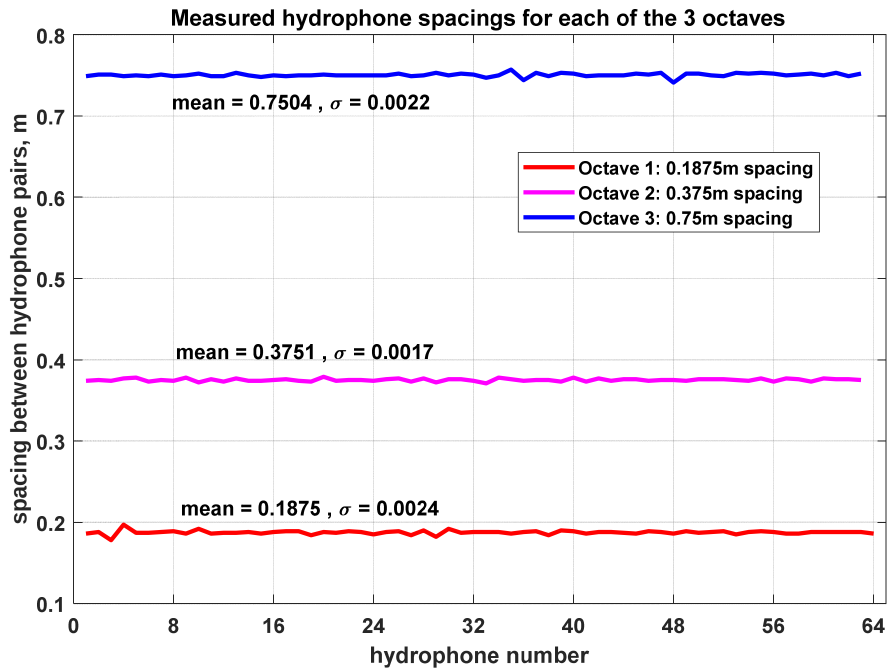


*Figure 39. Range data plotted as octave spacings, including mean and standard deviation*

# 9 Annex

## 9.1 Payment Schedule

**From:** Troiano Luigi | CMRE
**Sent:** 23 April 2020 19:05
**To:** 'Chad M. Smith' <cms561@arl.psu.edu>
**Cc:** Biagini Stefano | CMRE <Stefano.Biagini@nr.nato>; Maguer Alain | CMRE <Alain.Maguer@nr.nato>
**Subject:** FORA replacement build

Hello Chad,

Following our teleconference today, I would like to propose the following revised payment schedule:

| Payment number | ITEM DESCRIPTION | Amount | Milestone list ref (table 2 of Proposal document) | Estimated date |
|---|---|---|---|---|
| 1 | Acoustic Module Design | 10% | 30 | Paid |
| 2 | Reception of long-lead item components | 30% | 5,7,14,52,59,60 | Invoice issued |
| 3 | ACPS (including software) | 10% | 57 | Oct 2020 |
| 4 | Completion of Tow-Cable/deck cable/ VIM/Acoustic Module | 20% | 18,68,49 | Dec 2020 |
| 5 | Factory Acceptance Test (Bench test in-air) | 10% | 79 & Section 4 | Jan 2021 |
| 6 | Delivery | 20% | 79 | 24 Feb 2021 |

Please let me know if you require further details,
Best regards,
Luigi

## 9.2 Penn State PM comments/questions arising from the draft FAT report (Chad Smith email, 5th August 2021)

### 9.2.1 *Request to add the pressure gauge calibrations reported in [3] to the present document.*

New section added (7.4) with the requested data

### 9.2.2 *Question 1: Several optical pairs are not connected to the switch. Are these simply spares? Does all the array data pass over the single pair?*

Answer: Yes, only a single pair is required. The other terminations are provided as spares. Should an optical fiber in the tow cable break, an alternative pair may be utilised, buy opening the E/O converter, substituting another fiber pair for the damaged one, and repeating the procedure at the winch junction box and ACPS rack

### 9.2.3 *Question 2: The Sonifex timing unit used. Looking up the specs I believe it has a BNC PPS output that can be select to 1, 10, 100, or 1000 Hz. Am I looking at the correct model/options?*

Answer: Yes, the Variable PPS output can be set, via the instrument's web interface to frequencies of 1,10,100, 1000 Hz.

### 9.2.4 *Question 3: The acoustic module length was measured at 400N tension. Is this roughly the maximum expected force at 10 kts with drogue?*

Answer: No, it is the expected tension at approximately 5kn (see figure 40). This is considered a more likely operational towing speed than 10kn (note that the tow point tension is the **SUM** of the two curves in figure 40)

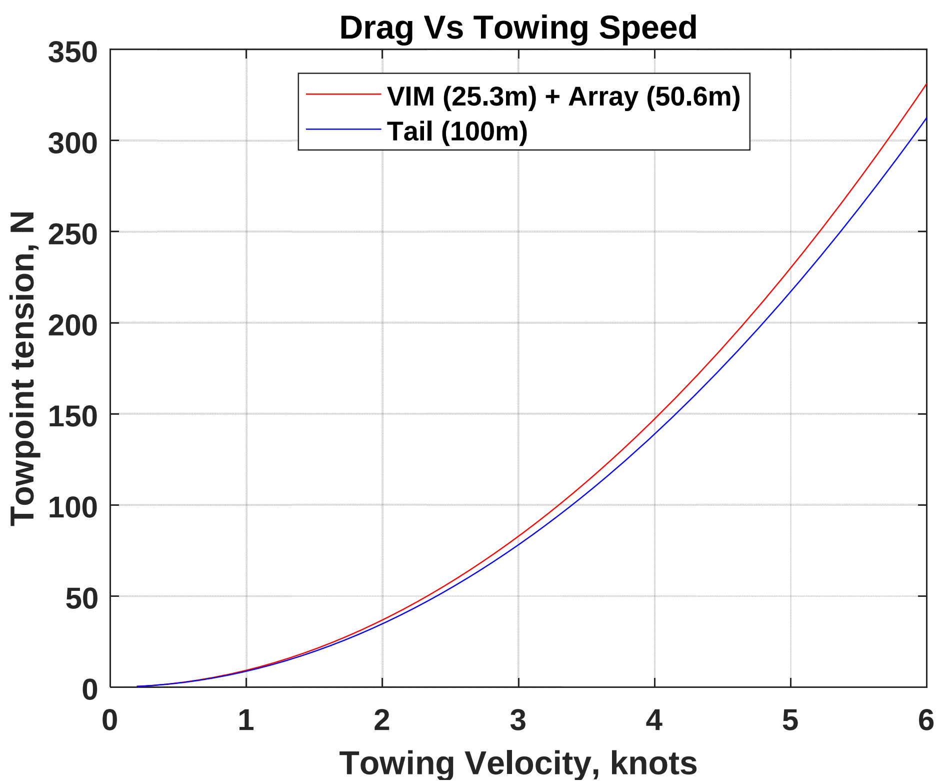


*Figure 40. Tension at the towpoint Vs speed for neutrally buoyant VIM + Array & Tail. The two curves must be summed to obtain the overall tension at the towpoint*

#### 9.2.5 *Question 4: What are the storage drive sizes on the DELL acquisition computer?*

Answer: The Dell Precision 3930 PC contains two SATA Class 20, 512 GB SSDs. There are 2 empty slots for additional 2.5" drives.

9.2.3 *Question 5: Fig. 27 for the in-air full array test. There is a "hot" channel across the time domain between channels 60 and 80. Is this 66? I would have expected the opposite of course with decreased sensitivity, but there is no color scale on these plots for me to get a feeling of scale. Maybe this is external noise, but I don't see it in the noise run.*

Answer: channel 67 does indeed have a higher rms noise level than adjacent channels. The source of the noise is 50Hz power-line pick-up, extrinsic to the array since it later disappears (as you point out, it is not present in the background noise plot, figure 29). The effect is best illustrated by plotting the power spectrum of channel 67 compared to a quieter channel (see figure 41). It should be noted that sensitivity and noise floor of channel 67 (sections 6.1 and 6.2) are normal, and consequently the higher 'noise' level referred to is not a concern.

However, in investigating this phenomenon, an issue was found with channel 67 that had not previously been noted; that of NAS channel crosstalk (see figure 42). The burst of noise seen on the plot is a packet of NAS data, coupling onto the hydrophone channel. This effect has not been noted on other channels. If required, the effect of this interference could be mitigated by reducing the interrogation rate of the NAS sensors from the default 1 Hz.

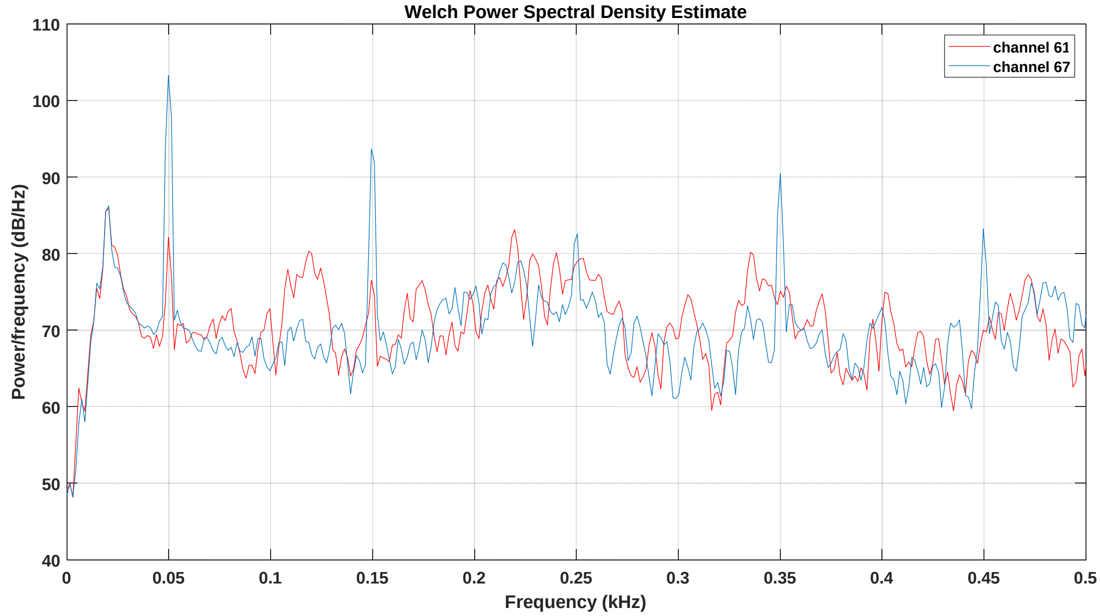


*Figure 41. power spectrum of channel 67, affected by mains pick-up, compared to a quieter channel (61). Fundamental and odd harmonics of 50Hz are much more prominent in channel 67. Data file:* ‘`fora_2021173154720.dat`’

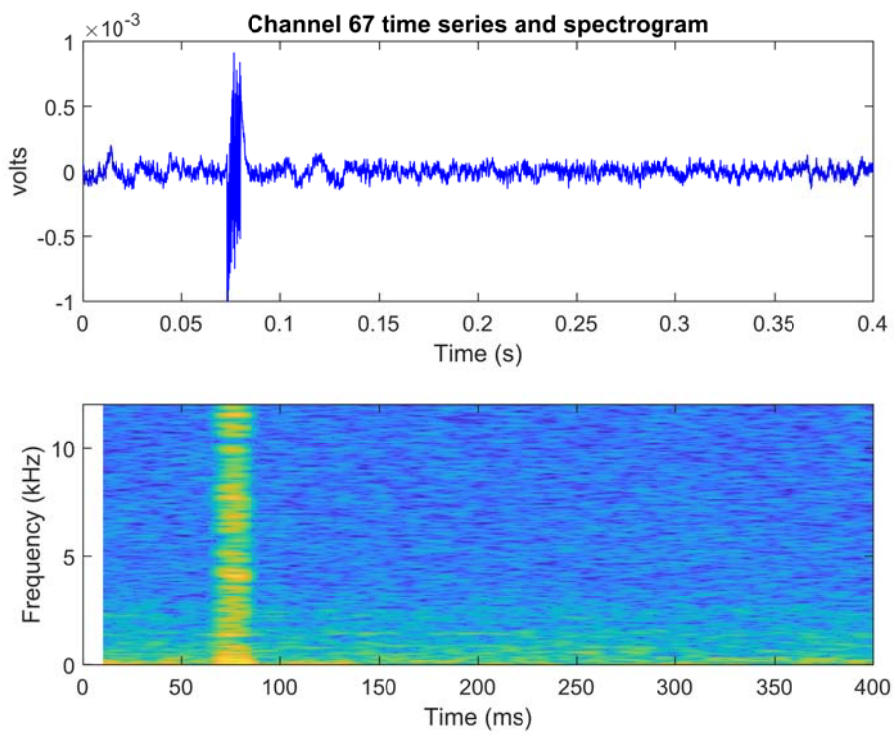


*Figure 42. Coupling of NAS data onto acoustc channel 67. Data file:* ‘`fora_2021173161200.dat`’

# 10 References


1. Troiano L., Dymond R., Bernardini M., Pinzani D., **“Acoustic Module Design”** 31 Oct. 2019. (Penn State University/ARL Contract/PO 940779 FORA Replacement Array).
2. Troiano L., Aglietti F., Bernardini M., Pinzani D., Dymond R., 21 Oct. 2020**. “Array Controller/ Power Supply/Storage (ACPS) Factory Test Specification”** (Penn State University/ARL Contract/PO 940779 FORA Replacement Array)
3. Troiano L., Dymond R., Markovic M., Bernardini M., Sapienza A., Pinzani D., Azzarini R., Sambucetti G., Grenon G., 21st May 2021, **“Pre-FAT Status Report”**, (Penn State University/ARL Contract/PO 940779 FORA Replacement Array)
4. Troiano L., Bernardini M., Mazzi M., 21st Feb 2021, **“Follow-up to ACPS-FAT: µDASS Frequency Response and Delay”**, (Penn State University/ARL Contract/PO 940779 FORA Replacement Array)